BUREAU OF RECLAMATION

Technical Memorandum No. 86-68330-2024-8

Analyses of the Fall 2020 Seismicity Swarm

Paradox Valley Unit, Colorado

Colorado River Basin Salinity Control Program
Upper Colorado Basin Region

U.S. Department of the Interior **August 2024**

Mission Statements

The U.S. Department of the Interior protects and manages the Nation's natural resources and cultural heritage; provides scientific and other information about those resources; honors its trust responsibilities or special commitments to American Indians, Alaska Natives, and affiliated Island Communities.

The mission of the Bureau of Reclamation is to manage, develop, and protect water and related resources in an environmentally and economically sound manner in the interest of the American public.

Technical Memorandum No. 86-68330-2024-8

Analyses of the Fall 2020 Seismicity Swarm
Paradox Valley Unit, Colorado

Colorado River Basin Salinity Control Program
Upper Colorado Basin Region

Prepared by:

Bureau of Reclamation
Technical Service Center
Denver, Colorado

U.S. Department of the Interior **August 2024**

Technical Memorandum No. 86-68330-2024-8

Analyses of the Fall 2020 Seismicity Swarm

Paradox Valley Unit, Colorado

Colorado River Basin Salinity Control Program
Upper Colorado Basin Region

LISA BLOCK

Digitally signed by LISA BLOCK
Date: 2024.08.27 12:45:39 -06'00'

Prepared by: Lisa Block
Geophysicist, Geomorphology and Seismology Group, 86-68330

Peer Review Certification

This report has been reviewed and is believed to be in accordance with the service agreement and standards of the profession.

JUSTIN BALL

Digitally signed by JUSTIN BALL
Date: 2024.08.26 17:24:24 -06'00'

Peer reviewed by: Justin Ball
Geophysicist, Geomorphology and Seismology Group, 86-68330

Acronyms and Abbreviations

1-D	one-dimensional
3-D	three-dimensional
BOR	Bureau of Reclamation
FoS	factor-of-safety
ft	feet
GPa	gigapascals
GR	Gutenberg-Richter
kg/m^3	kilograms per cubic meter
km	kilometers
m	meters
M_D	duration magnitude
mi	miles
m/s	meters per second
M_W	moment magnitude
NW	northwest
Pa	pascals
psi	pounds per square inch
PVSN	Paradox Valley Seismic Network
PVU	Paradox Valley Unit
SE	southeast
SLU	Saint Louis University
SW	southwest
U.S.	United States
USGS	United States Geological Survey
UUSS	University of Utah Seismograph Stations

Symbols

>	greater than
≥	greater than or equal to
<	less than
≤	less than or equal to
±	plus or minus

Contents

Tables

Figures

Figure `Page

Appendices

Appendix

1.0 Introduction

The Paradox Valley Seismic Network (PVSN) monitors earthquakes induced by deep-well brine disposal at the Bureau of Reclamation's Paradox Valley Unit (PVU), as well as local naturally occurring earthquakes. In the fall of 2020, PVSN recorded an unusual swarm of seismicity approximately 3 km southwest of PVU's single injection well and ~1.6 km from the epicenter of an induced earthquake with moment magnitude (M_W) 4.5 that occurred in March 2019 (Figure 1-1). The fall 2020 seismicity swarm occurred in an area interpreted to be outside the reservoir pressurized by PVU injection, where few earthquakes had previously occurred. A major northwest-southeast (NW-SE) trending fault 2.2 km southwest of the PVU injection well has previously been interpreted as forming a barrier to fluid flow and pore pressure diffusion from PVU injection, based on seismic reflection and induced seismicity studies (Bremkamp and Harr, 1988; King et al., 2018). The fall 2020 seismicity swarm lies on the southwest side of this fault (Figure 1-1). We refer to the seismicity cluster where the fall 2020 seismicity swarm occurred as the "SW cluster" throughout this report. The fall 2020 swarm included an unusually large fraction of felt earthquakes, including three earthquakes with magnitude ≥ M_W 3.5. No felt earthquakes had occurred in this area during the preceding 35 years of continual seismic monitoring.

The seismicity swarm occurred from early November 2020 to early January 2021, although earthquakes occurred in the same area at much lower rates both before and after this time period. The swarm occurred approximately 20 months after the PVU injection well had been shut down following the March 2019 M_W 4.5 earthquake. The PVU injection well remained shut shown from March 2019 through May 2022, except for a five-week injection test conducted in April-May 2020.

Several types of analyses were performed to better understand the characteristics of this seismicity swarm and its relation to PVU injection. Seismic analyses to characterize the swarm included: computation of precise relative event locations, generation of time-lapse maps and cross sections, focal mechanism analyses, and Gutenberg-Richter b-value analyses. In addition, Omori aftershock rate analyses were performed to evaluate the possibility that the fall 2020 swarm represents aftershock activity from the March 2019 M_W 4.5 induced earthquake. Modeling of the Coulomb stress transfer associated with fault plane ruptures were also performed for the March 2019 main shock and its largest aftershocks. To further investigate the potential relation of the seismicity swarm to PVU injection, geomechanical modeling was performed. This modeling computes stress and pressure changes over time related to reservoir pressurization and depressurization. This modeling was performed specifically to investigate whether stress changes associated with the prolonged shut-in of the injection well starting in March 2019 or the 5-week injection test in the spring of 2020 could have contributed to the occurrence of the fall 2020 seismicity swarm.

Initial analyses of the SW cluster were performed in 2021. At later dates (2022 to 2024), some of original analyses were updated and additional analyses were performed. Time constraints did not

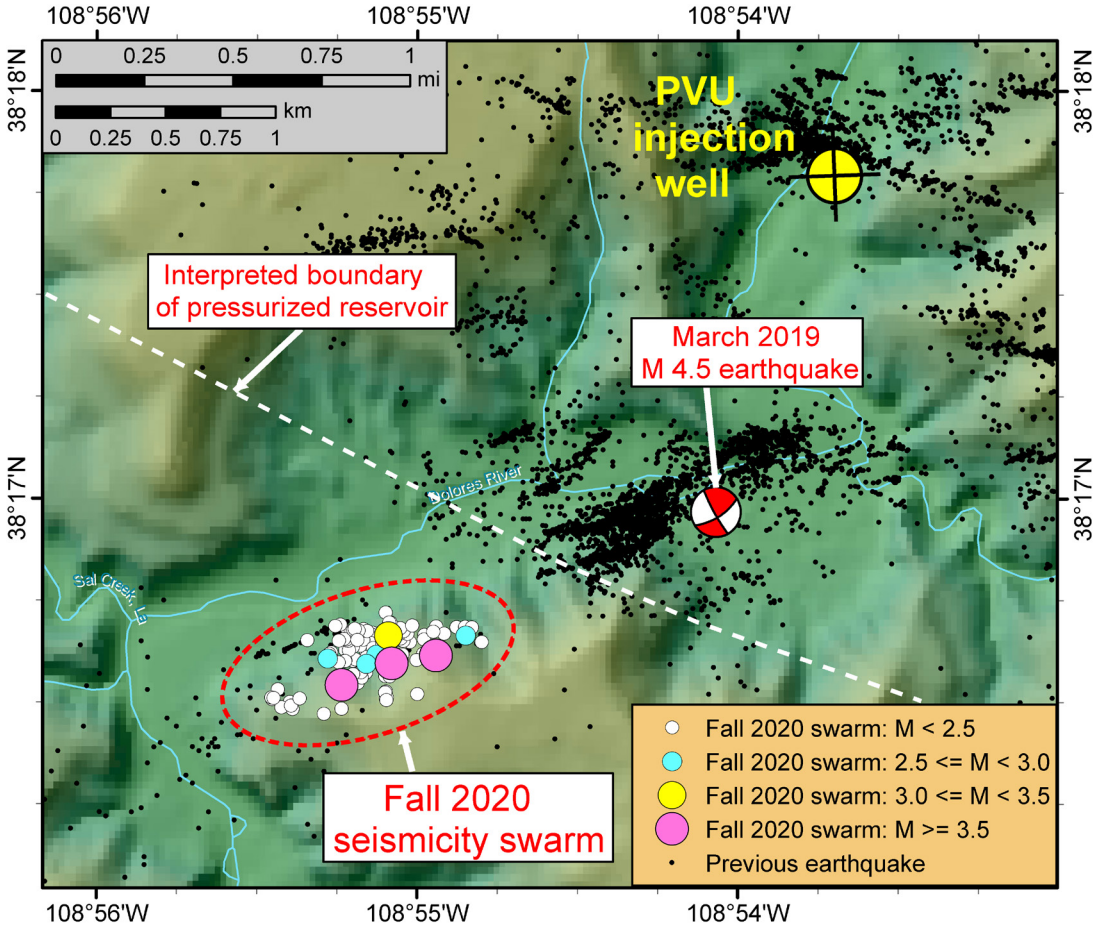

Figure 1-1: Location of the fall 2020 seismicity swarm (dashed red ellipse) relative to the PVU injection well, interpreted (approximate) boundary of the pressurized reservoir, and the March 2019 M_W 4.5 earthquake epicenter (focal mechanism shown). Epicenters of earthquakes that occurred during the swarm from November 2020 to January 2021 are displayed; symbols are sized and colored according to earthquake magnitude as indicated by the legend. The magnitudes shown are duration magnitudes (M_D) for earthquakes with M_D < 3.0 and moment magnitudes for larger events. The black dots are epicenters of earthquakes that occurred prior to November 2020.

allow for updating of all of the original analyses. Hence, the date ranges of earthquakes included in different analyses presented in this report are not always consistent. This discrepancy does not affect any of the interpretations discussed in this report.

1.1 Project Background

Reclamation's PVU, a component of the Colorado River Basin Salinity Control Program, intercepts salt brine that would otherwise flow into the Dolores River, a tributary of the Colorado River. PVU is in western Montrose County, Colorado, approximately 90 km southwest of Grand Junction and 16 km east of the Colorado-Utah border (Figure 1-2). The Dolores River flows

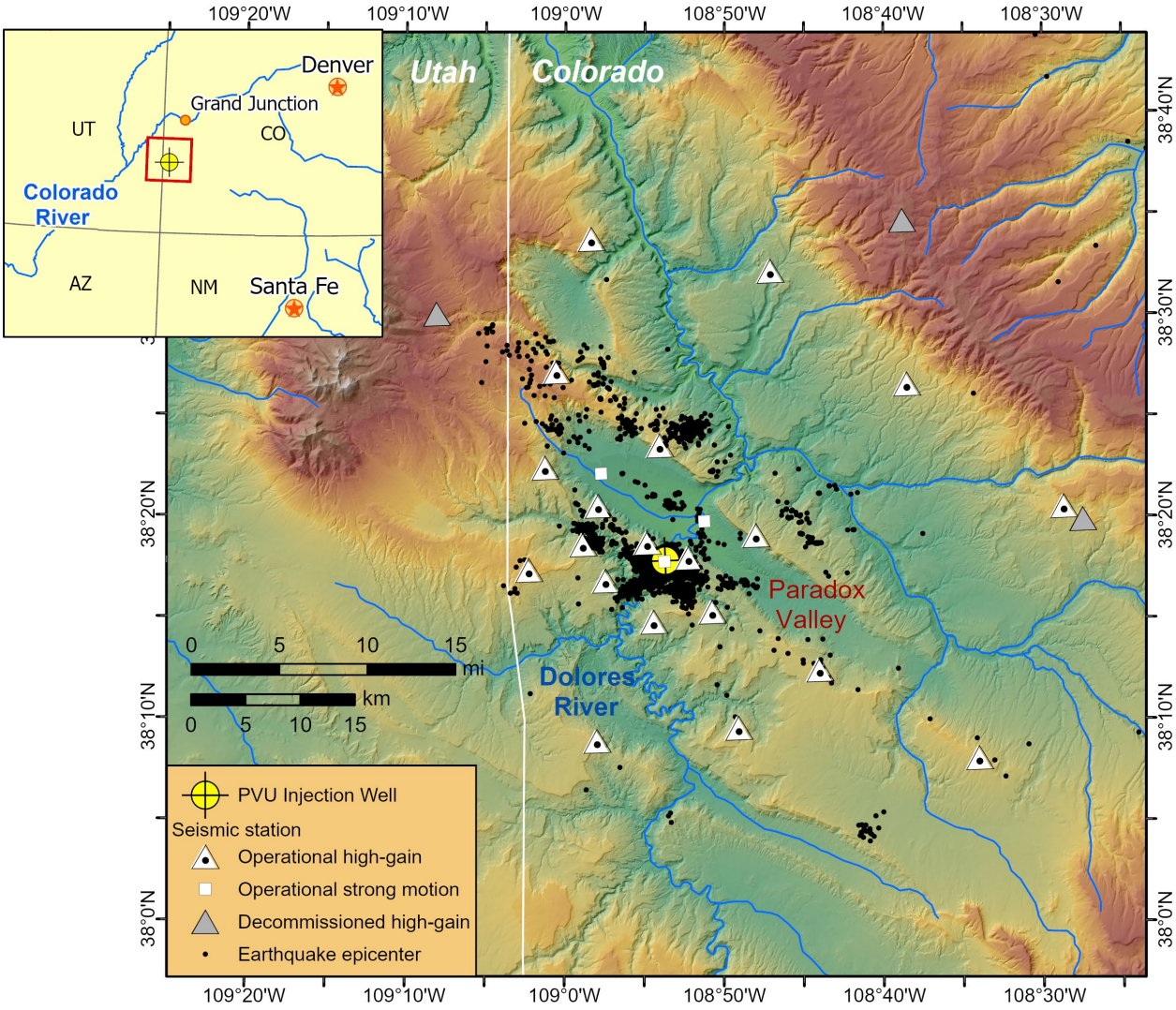

Figure 1-2: Locations of the PVU injection well, PVSN seismic stations, and epicenters of earthquakes ≤ 10 km deep recorded through 2023.

from southwest to northeast across Paradox Valley, which was formed by the collapse of a salt-cored anticline. Due to the presence of the salt diapir underlying Paradox Valley, groundwater within the valley is nearly eight times more saline than ocean water. To prevent this highly saline groundwater from entering the Dolores River and degrading water quality downstream, the brine is extracted from nine shallow wells within the valley near the Dolores River. The diverted brine is injected at high pressure into a single deep disposal well, approximately 1.5 km southwest of Paradox Valley (Figure 1-2). This project is authorized by the Colorado River Basin Salinity Control Act, which was passed by the U.S. Congress in 1974. Further information on PVU can be found at the Reclamation project website (https://www.usbr.gov/uc/progact/paradox).

During the planning for PVU, it was recognized that earthquakes could be induced by the deep-well injection of brine. This was based on comparisons to other deep-well injection projects in Colorado, including the Rocky Mountain Arsenal near Denver and oil and gas extraction projects near Rangely (Gibbs et al., 1973; Hsieh and Bredehoeft, 1981; Nicholson and Wesson, 1990; Raleigh et al., 1976). In 1983, eight years before the first injection at PVU, Reclamation commissioned installation of the Paradox Valley Seismic Network to characterize the pre-injection naturally occurring seismicity in the Paradox Valley region and to monitor earthquakes that might be induced once injection operations began. The seismic network has been operated continually since 1985 and has been expanded and updated over the years to respond to changing seismicity patterns and advances in seismic instrumentation (Block et al., 2024). The current network configuration consists of a surface array of 20 broadband high-gain three-component sensors and three strong motion instruments (Figure 1-2).

No earthquakes were recorded within 18 km of the injection well during six years of pre-injection monitoring (Block et al., 2014). The data recorded during this period include just one local earthquake that occurred almost 19 km from the PVU injection well, at an estimated depth of ~14 km (relative to the PVU wellhead). Within a few days of the start of the initial injection test in 1991, seismic events were detected in the immediate vicinity of the injection well. During subsequent injection tests and the near-continuous injection operations that began in 1996, induced earthquakes occurred at increasing distances from the injection well (Figure 1-3). Most of the earthquakes that have been recorded in the Paradox Valley area since the start of PVU injection have depths between 2 and 7 km (relative to the PVU wellhead), consistent with the depths of target injection formations. Focal depths of the few naturally occurring tectonic events recorded in the area have exceeded 10 km (Block et al., 2014). The close correlation between injection operations and induced seismicity at PVU has been well established, as illustrated by Figure 1-3.

PVU injection operations have been adjusted several times in response to unacceptable levels of induced seismicity (Block et al., 2024). As a result, daily average injection rates have generally decreased over time, and unplanned shut-ins of the injection well have occurred a few times following the largest induced earthquakes (Figure 1-3). The largest PVU-induced event to date is the March 2019 M_W 4.5 earthquake, which occurred 1.6 km southwest of the injection well (Figure 1-1). At the time of this earthquake, the PVU injection well had been shut down for a few hours to accommodate previously scheduled maintenance activities. Following the M_W 4.5 earthquake, the injection well remained shut down for more than a year, while analyses of the seismic and injection data were conducted and aftershock activity was monitored. The well came online temporarily at a reduced flow rate for injection testing from April 21 to May 29, 2020 (Figure 1-3). The flow rate during the test was 115 gpm, a 32% reduction compared to the flow rate prior to the earthquake. Following this short injection test, the PVU injection well was shut down and no additional injection was performed until June 2nd 2022. On that date, PVU injection was resumed at a rate of 115 gpm (Figure 1-3).

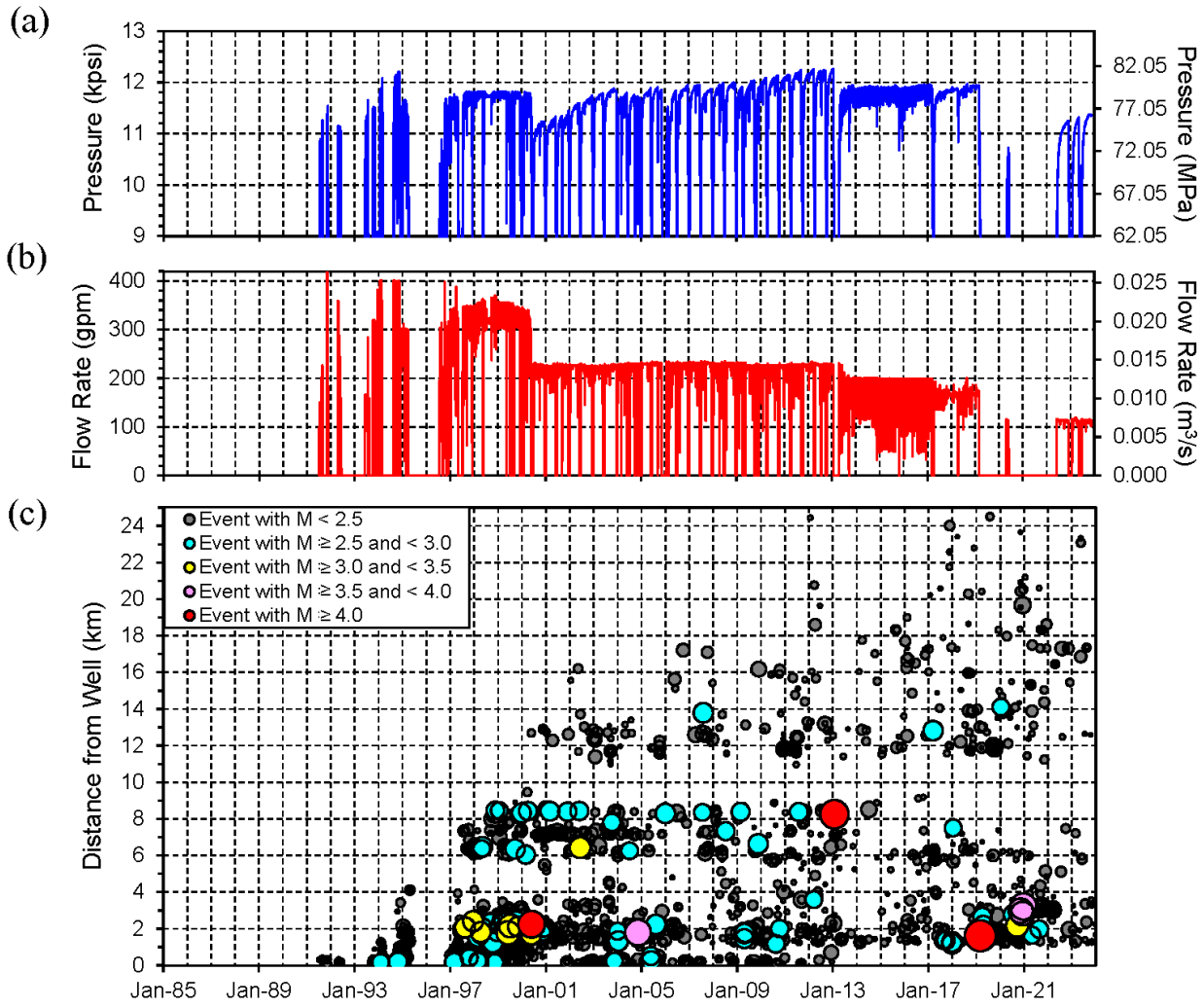

Figure 1-3: (a) Daily average downhole pressure history, (b) daily average injection flow rate history, and (c) moveout of seismicity from the injection well over time. The downhole pressures were computed from the measured surface pressures using the density of the brine column in the well, for a depth of 4.3 km (the top of the perforated zone). In the lower plot, each circle represents a single earthquake with duration magnitude (M_D) ≥ 0.5 and depth ≤ 10 km (relative to the ground surface elevation at the injection wellhead). The width of each circle is scaled by the event magnitude. The magnitudes shown are duration magnitudes for earthquakes with M_D < 3.0 and moment magnitudes for larger events.

2.0 Description of the Seismicity Swarm

2.1 Earthquake Rates and Magnitudes

The fall 2020 seismicity swarm occurred approximately 3 km southwest of the PVU injection well (Figure 1-1), at depths ranging from ~3.75 to ~4.75 km relative to the PVU wellhead. No earthquakes were detected at the location of this swarm prior to March 2019. Several earthquakes were detected here from early March to early May 2019, including an earthquake with magnitude M_D 2.7 (Figure 2-1). Only two additional earthquakes were recorded in this cluster during the following 13 months, from June 2019 through June 2020. The larger of these earthquakes had a magnitude of M_D 2.2. Six additional earthquakes occurred in July and early August 2020, including an earthquake with magnitude M_D 2.7. The seismicity rate substantially increased on November 8th 2020 when an earthquake with M_W 3.6 occurred, followed by several smaller-magnitude aftershocks (Figure 2-1). Several other significant earthquakes occurred in

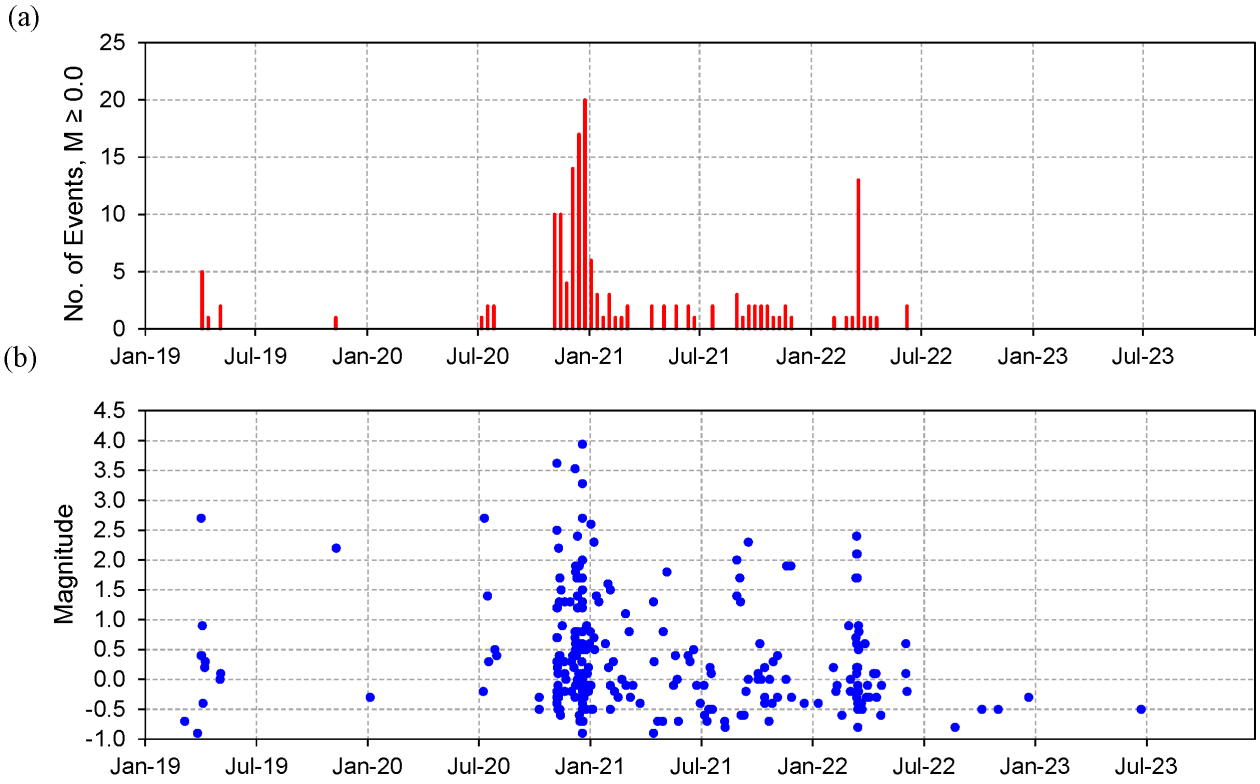

Figure 2-1: Seismicity recorded in the area of the fall 2020 swarm during 2019 to 2023: (a) rates of events with magnitude ≥ M_D 0.0, and (b) scatter plot of events by date and magnitude. The rates shown in part (a) are for 10-day (non-overlapping) bins. The magnitudes shown in part (b) are duration magnitudes for earthquakes with M_D < 3.0 and moment magnitudes for larger events.

the following weeks, including: an M_w 3.5 earthquake on December 8th, M_w 3.3 and M_w 3.9 earthquakes on December 20th, and four other events with magnitudes between M_D 2.5 and M_D 3.0 between early November 2020 and early January 2021 (Figure 2-1; two M_D 2.5 events on November 8th overlay in Figure 2-1b). This seismicity swarm ended in early January 2021, but earthquakes continued to occur in this area at lower rates and magnitudes until March 2022, when a less intense swarm occurred (Figure 2-1). The largest earthquake during the March 2022 swarm had a magnitude of M_D 2.4. Seismicity rates in the SW cluster decreased abruptly in early June 2022. From July 2022 through December 2023, only five earthquakes were detected in the SW cluster, and these events all have magnitudes < M_D 0.0 (Figure 2-1b).

The occurrence of three earthquakes with $M_w \geq 3.5$ within two months, which occurred during the fall 2020 seismicity swarm, is extremely unusual. Only four other earthquakes of this magnitude have been recorded in the Paradox Valley area since PVSN seismic monitoring began in 1985. All four of those earthquakes are interpreted as induced by PVU injection. In addition, the December 20th M_w 3.9 earthquake is the fourth-largest local earthquake recorded by PVSN. The local earthquakes with $M_w \geq 3.5$ recorded during the fall 2020 seismicity swarm and in previous years are listed in Table 2-1. Six of these seven earthquakes occurred within 3.5 km of the PVU injection well, including the three events that occurred in November-December 2020.

Table 2-1: Local earthquakes with *Mw* ≥ 3.5 recorded by PVSN from 1985 through 2023.

Date	Moment Magnitude BOR[1]	Moment Magnitude USGS/UUSS[2]	Moment Magnitude SLU[3]	Distance from PVU Injection Well (km)
5/27/2000	4.01	3.8	3.77	2.3
11/7/2004	3.86	---	3.60	1.8
1/24/2013	4.26	3.9 - 4.0	3.95	8.3
3/4/2019	4.65	4.4 - 4.6	4.45	1.6
11/8/2020	3.62	---	---	3.0
12/8/2020	3.53	---	---	2.8
12/20/2020	3.94	3.7	3.65	3.2

[1] Bureau of Reclamation. *Mw* values were retrieved from the BOR PVSN database on 6/22/22. *Mw* values are computed using only PVSN data.

[2] United States Geological Survey (USGS) and the University of Utah Seismograph Stations (UUSS). *Mw* values were retrieved from https://earthquake.usgs.gov/earthquakes/search/ on 6/22/22. *Mw* values are computed using data from regional seismic stations.

[3] St. Louis University. *Mw* values were retrieved from https://www.eas.slu.edu/eqc/eqc_mt/MECH.NA/ on 6/22/22. *Mw* values are computed using data from regional seismic stations.

2.2 Magnitude-Frequency Distribution

The SW cluster appears to produce an unusually large percentage of larger-magnitude earthquakes compared to smaller-magnitude earthquakes. The relative occurrence of earthquakes of different magnitudes is commonly characterized by the Gutenberg-Richter (GR) magnitude-frequency relationship (Gutenberg and Richter, 1954):

$$log_{10}(no.\,of\ earthquakes\ with\ mag \geq M) = a - bM$$

The GR fits to the magnitude-frequency data from earthquakes occurring in the SW cluster from March 2019 to July 2021 are shown in Figure 2-2. Separate fits are plotted for duration magnitudes and moment magnitudes, over magnitude ranges that are appropriate for each magnitude scale. These fits indicate GR b-values of 0.43 – 0.45. These b-values are unusually low and indicate an unusually high percentage of larger-magnitude earthquakes. More advanced methods for computing the GR b-values are available and have been applied to PVSN induced seismicity previously (Wood et al., 2016). These methods have not yet been applied to the data from the SW cluster but should be considered for future analyses.

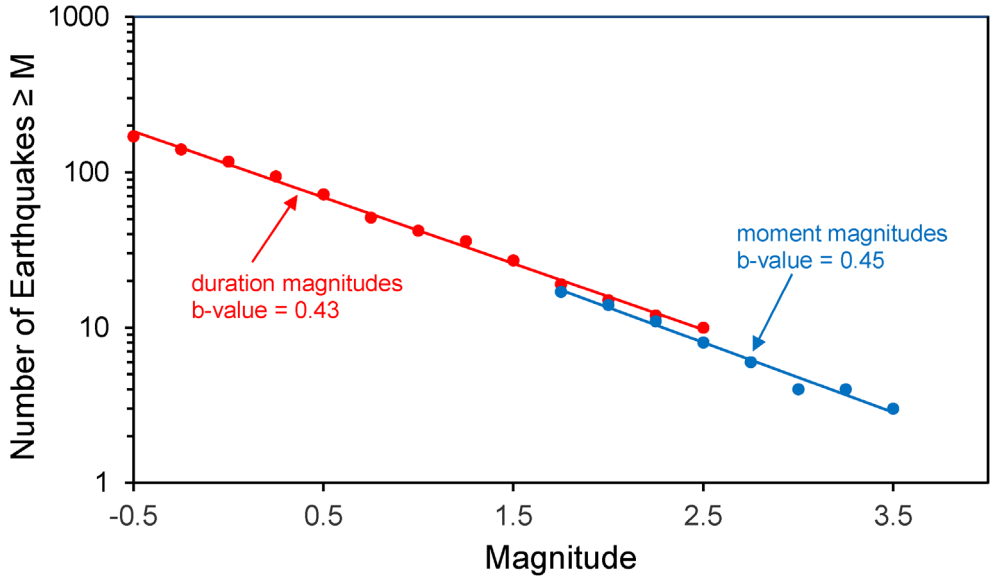

Figure 2-2: Gutenberg-Richter fits for earthquakes occurring in the SW cluster from March 2019 to July 2021. The filled circles are the magnitude-frequency data computed with a magnitude bin of 0.25, and the lines are the GR fits. The GR b-values from the slopes of the linear fits are labeled. The red data are from the duration magnitudes, and the blue data are from the moment magnitudes.

2.3 Hypocenter Distribution and Focal Mechanisms

Following PVSN's standard data processing procedures for local earthquakes, absolute hypocenters for earthquakes in the SW cluster were initially computed using manually determined P-wave and S-wave arrival times. These hypocenters were computed using three-dimensional (3-D) velocity models developed previously from hypocenter-velocity inversions of arrival times from local earthquakes and explosions. Precise relative hypocenters were subsequently computed from P-wave and S-wave arrival time differences obtained from cross-correlations of waveforms from pairs of earthquakes. This relative location procedure is applied simultaneously to all local earthquakes throughout the Paradox Valley area recorded during a given time period, during occasional updates of the PVSN earthquake catalog. During these updates, earthquakes are tied to other nearby events occurring during the same time period and to all previously recorded nearby events. During the relative event location, the absolute hypocenter of one earthquake in the SW cluster was fixed as a constraint. (Similarly, a few widely spaced absolute hypocenters are fixed in other areas, as discussed in Block et al. (2015).) Because the earthquakes in the SW cluster exhibit very similar waveforms at many stations, 261 of the 267 events recorded there during 2019-2023 (~98%) tied into the relative location. These relative hypocenters are assigned a quality of *a*. For the few remaining events, the absolute hypocenters are used and assigned a quality of *b*.

The a-quality hypocenters in the SW cluster recorded through January 2021 form a single east-northeast-trending, steeply dipping planar feature (Figure 2-3). This feature strikes

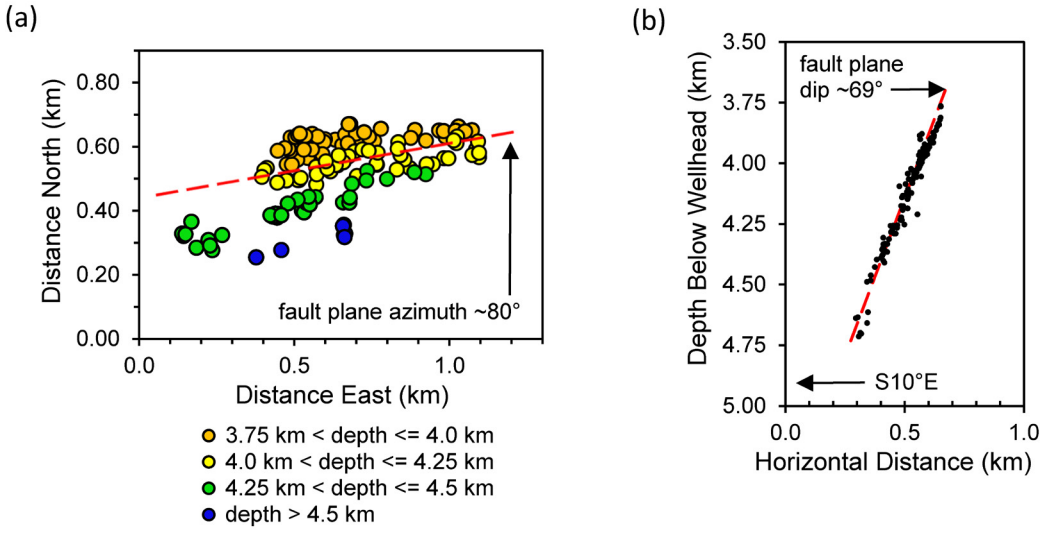

Figure 2-3: A-quality hypocenters of events that occurred in the SW cluster during Mar. 2019 to Jan. 2021: (a) plan view with symbols color-coded by hypocenter depth, and (b) vertical projection perpendicular to the strike of the inferred fault plane (looking N100°W). The dashed red line in each plot indicates the orientation of the inferred fault plane.

approximately N80°E and dips ~69° to the south. Hypocenters recorded through January 2021 occur over a horizontal distance of approximately 1 km along-strike (Figure 2-3a) and about the same distance vertically (Figure 2-3b).

To confirm that the planar feature formed by the relative hypocenters is the fault plane on which these earthquakes occurred, focal mechanisms were computed from larger earthquakes within the cluster. The mechanisms were computed using a grid search method applied to the waveform P-wave first break data, with the software *focmec* (Snoke, 2009). This program systematically searches the focal sphere and outputs all double-couple orientations that meet specified polarity match criteria. The averages of the acceptable fits are subsequently computed as the final solutions presented here. For these calculations, the relative earthquake locations and local 3-D P-wave velocity model were used to compute the azimuths and takeoff angles of the ray paths. The grid search was performed at a 1° increment, and relative weighting of polarity mismatches was used to down-weight mismatches near nodal planes.

One of the nodal planes of the computed focal mechanisms is consistent with the orientation of the planar hypocenter feature. Focal mechanisms for the four earthquakes with magnitude > M_W 3.0 that occurred during the fall 2020 seismicity swarm are presented in Figure 2-4. The strike azimuths of the east-west nodal planes from three of these mechanisms range from 78° to 80°, and the corresponding dips are 73°-74° (to the south). For the remaining earthquake, the focal mechanism solution is less robust and yields a strike of 88° and dip of 65°. A composite focal mechanism was also computed, using first break data from 43 larger earthquakes within the cluster (generally those with duration magnitude ≥ ~1.2 that occurred through 2021). The hypocenters of these 43 earthquakes are presented in Figure 2-5, and the composite focal mechanism is shown in Figure 2-6. The earthquakes are distributed over much of the interpreted fault plane along strike and depth (Figure 2-5). The east-west nodal plane from the composite mechanism has a strike of 80° and a dip of 71° to the south (Figure 2-6), consistent with the orientation of the planar hypocenter feature (80° strike and 69° dip).

In summary, both the precise relative earthquake hypocenters and the focal mechanisms indicate that the earthquakes within the SW cluster are occurring on a fault striking ~N80°E and dipping 69° to 74° to the south. The rakes from three of the individual earthquake focal mechanisms are 176°-177° degrees (Figure 2-4 a, b, and c). The rake from the less robust individual focal mechanism is -157° (Figure 2-4 d), and the rake from the composite focal mechanism is -171°. These results indicate that the fault has primarily right-lateral strike-slip displacement.

The moment magnitude solution for the largest earthquake that occurred during the fall 2020 seismicity swarm (12/20/2020 M_W 3.9 earthquake) indicates a fault radius of 0.53 km (for a simple circular rupture model (Brune, 1970, 1971) with the computed stress drop of 24 bars). This radius is consistent with the dimensions of the active fault surface (through Jan. 2021) indicated by the distribution of a-quality hypocenters (Figure 2-3). Hence, this earthquake likely ruptured the entire identified fault segment.

(a) November 8, 2020 M_W 3.6 earthquake: strike 79°, dip 74° south, rake 176°

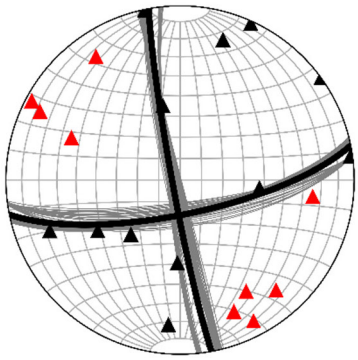

(b) December 8, 2020 M_W 3.5 earthquake: strike 80°, dip 73° south, rake 177°

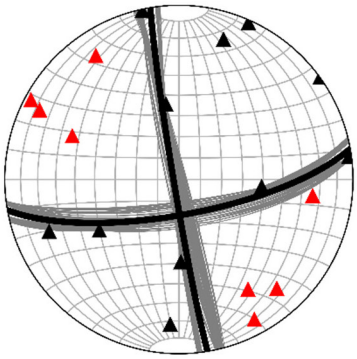

(c) December 20, 2020 M_W 3.3 earthquake: strike 78°, dip 74° south, rake 177°

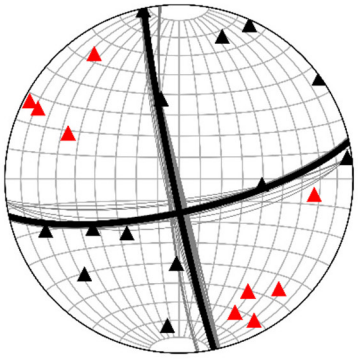

(d) December 20, 2020 M_W 3.9 earthquake: strike 88°, dip 65° south, rake -157°

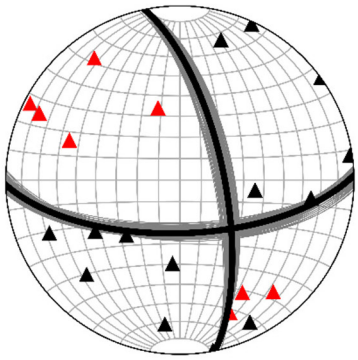

Figure 2-4: Focal mechanisms for the four earthquakes with M_W > 3.0 that occurred during the fall 2020 seismicity swarm. These mechanisms were computed from first break data with the program *focmec,* which uses a grid search method to find all mechanisms that meet a defined set of criteria. An increment of 1° was used for the grid search, and relative weighting was used to down-weight polarity misfits near nodal planes. Parameters were set to allow one polarity mismatch in areas with a theoretical radiation pattern ≤ 0.2 for the three mechanisms in (a), (b), and (c). The threshold was increased to 0.3 for (d) to obtain results. The thin lines represent acceptable focal mechanism fits; the heavy lines represent the means of the acceptable fits. The strike, dip, and rake of the mean fit for the east-west focal plane is given in the heading for each earthquake. The compressional and dilatational first breaks are represented by the black and red triangles, respectively.

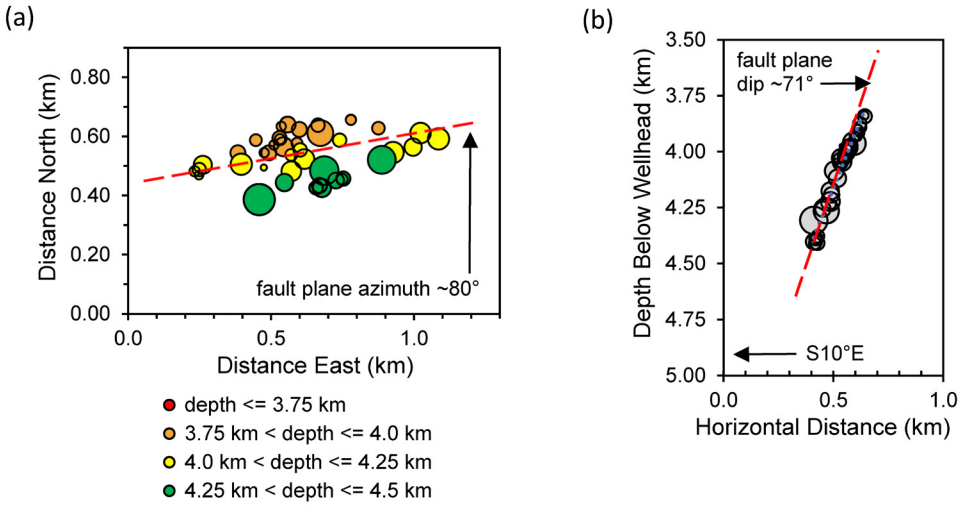

Figure 2-5: Hypocenters of 43 earthquakes in the SW cluster whose first break data were used for the composite focal mechanism shown in Figure 2-6: (a) map view and (b) vertical projection perpendicular to the strike of the inferred fault plane (looking N100°W). The widths of the circles representing the hypocenters are scaled by the earthquake magnitudes. The dashed red line in each plot indicates the orientation of the east-west focal plane from the composite focal mechanism.

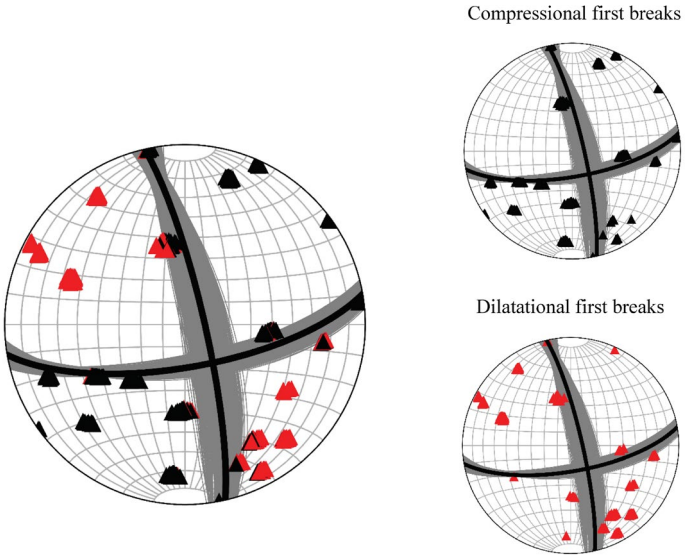

Figure 2-6: Composite focal mechanism determined using first break data from 43 of the larger earthquakes in the SW cluster (generally those with magnitude > ~M_D 1.2, shown in Figure 2-5). The mechanism was computed with the program *focmec*, using an increment of 1° for the grid search. Polarity mismatches were relatively weighted according to the theoretical radiation pattern, with equal weighting below the threshold of 0.1. The maximum allowable sum of weighted polarity mismatches was 16. The thin lines represent acceptable focal mechanism fits; the heavy lines represent the mean of the acceptable fits. The mean fit for the east-west focal plane is: strike 80°, dip 71° south, and rake -171°.

2.4 Growth of Active Fault Area Over Time

The growth over time of the seismically active portion of the fault plane in the SW cluster is illustrated by the series of plots in Figure 2-7 to Figure 2-9. These plots show the a-quality (relative) hypocenters in the SW cluster in plan view (Figure 2-7), projected into the interpreted fault plane (Figure 2-8), and projected perpendicular to the interpreted fault plane (Figure 2-9). For each type of projection (i.e., each figure), multiple plots are included. Each plot shows the cumulative hypocenters through the date in the plot heading, with dates ranging from March 2019 to December 2023. Hypocenters are sized and color-coded according to earthquake magnitude (see figure captions).

The seismically active area of the identified fault in the SW cluster grew very slowly from March 2019 through October 2020. One earthquake with an a-quality hypocenter occurred in late March 2019, on the east end of the SW cluster (Figure 2-7a, Figure 2-8a). A few additional events occurred close to the initial earthquake during April 2019 (Figure 2-7b, Figure 2-8b). These events extend slightly shallower along the interpreted fault plane than the initial earthquake (Figure 2-9b). As a few additional earthquakes occurred during the following 18 months (through October 2020), the small seismicity cluster spread a little more toward the west (Figure 2-7c, Figure 2-8c). During this time period, the cluster also grew slightly in the vertical direction, mostly extending deeper along the fault plane (Figure 2-9c).

During the seismicity swarm in November-December 2020, the seismically active area of the fault plane increased substantially. The earthquake hypocenters spread farther west, with no change to the eastern extent of the seismically active fault plane (Figure 2-7d-f and Figure 2-8d-f). Along strike, the active fault length increased from about 300 m to ~1 km. A similar growth is seen along the dip of the fault plane, with the active portion increasing from a width of about 400 m (Figure 2-8c) to ~1 km (Figure 2-8f). The active portion of the fault plane extended both shallower and deeper, but it grew more downward than upward (Figure 2-9d-f). The three earthquakes with magnitude $\geq M_W$ 3.5 occurred in the lower portion of the fault plane.

After December 2020, the extent of the seismically active portion of the fault plane did not expand noticeably until March 2022. During a swarm of low-magnitude earthquakes that month, the seismicity expanded upward along the interpreted fault plane by an additional ~300 m (Figure 2-8h, Figure 2-9h). No further expansion of the active fault plane has occurred since then (Figure 2-8i, Figure 2-9i).

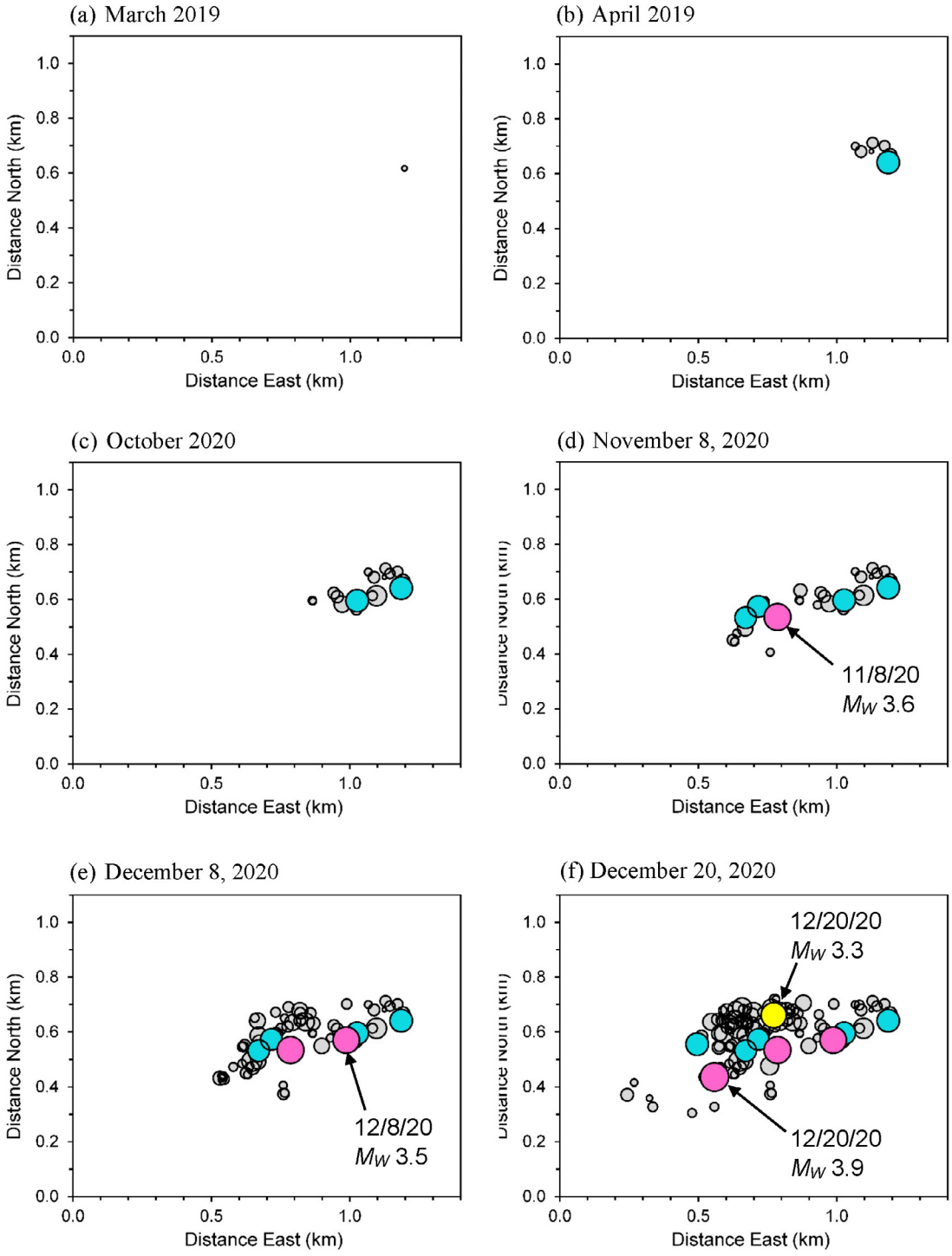

Figure 2-7 – caption on the following page

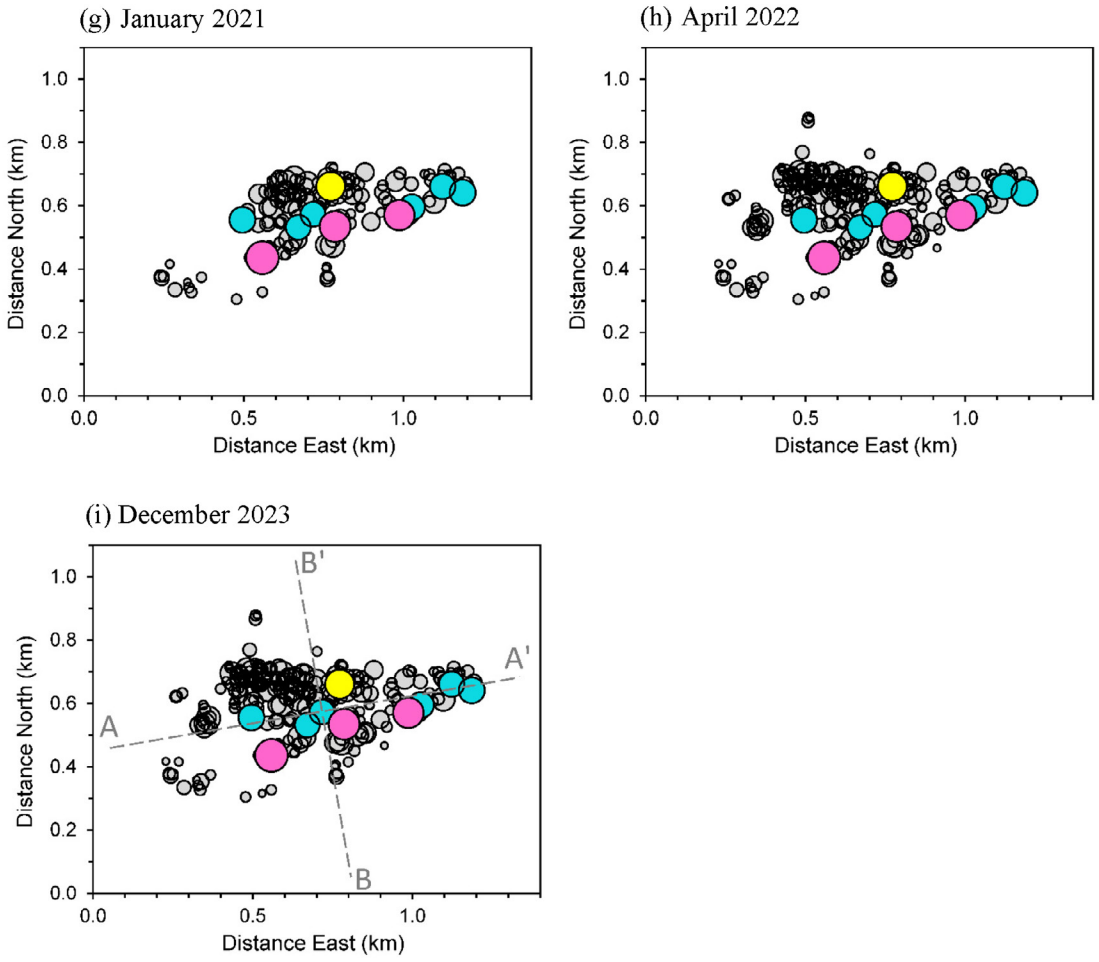

Figure 2-7: Plan views of a-quality earthquake hypocenters over time. Each plot shows the hypocenters of earthquakes recorded from March 2019 through the date listed in the plot heading. Hypocenter symbols are sized by earthquake magnitude, and symbols for larger earthquakes are color-coded: light blue – 2.5 ≤ M < 3.0; yellow – 3.0 ≤ M < 3.5; pink – 3.5 ≤ M < 4.0. The magnitudes shown are duration magnitudes for earthquakes with M_D < 3.0 and moment magnitudes for larger events. The last plot includes section lines for the plots in Figure 2-8 (section A-A') and Figure 2-9 (section B-B').

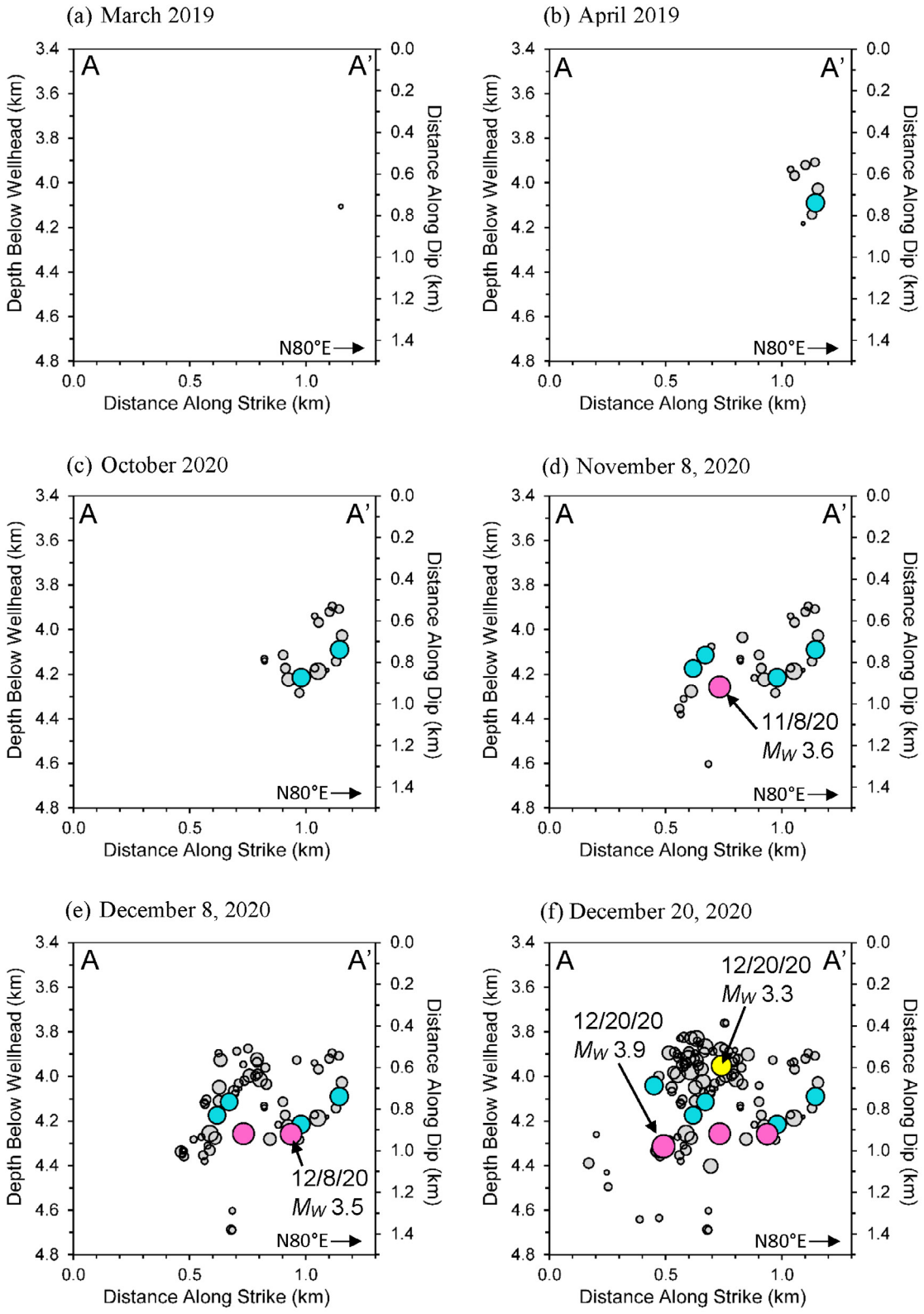

Figure 2-8 – caption on following page.

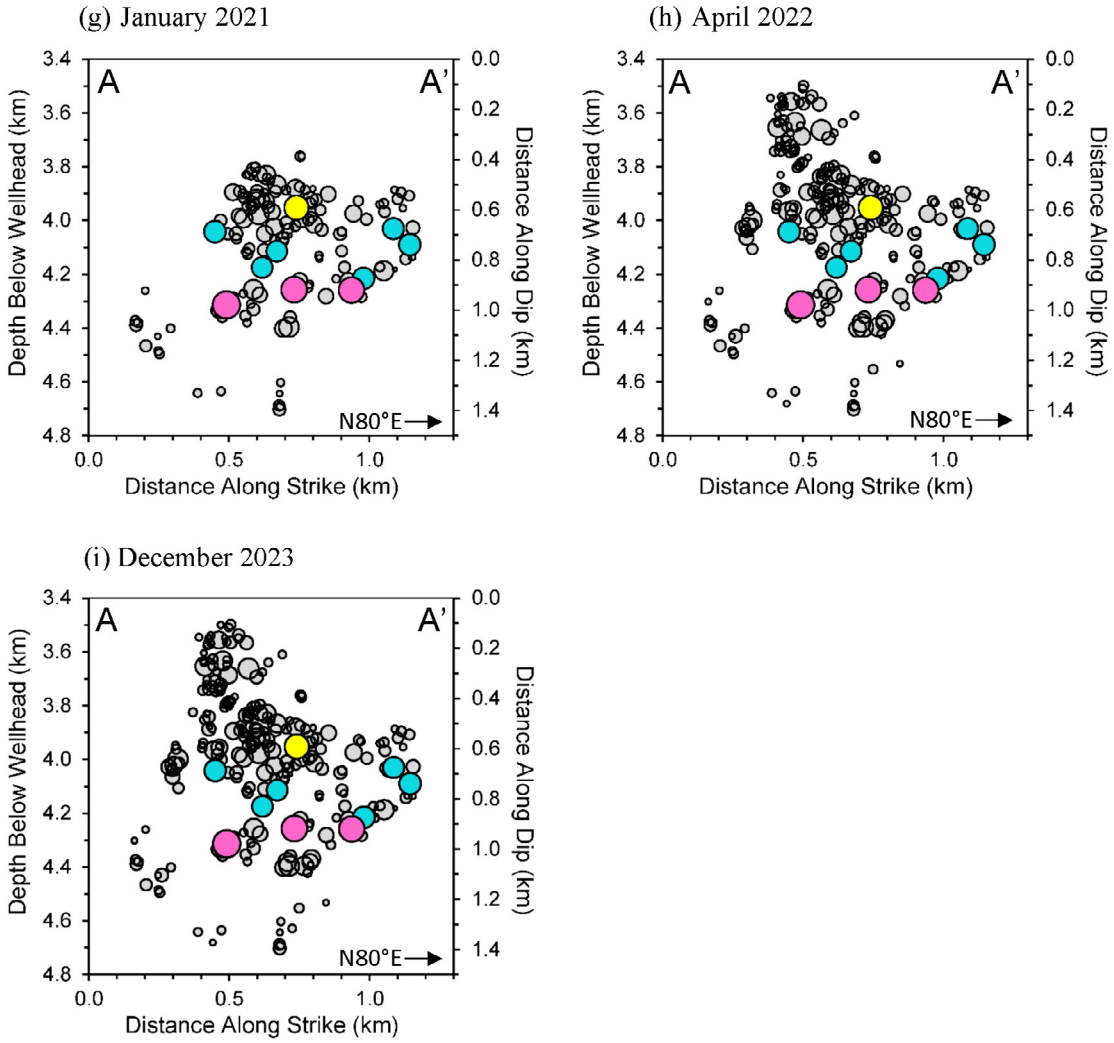

Figure 2-8: Sections over time of a-quality earthquake hypocenters projected into the interpreted fault plane of the fall 2020 seismicity swarm (strike N80°E, dip 69° south). The orientation of these sections is indicated by section line A-A' in Figure 2-7i. The x axis of each plot is along strike, with east to the right, and the y axis is along the fault plane dip, with shallower depths at the top. Depths below the PVU wellhead are included for reference, but the sections are not vertical. Each plot shows the hypocenters of earthquakes recorded from March 2019 through the date listed in the plot heading. Hypocenter symbols are sized by earthquake magnitude, and symbols for larger earthquakes are color-coded: light blue – 2.5 ≤ M < 3.0; yellow – 3.0 ≤ M < 3.5; pink – 3.5 ≤ M < 4.0. The magnitudes shown are duration magnitudes for earthquakes with M_D < 3.0 and moment magnitudes for larger events.

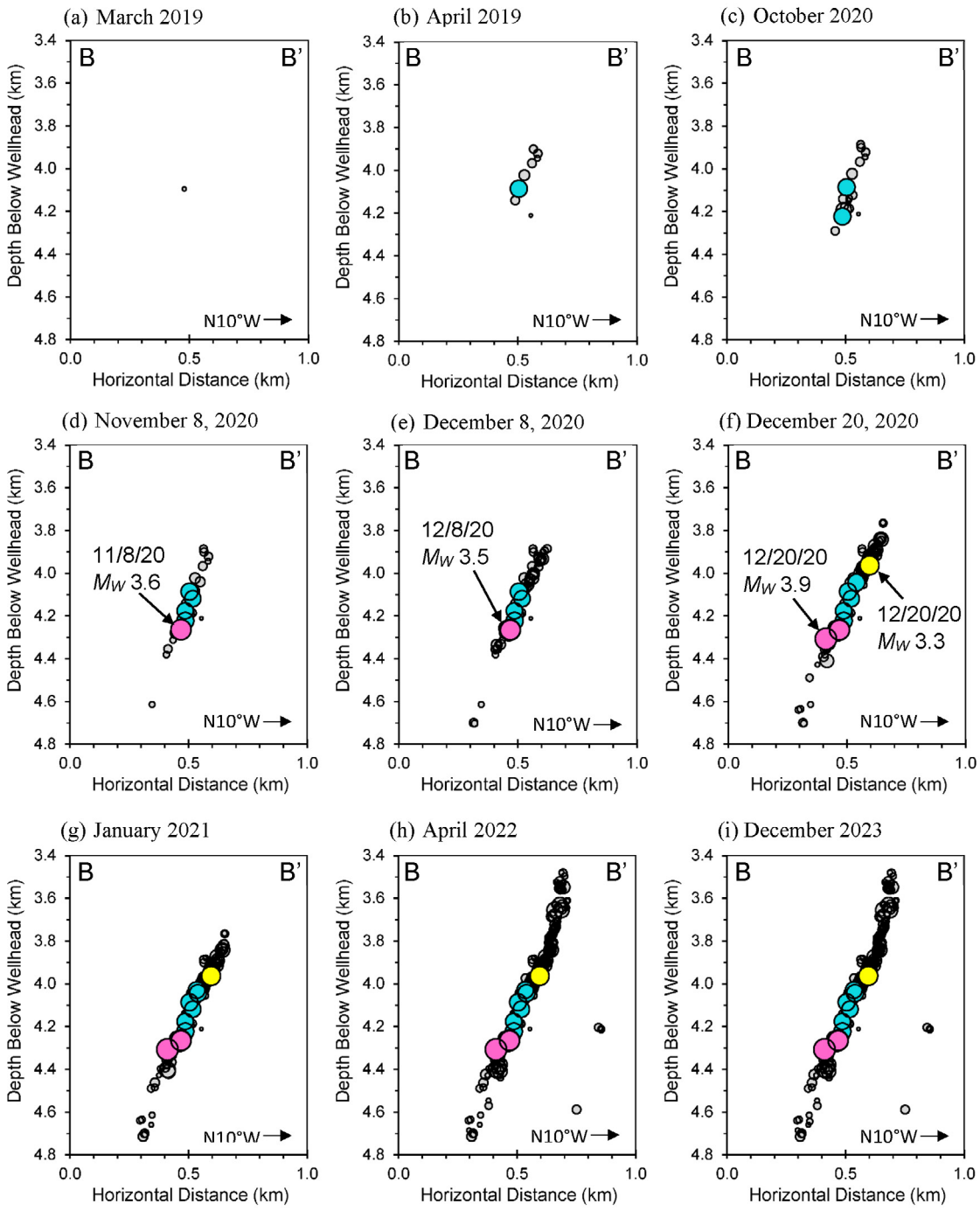

Figure 2-9: Vertical sections over time of a-quality earthquake hypocenters projected perpendicular to the strike of the interpreted fault plane of the fall 2020 seismicity swarm (strike N80°E, dip 69° south). The orientation of these sections is indicated by section line B-B' in Figure 2-7i. Each plot shows the hypocenters of earthquakes recorded from March 2019 through the date listed in the plot heading. Hypocenter symbols are sized by earthquake magnitude, and symbols for larger earthquakes are color-coded: light blue – 2.5 ≤ M < 3.0; yellow – 3.0 ≤ M < 3.5; pink – 3.5 ≤ M < 4.0. The magnitudes shown are duration magnitudes for earthquakes with M_D < 3.0 and moment magnitudes for larger events.

Additional plan view and vertical section hypocenter plots are provided in Appendix A. The plots in the appendix show the position of the hypocenters in the SW cluster relative to aftershocks of the March 2019 M_W 4.5 earthquake occurring on or near its interpreted fault plane. The plots were constructed previously for use in presentations. The plan view plots (maps) were created using the now outdated software *Arcmap*. A license for that software is no longer available, and the plots made with that software are not readily modified or updated. The plots in Appendix A show the expansion of the SW cluster over time through April 2022, relative to the M_W 4.5 fault plane. Interpreted boundaries of major lithologic units are included on the vertical sections. These plots show that the hypocenters in the SW cluster lie at about the same elevation as those along the M_W 4.5 fault plane. However, because of an intervening normal fault with more than 500 m of vertical offset, they occur substantially lower in the stratigraphic column. All of the seismicity in the SW cluster is interpreted to have occurred in the Precambrian basement until March 2022, when the seismicity expanded upward into the lower Cambrian units. The depths to the geologic formations were interpreted from a combination of well log data from the PVU injection well, interpretation of seismic reflection data, and a local hypocenter-velocity inversion of time difference data (Block et al., 2020).

3.0 Relation to Aftershock Activity of the March 2019 M_W 4.5 Earthquake

In this section, the possibility that the seismic activity in the SW cluster represents aftershock activity from the March 2019 M_W 4.5 earthquake is explored. First, the spatial relation of the SW cluster to areas of Coulomb stress transfer from the main shock fault rupture is investigated. Second, seismicity rates in the SW cluster are compared to aftershock rates predicted by the Omori aftershock decay relation.

3.1 Fault Rupture Coulomb Stress Change

3.1.1 Factor-of-Safety

For consistency with the *FLAC3D* geomechanical modeling results discussed below (section 4.0), stress changes associated with the M_W 4.5 fault rupture are presented in terms of changes in the factor-of-safety (FoS). The factor-of-safety is based on the Coulomb failure criterion. The Coulomb failure criterion for a negative compressive stress convention can be represented as (Detournay and Dzik, 2017):

$$(\sigma_1 + p) - (\sigma_3 + p)N_\phi + 2c(N_\phi)^{1/2} \geq 0, \quad (1)$$

where:

σ_1 = maximum compressive stress (most negative principal stress)
σ_3 = minimum compressive stress (least negative principal stress)
p = pore pressure
c = cohesion
$N_\phi = \frac{(1+sin(\phi))}{(1-sin(\phi))}$
ϕ = angle of internal friction = $\tan^{-1}(\mu)$, where μ = the coefficient of internal friction

Rearranging Equation 1, the factor-of-safety is defined as:

$$FoS = \frac{(\sigma_3+p)N\phi+2c(N_\phi)^{1/2}}{(\sigma_1+p)} \leq 1. \quad (2)$$

For these FoS calculations (and the *FLAC3D* model discussed below), cohesion was set to zero. The angle of internal friction, ϕ, was set to 31°, which corresponds to a coefficient of internal friction of 0.6. This value is consistent with the most common orientation of reactivated faults due to PVU injection and the regional maximum horizontal stress direction of N78°W given by the World Stress Map (Block et al., 2015). Different values of ϕ produce substantially different absolute values of FoS but similar geographical and temporal patterns.

Failure is predicted to occur for FoS values ≤ 1 (Equation 2). However, because of the uncertainty in ϕ, as well as uncertainty in initial stress conditions, the absolute FoS value may not be accurate. For this reason, only changes in FoS over time are examined here, rather than absolute values. Decreasing FoS values indicate increasing seismicity potential, while increasing FoS values indicate decreasing seismicity potential.

3.1.2 Procedure

To examine spatial changes in the FoS resulting from the M_W 4.5 fault plane rupture, percent change in FoS was computed at each point on a 3-D grid surrounding a defined fault rupture plane. The general procedure for performing these calculations is given immediately below. Additional procedural details and the model parameter values used for the calculations are provided in the following sub-sections.

First, a pre-rupture initial stress model is constructed. Two simple initial models are considered: a half-space model and a one-dimensional (1-D) model where stresses vary with depth. The stress values and orientations for these initial models are based on previous Reclamation studies and are discussed in the next section. Once the stress tensor for the initial model is constructed, an eigenvalue decomposition of this tensor is performed to determine the principal stress values, σ_1 and σ_3. Pore pressure is computed using a hydrostatic pressure gradient (section 3.1.2.3), and then FoS for the initial model (pre-rupture FoS) is computed using equation 2.

Second, changes in the stress tensor components due to a defined fault rupture are computed. These calculations are performed using an open-source software package that uses an elastic half-space model. Details of these calculations and the fault geometry and rupture parameters used for the modeling are presented in section 3.1.2.2 below.

Third, the stress tensor for the initial model and the stress tensor for the fault rupture are added together, An eigenvalue decomposition of the summed tensor is performed to determine the σ_1 and σ_3 values. Pore pressure is computed using the defined hydrostatic pressure gradient, and then equation 2 is used to compute the post-rupture FoS.

Lastly, the percent difference between and pre- and post-rupture FoS values are computed and plotted.

3.1.2.1 *Initial Model Stress Tensor*

Stress tensors for the two initial models are computed using stress information summarized in a previous Reclamation report (King et al., 2018):

> "The regional *in situ* stress state for the Paradox Valley area is inferred from earthquake focal mechanisms, hypocenter lineations, well log data, and an assumption that the crust is critically stressed. Under these assumptions and interpretations, we infer that the regional

> *in situ* total principal stresses are oriented in the vertical and horizontal directions, with the maximum horizontal stress S_{Hmax} direction approximately N78°W. The magnitude of the total vertical stress S_{Vert} is approximately equal to the lithostatic load, which can be estimated from density logs. Assuming a hydrostatic pore pressure gradient throughout the crust, and a transitional strike-slip to normal faulting stress state, the magnitudes of the total horizontal stresses are estimated by $S_{Hmin} = 0.6 * S_{Hmax}$, $S_{Hmax} = S_{Vert}$."

To compute S_{Vert}, the overburden pressure gradient is first determined using data from the mechanical properties log in the PVU injection well, which indicates an overburden pressure of 16,500 psi at a depth of 14,050 ft (Dewan, 1988; King et al., 2018). This corresponds to an overburden pressure gradient of 26,565 Pa/m. For the half-space initial model, *Svert* is computed using the depth of the center of the modeled fault rupture plane, 4.05 km (section 3.1.2.2). Using the overburden pressure gradient given above, this depth corresponds to an overburden pressure of 107.589 MPa. For the 1-D initial model, a different overburden pressure is computed for each depth in the 3-D grid of points used in the FoS calculations. The vertical stress, $S_{Vert,}$ and by extension, S_{Hmax}, are set equal to the computed overburden pressure (at each point in the grid). S_{Hmin} is then computed by scaling S_{Hmax} by 0.6.

The stress tensor **S** for the initial model, in a coordinate system parallel to the direction S_{Hmax} and for a negative compressive stress convention, is:

$$\mathbf{S} = \begin{pmatrix} -S_{Hmax} & 0 & 0 \\ 0 & -S_{Hmin} & 0 \\ 0 & 0 & -S_{Vert} \end{pmatrix}.$$

This stress tensor is then transformed into a tensor, S', with an East-North orientation by rotating the tensor by $\theta = 12°$ counterclockwise (Roylance, 2001):

$$\mathbf{S'} = \mathbf{A}\,\mathbf{S}\,\mathbf{A}^{\mathbf{T}},$$

where

$$\mathbf{A} = \begin{pmatrix} \cos(\theta) & \sin(\theta) & 0 \\ -\sin(\theta) & \cos(\theta) & 0 \\ 0 & 0 & 1 \end{pmatrix}.$$

3.1.2.2 *Fault Rupture Stress Tensor*

Stress changes caused by rupture of the M_W 4.5 fault plane are computed using the open-source software package *Hdef* (Herman). This package computes stress changes in an elastic half-space defined by P-wave velocity, S-wave velocity, and density. The M_W 4.5 earthquake hypocenter is interpreted to have occurred in the carbonate Leadville formation, which is the primary target formation for PVU injection (Block et al., 2020). Therefore, the material properties for the Leadville layer in PVU's *FLAC3D* geomechanical model were used to specify the half-space parameters (Detournay and Dzik, 2017). The bulk modulus, shear modulus, and density values

for this layer in the *FLAC3D* model were used to compute the corresponding P-wave and S-wave velocities for input into *Hdef*. These values were originally derived from analyses of geophysical well logs acquired in the PVU injection well (Block and Kang, 2024). The parameter values are listed in Table 3-1.

Table 3-1: Half-space parameters used for the *Hdef* model

Parameter	Value
density	2690 kg/m^3
bulk modulus	64.8 GPa
shear modulus	29.2 GPa
P-wave velocity	6210 m/s
S-wave velocity	3295 m/s

The fault plane geometry is defined by the coordinates of its center, its length (along strike), its width (along-dip length), strike azimuth, and dip. The fault rupture is defined by its rake and total slip. These parameters were determined from the spatial distribution of relative hypocenters of the M_W 4.5 earthquake and its aftershocks, focal mechanism analyses, and seismic moment analysis of the main shock (and a simple circular rupture model (Brune, 1970, 1971)). Details of these analyses are found in Block et al. (2020). The values used for the *Hdef* calculations are listed in Table 3-2.

Table 3-2: M_W 4.5 fault geometry and rupture parameters used for the *Hdef* model

Parameter	Value
fault center x – Colorado State Plane Central East coordinate converted to km	616.916 km
fault center y – Colorado State Plane Central North coordinate converted to km	360.189 km
fault center depth (km)	4.05 km
fault length (km)	1.2 km
fault width (km)	0.8 km
strike	60°
dip	60°
rake	171°
total slip (m)	0.27 m

The *o92util* module of the *Hdef* software package is used to compute stress changes caused by the defined fault rupture, at each point in the 3-D grid used for the FoS calculations. A stress tensor is output for each grid point.

3.1.2.3 *Pore pressure*

Pore pressure is computed assuming hydrostatic conditions. (Although pore pressures have increased near the PVU injection well due to more than 20 years of near-continuous injection, the SW cluster is interpreted as being outside the pressurized reservoir (section 1.0).) The regional pore pressure gradient for the Leadville formation determined by Allis et al. (2009) and discussed in King et al. (2018) is used. The reported gradient of 0.47 psi/ft and head of 3900 ft elevation correspond to an intercept of 1188.72 m and slope of 10,631.682 Pa/m for the hydrostatic pressure gradient. When performing FoS calculations using the initial half-space model, a single pore pressure is used. This pressure is computed using the depth of the center of the modeled fault rupture plane (4.05 km). When performing FoS calculations using the initial 1-D model, the pore pressure at each point in the 3-D grid is computed using its depth.

3.1.3 Results

Five horizontal sections showing the percent change in FoS from the modeled M_W 4.5 fault rupture are presented in Figure 3-1 for the initial half-space model and in Figure 3-2 for the initial 1-D model. These horizontal sections span most of the depth range of the SW cluster and are spaced 300 m apart, at depths of: 3.5 km, 3.8 km, 4.1 km, 4.4 km, and 4.7 km. (Depths are relative to the ground surface elevation at the PVU injection well, 1.524 km.) Earthquake hypocenters in the SW cluster within 150 m of each section are projected into the sections (black dots). In these plots, percent change in FoS is shown as a colored raster, with the orange and yellow areas indicating decreased FoS (increased potential for seismicity) and blue areas indicating increased FoS (decreased potential for seismicity).

Results from the initial half-space and 1-D models are very similar. For both models, the plots for all depths indicate that the SW cluster is in an area with decreased FoS (increased seismicity potential). The first earthquake to occur in the SW cluster (in March 2019) has a hypocenter depth of about 4.1 km (Figure 2-9a). It occurred at the east end of the SW cluster (Figure 2-7a and Figure 2-8a). The results from the stress models indicate a decrease in FoS of about 5% to 6% at this location (Figure 3-1c, Figure 3-2c). The magnitudes of the FoS changes in more westerly and shallower and deeper parts of the SW cluster are less. The smallest changes in FoS in the SW cluster are decreases of about 0.4%.

These results indicate that the SW cluster lies in an area that experienced increased potential for seismicity due to Coulomb stress transfer from the fault rupture associated with the March 2019 M_W 4.5 earthquake.

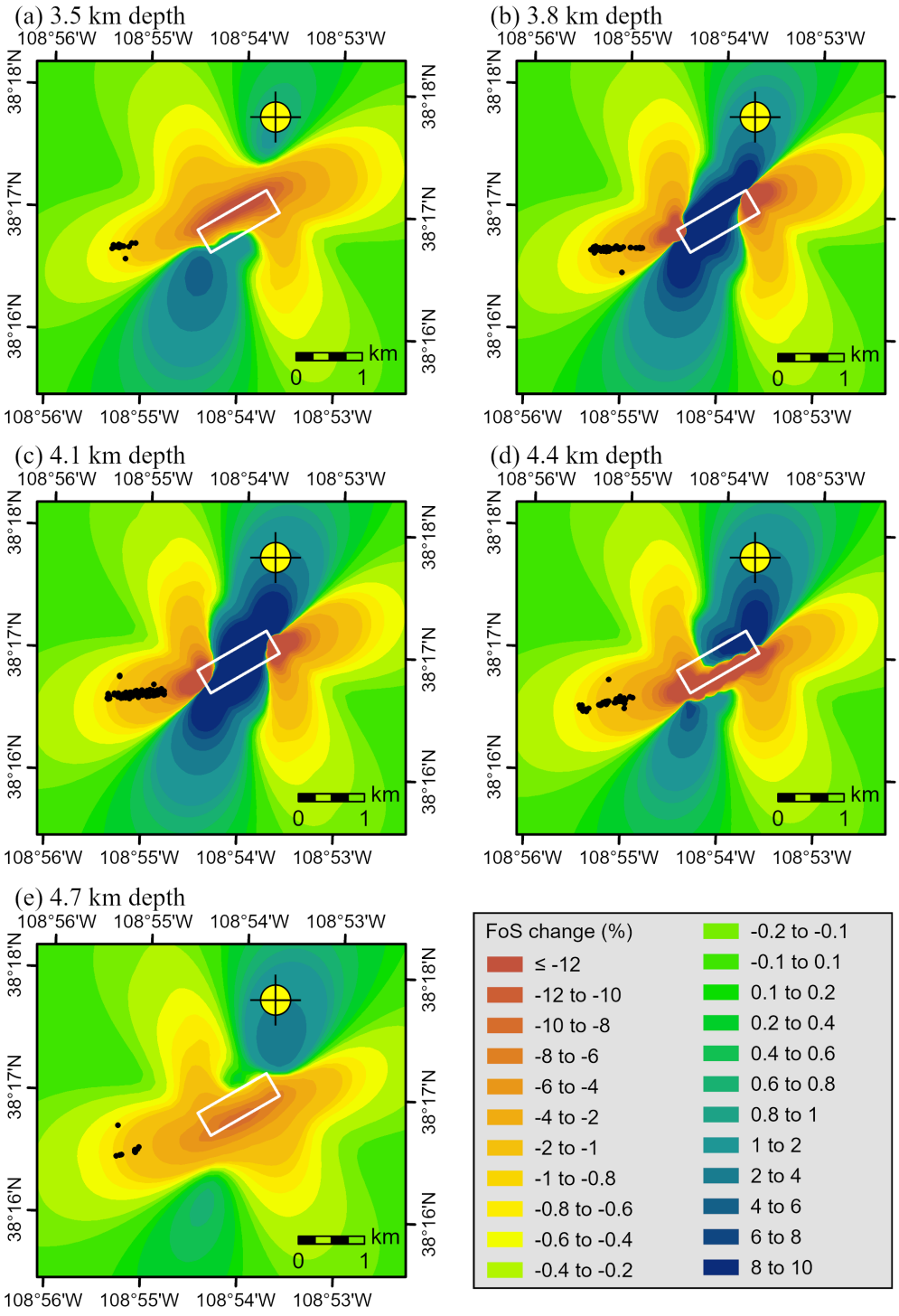

Figure 3-1: Percent change in FoS from the March 2019 *Mw* 4.5 earthquake fault rupture, based on the initial half-space model described in the text. Horizontal sections are shown for the five depths indicated. The black dots are earthquake hypocenters in the SW cluster within 150 m of each section. The yellow circle with crosshairs is the PVU injection well, and the white rectangle is the modeled fault rupture plane.

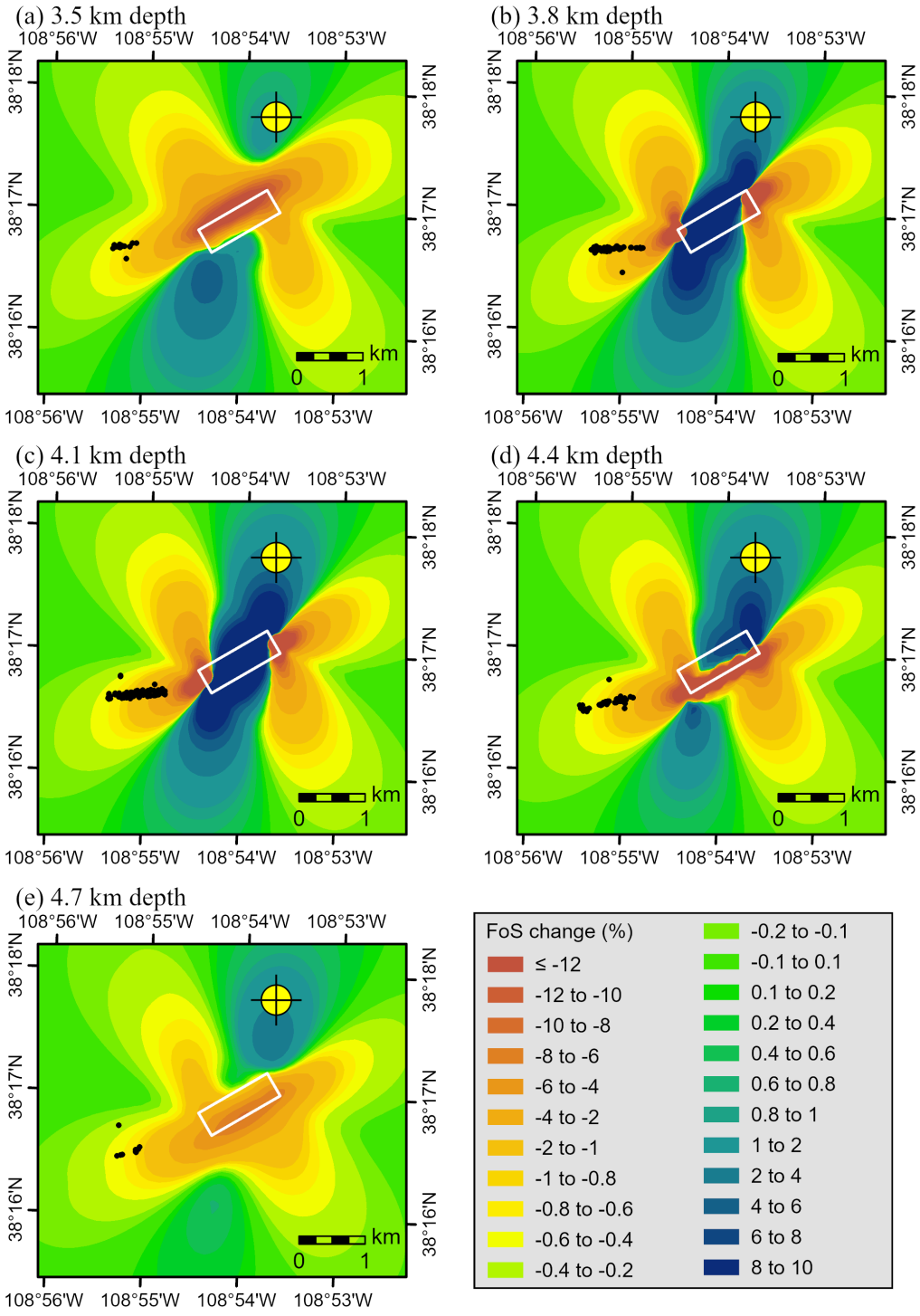

Figure 3-2: Percent change in FoS from the March 2019 M_W 4.5 earthquake fault rupture, based on the initial 1-D model described in the text. Horizontal sections are shown for the five depths indicated. The black dots are earthquake hypocenters in the SW cluster within 150 m of each section. The yellow circle with crosshairs is the PVU injection well, and the white rectangle is the modeled fault rupture plane.

3.2 Aftershock Rates

Rates of aftershocks from the March 2019 M_W 4.5 earthquake over time were analyzed by Block et al. (2020), using the modified Omori rate law:

$$n(t)=K\,(t+c)^{-p},$$

where n(t) is the rate of aftershocks at time t, and K, c, and p are constants. Block et al. (2020) fit the modified Omori relation to aftershocks of the M_W 4.5 earthquake recorded from the time of the main event to the end of July 2019. These computations were done for five magnitude thresholds, and the results are shown in Figure 3-3. The corresponding parameter values for the Omori relations are listed in Table 3-3. The value of *p*, which indicates how quickly the aftershock rate declines over time, varies from 0.83 to 0.92 for the five fits, with a mean value of 0.88 and median value of 0.87.

Table 3-3: Omori parameters computed from the aftershock data of the M_W 4.5 earthquake, for five magnitude thresholds. Aftershocks recorded between the time of the main shock (3/4/2019) and the end of July 2019 were included in the analyses. Table from Block et al. (2020).

Threshold Magnitude (M_D)	Number of Aftershocks Included	*K*	*c*	*p*
-0.5	1416	133.500	0.034	0.831
0.0	641	68.295	0.066	0.869
0.5	247	28.660	0.094	0.895
1.0	111	12.595	0.055	0.919
2.0	20	1.990	0.002	0.864

To evaluate how the rates of earthquakes occurring in the SW cluster compare to the aftershock rates predicted by the Omori relation, the predicted cumulative number of aftershocks through December 2022 were computed using the parameter values derived previously (Table 3-3). These predicted numbers of aftershocks were then compared to the observed cumulative numbers of aftershocks, for two scenarios. One scenario included the earthquakes in the SW clusters as assumed aftershocks and the other scenario excluded them. These calculations were originally performed for the five magnitude thresholds used in Table 3-3. However, because PVSN's detection of very small earthquakes may have varied over time, results for a magnitude threshold of M_D -0.5 are not presented here. Likewise, results for the largest magnitude threshold, M_D 2.0, are excluded because of the small numbers of earthquakes in this data set.

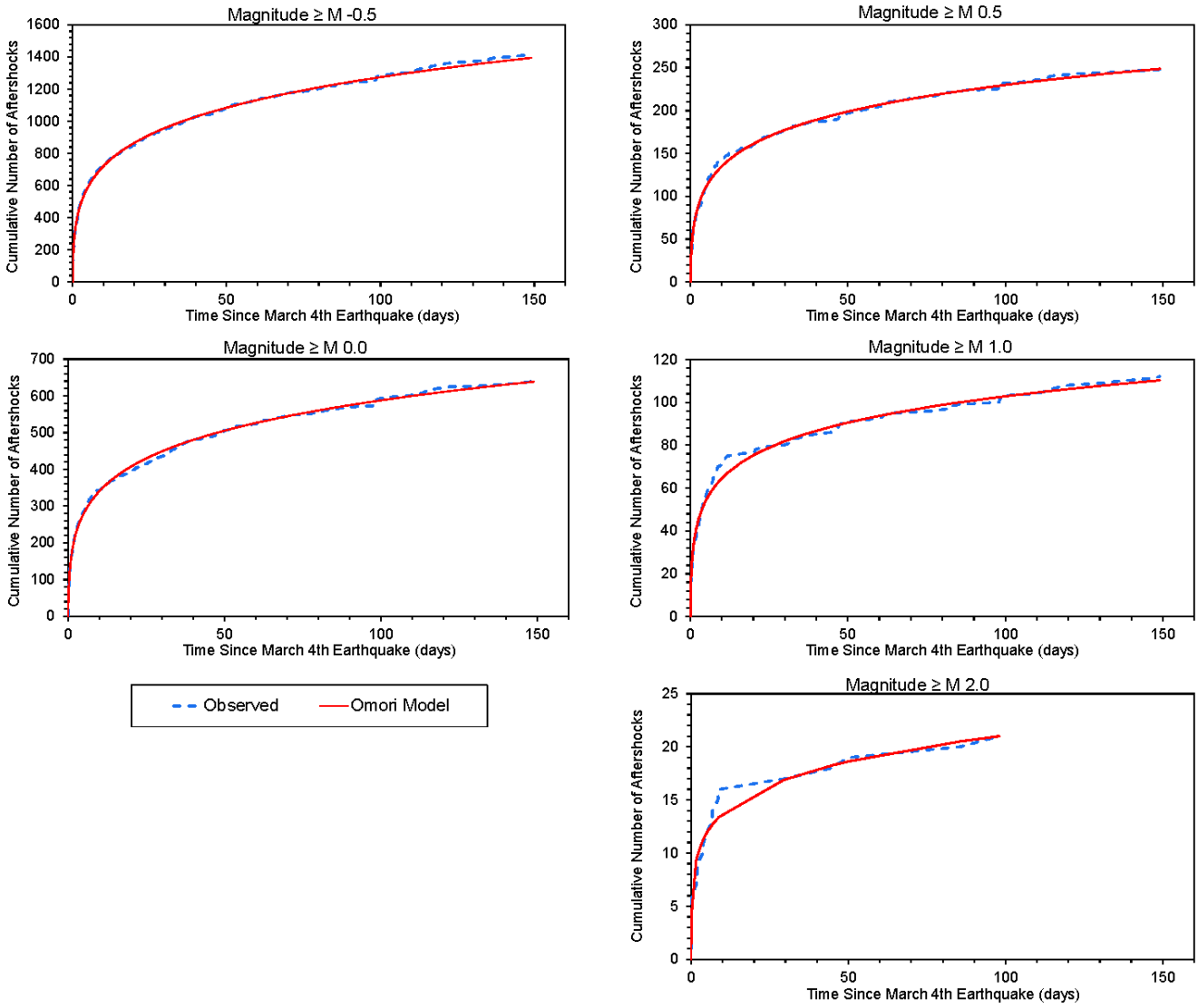

Figure 3-3: Fit of the Omori model to the cumulative number of aftershocks from the M_W 4.5 earthquake recorded through July 2019. Results are shown for five magnitude thresholds; all magnitudes are duration magnitudes. The fit for aftershocks with magnitudes ≥ M_D 2.0 only extends to 98 days after the main shock because no aftershocks with M_D ≥ 2.0 were recorded between mid-June and the end of July. Figure from Block et al. (2020).

Events in the vicinity of the March 2019 M_W 4.5 earthquake were selected for inclusion in the original aftershock analyses based on the following geographic bounds: latitude 38.257° to 38.317° and longitude -108.95° to -108.85° (Block et al., 2020). The same geographic area was used for the calculations of the cumulative numbers of aftershocks through December 2022. This selection may include some near-well induced earthquakes that are not aftershocks of the M_W 4.5 earthquake. However, since the vast majority of earthquakes that occurred in this area between March 2019 and December 2022 have hypocenters close to the interpreted M_W 4.5 fault plane, any non-aftershock events included would constitute a small percentage of the data. The earthquakes used in the first scenario, which includes events in the SW cluster, are shown on the map in Figure 3-4a (colored circles). The earthquakes for the second scenario, which excludes events in the SW cluster, are shown in Figure 3-4b. In both plots, the earthquakes included in the aftershock analyses are color-coded by hypocenter depth. The SW cluster events are the relatively deep hypocenters labeled in Figure 3-4a. The shallower earthquakes in the same geographic location are retained in both scenarios.

The observed and predicted cumulative numbers of aftershocks for both scenarios are presented in Figure 3-5. Results for the first scenario, which includes the SW cluster, are presented on the left, for the three magnitude thresholds used. Results for the second scenario, which excludes the SW cluster, are presented on the right. These results demonstrate that the observed aftershock rates match the aftershock rates predicted by the Omori relation very well if earthquakes in the SW cluster are excluded (Figure 3-5, plots on right). However, when earthquakes in the SW cluster are included, the observed aftershock rates deviate abruptly from the predicted rates in late 2020. After 2020, the two curves approximately parallel one another. These results indicate that the high seismicity rates in the SW cluster during the fall 2020 seismicity swarm are not consistent with the Omori aftershock decay relation.

3.3 Discussion

The results from the two types of analyses performed to evaluate whether the earthquakes in the SW cluster represent normal aftershock activity of the March 2019 M_W 4.5 earthquake are inconsistent. The results from the stress models clearly indicate that the SW cluster lies in an area that experienced increased potential for seismicity due to Coulomb stress transfer from the fault rupture associated with the March 2019 M_W 4.5 earthquake. In addition, the initial earthquake in the SW cluster occurred in the area of greatest decrease in FoS, a few weeks after the main shock. However, the results from the Omori aftershock rate analyses clearly indicate that the rate of seismicity that occurred in the SW cluster during the fall 2020 seismicity swarm is much too high to be consistent with normal aftershock activity. Hence, these analyses suggest that seismicity in the SW cluster initially began in March 2019 as aftershock activity of the M_W 4.5 earthquake but that other factors contributed to the greatly increased rates observed in late 2020.

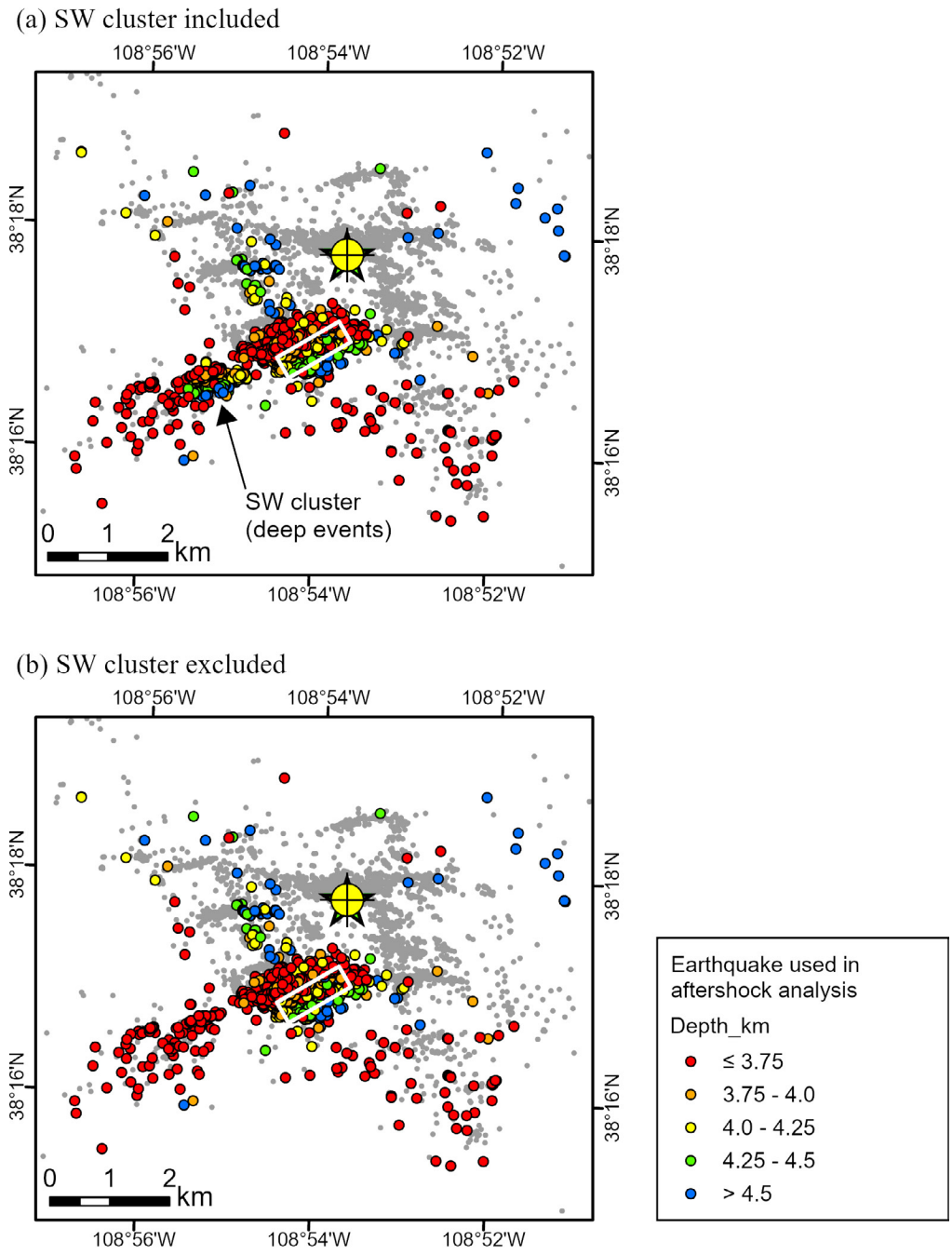

Figure 3-4: Earthquakes included in the observed cumulative numbers of aftershocks: (a) scenario #1 - including the SW cluster (b) scenario #2 - excluding the SW cluster. The events used in the analyses are color-coded by hypocenter depth. The gray dots are events that occurred prior to the March 2019 M_W 4.5 earthquake. The yellow circle with crosshairs is the PVU injection well, and the white rectangle represents the M_W 4.5 fault plane.

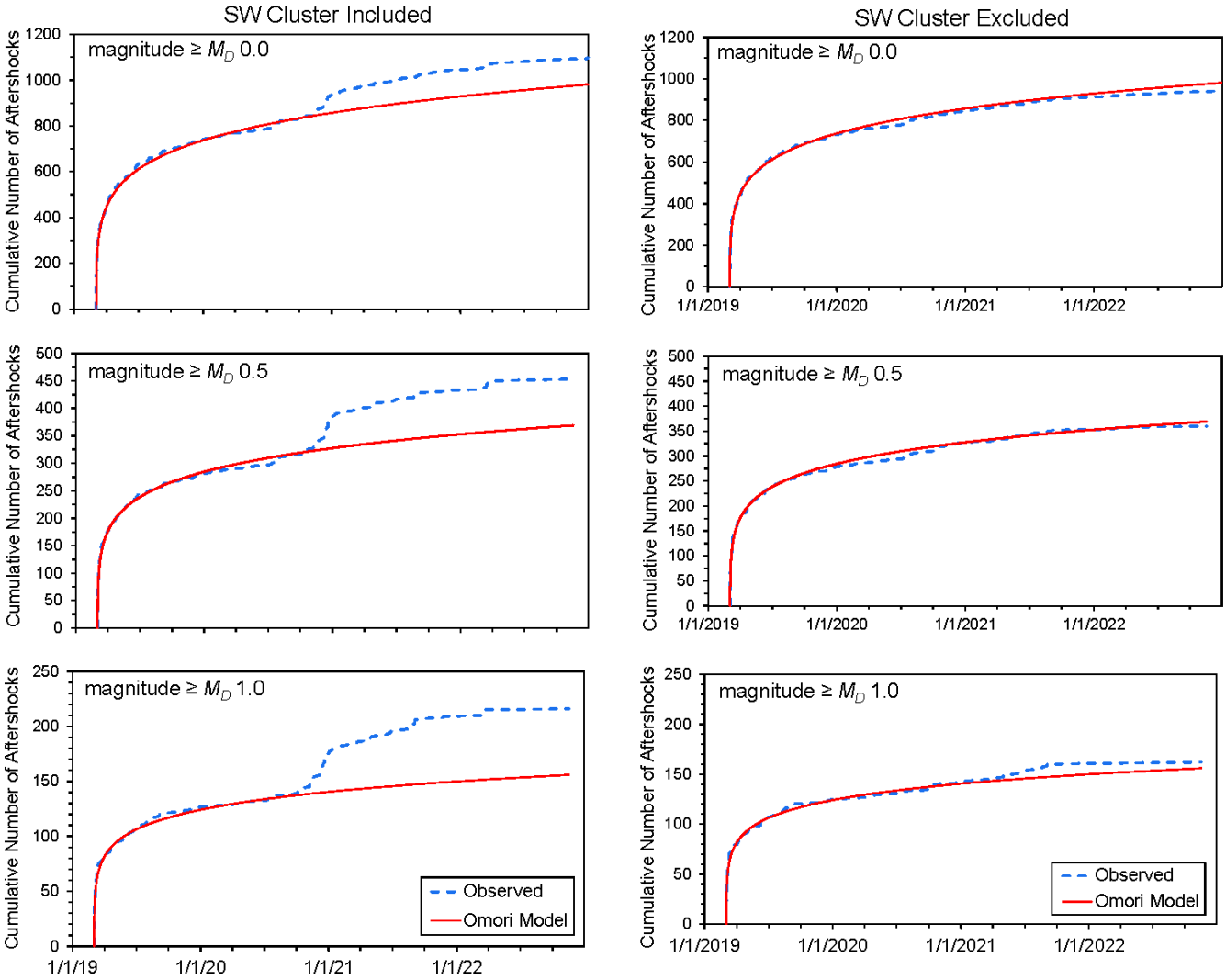

Figure 3-5: Predicted and observed cumulative numbers of aftershocks over time for three magnitude thresholds (M_D 0.0, 0.5, and 1.0). For the plots on the left, the earthquakes in the SW cluster are included in the observed numbers of aftershocks; for the plots on the right, they are excluded. The predicted numbers of aftershocks were computed using the Omori relations defined by the parameters in Table 3-3, which were determined previously using data from March to July 2019 (Block et al., 2020). The observed data include earthquakes recorded from March 2019 to December 2022.

.

4.0 Coulomb Stress Transfer from Large Earthquakes in the SW Cluster

The fall 2020 seismicity swarm produced four earthquakes with magnitude ≥ M_W 3.0 (M_W 3.0+). Coulomb stress transfer from the fault ruptures associated with these earthquakes may have contributed to the end of the swarm activity in early January 2021. Changes in the factor-of-safety from the fault ruptures of these four earthquakes were computed in the same way as for the M_W 4.5 earthquake, using the *Hdef* software. For this analysis, only the halfspace model was used (Table 3-1). The fault geometry and rupture parameters used for the fault characterizations are listed in Table 4-1. Total slip and rupture area were determined from seismic moment analyses of the earthquakes (using a simple circular rupture model). Rectangular fault planes were then constructed centered on the earthquake hypocenters. The fault lengths were set equal to 1.5 times the fault widths, and both were adjusted to honor the fault areas from the moment analyses. The fault strikes, dips, and rakes used for this analysis were determined from preliminary event relative locations and manually determined earthquake focal mechanisms, prior to completion of the more thorough analyses discussed previously (section 2.3). The average rake from the four earthquake focal mechanisms (169°) was used for all rupture models. A single fault strike of 80° and dip of 66° were used, based on preliminary analysis of relative event locations. The strike, dip, and rake used for these rupture models are within a few degrees of the values determined later from more in-depth analyses (section 2.3).

Table 4-1: Fault geometry and rupture parameters used for the *Hdef* model for the SW-cluster earthquakes with magnitude ≥ M_W 3.0

Parameter	11/8/2020 M_W 3.6	12/8/2020 M_W 3.5	12/20/2020 M_W 3.3	12/20/2020 M_W 3.9
fault center x – Colorado State Plane Central East coordinate converted to km	615.379	615.581	615.370	615.148
fault center y – Colorado State Plane Central North coordinate converted to km	359.631	359.660	359.758	359.541
fault center depth (km)	4.264	4.266	3.963	4.307
fault length (km)	0.860	0.684	0.647	1.164
fault width (km)	0.573	0.456	0.431	0.776
strike	80°	80°	80°	80°
dip	66°	66°	66°	66°
rake	169°	169°	169°	169°
total slip (m)	0.021	0.022	0.011	0.031

Stress tensors from the initial halfspace model, the March 2019 M_W 4.5 fault rupture, and the four M_W 3.0+ fault ruptures within the SW cluster were summed, and then the FoS was computed. The results are presented in Figure 4-1. These results indicate that the fault ruptures that produced the largest earthquakes during the fall 2020 seismicity swarm transferred Coulomb stress away from the interpreted fault in the SW cluster at the fault plane mid-depths (4.1 to 4.4 km, Figure 4-1 c and d). Near the top and bottom portions of the fault plane, however, increased Coulomb stress (FoS decrease) from the M_W 4.5 earthquake remains (Figure 4-1 a, b, and e). These results suggest that seismic activity in the SW cluster since the fall 2020 seismicity swarm is mostly likely to occur at the upper and lower margins of the fault plane. This interpretation is consistent with the observed expansion of the seismicity upward along the interpreted fault plane in March 2022 (Figure 2-8h).

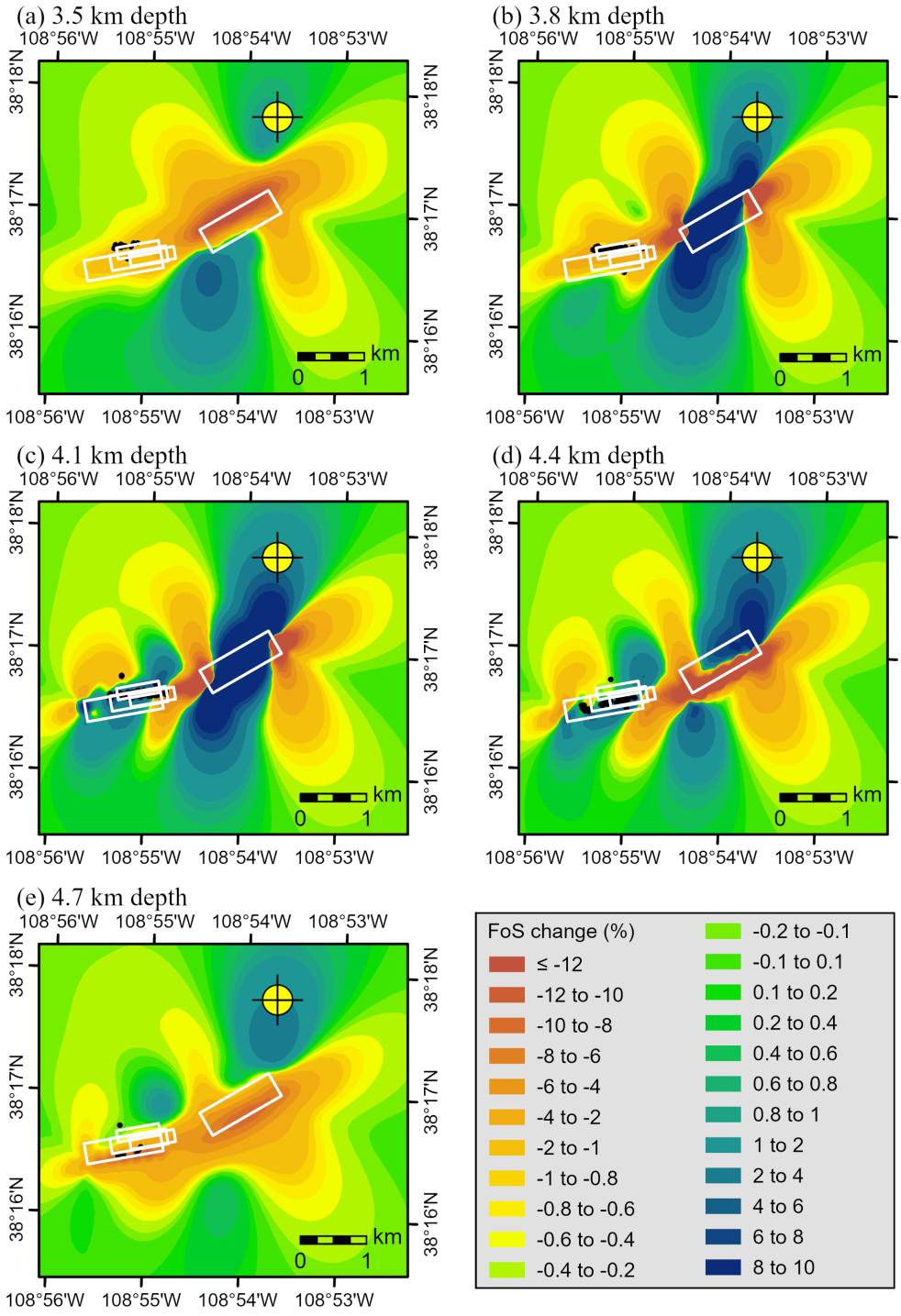

Figure 4-1: Percent change in FoS from the fault ruptures of the March 2019 M_W 4.5 earthquake and the four earthquakes with $M_W \geq 3.0$ that occurred in the SW cluster during the fall 2020 seismicity swarm. The initial half-space model was used (Table 3-1). Horizontal sections are shown for the five depths indicated. The white rectangles are the modeled fault rupture planes. The yellow circle with crosshairs is the PVU injection well.

5.0 Geomechanical Modeling of PVU Injection

To determine whether PVU injection operations may have contributed to the occurrence of the fall 2020 seismicity swarm, flow and geomechanical modeling of PVU injection was performed. For this study, the model is used to specifically investigate whether stress changes associated with the extended shut-in of the PVU injection well, which began on March 4, 2019, may have contributed to increased seismicity rates in the SW cluster in the fall of 2020. In addition, stress changes associated with the five-week injection test conducted in April-May 2020 are evaluated for any potential relation to the seismicity swarm. The temporal relation between injection operations and the rate of seismicity in the SW cluster is illustrated in Figure 5-1.

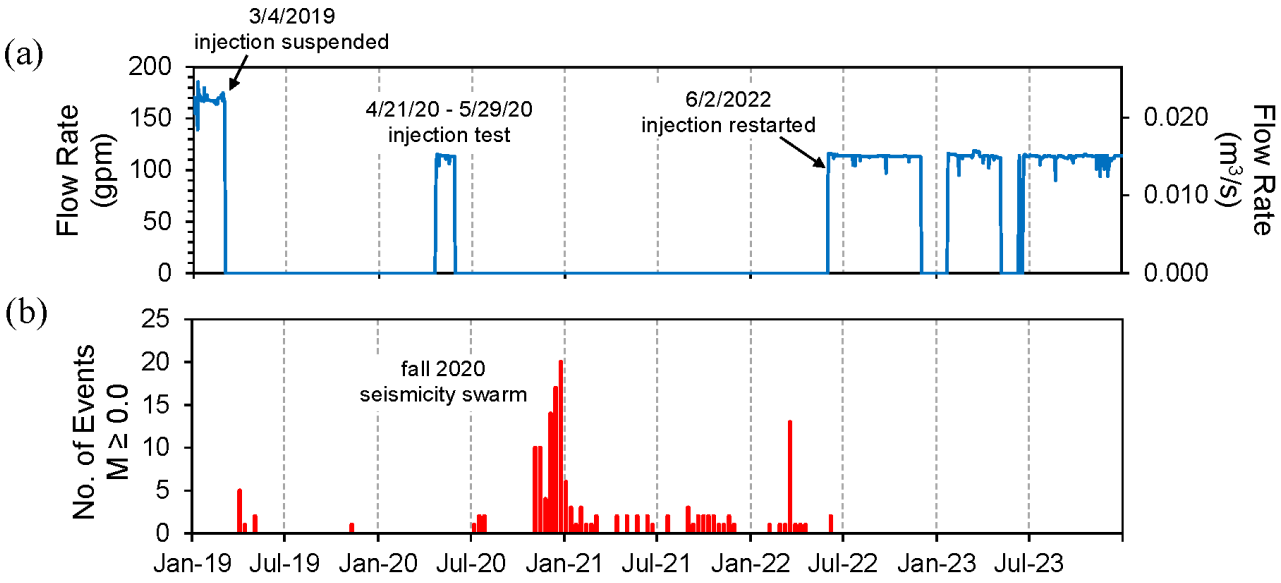

Figure 5-1: (a) PVU injection flow rate (b) rates of events in the SW cluster with magnitude ≥ M_D 0.0. The seismicity rates were computed using 10-day (non-overlapping) bins.

The PVU coupled geomechanical-flow model was originally developed by Itasca Consulting Group, under contract to Reclamation. The model was constructed using *FLAC3D*, a three-dimensional finite-volume numerical modeling software package (Itasca Consulting Group, 2018). The model is formulated as saturated single-phase porous-medium flow, with elastic material deformation. The coupled problem is solved by iterating between the flow solution and the mechanical solution. The model was developed initially for use in evaluating proposed sites for a potential second PVU injection well (Detournay and Dzik, 2017). The following year, additional modeling was performed under a follow-up contract to increase the resolution of the model in the vicinity of the current PVU injection well and to improve the calibration of the model with the historical PVU injection data (Detournay, 2018). Since then, additional model

simulations have been performed by Reclamation to evaluate the effect of PVU operations on the potential for induced seismicity (Block and Kang, 2024).

Faults with more than 500 ft of vertical offset are treated as impermeable barriers in the *FLAC3D* model (Detournay and Dzik, 2017). These faults extend vertically throughout the entire model. Hence, increased pore pressures near the PVU injection well cannot diffuse across these fault barriers. The SW cluster lies on the far side of one of these impermeable faults (Figure 1-1), and therefore pore pressures cannot diffuse from the PVU injection well to the location of the SW cluster. Therefore, this study only investigates changes in stress conditions. The results are presented in terms of percent change in the factor-of-safety (section 3.1.1).

5.1 Injection Well Shut-in

Changes in the factor-of-safety following the extended injection well shut-in are presented as a series of time-lapse maps in Figure 5-2. These maps show the percent change in FoS at a depth of 4.1 km from the day prior to the extended injection well shut-in (3/3/2019) through the date in each plot heading. The end dates range from 6/30/2019 to 11/7/2020, the day prior to the beginning of the fall 2020 seismicity swarm. The cool colors (blue and green) indicate areas where FoS increased; the warm colors (pink) indicate areas where FoS decreased; gray indicates areas where the FoS change was less than 0.1%. The color scale is not linear – the increment between adjacent colors varies from 0.1% (for small values) to 2.0% (for large values). A depth of 4.1 km was chosen because it is the depth where the first earthquake in the SW cluster occurred and is also the approximate mid-depth of the final cluster extent (Figure 2-9). The black lines on the maps are faults at the top of the Precambrian basement, interpreted from seismic reflection studies (Arestad, 2016). The thick white line is the impermeable fault as represented in the *FLAC3D* model. Earthquakes in the SW cluster (with a-quality hypocenters) that occurred up to the end date listed in each plot heading are shown as black dots.

These maps generally show increasing FoS on the northeast side of the impermeable fault (blue and green colors) and decreasing FoS on the southwest side (pink colors). The FoS patterns are somewhat complex on the northeast side of the fault because the horizontal section cuts through different layers in the FLAC3D model, which are slightly dipping toward the northeast. Some of these layers are pressurized by PVU injection (blue and green areas) and some of the layers are above the Paradox salt confining layer and do not experience pore pressure changes from PVU injection (gray areas). The model results show FoS values increasing on the northeast side of the impermeable fault within the pressurized reservoir formations after the injection well was shut in, as pore pressures gradually decreased. On the southwest side of the impermeable fault, where the SW cluster lies, the horizontal section is within the lower Precambrian layer in the *FLAC3D* model and the FoS pattern is less complex. The model shows FoS values here gradually decreasing over time following the injection well shut-in. This decrease first occurs near the impermeable fault (Figure 5-2a, b) and gradually spreads toward the southwest, including the area of the SW cluster (Figure 5-2c, d, e). Since the impermeable fault in the *FLAC3D* model

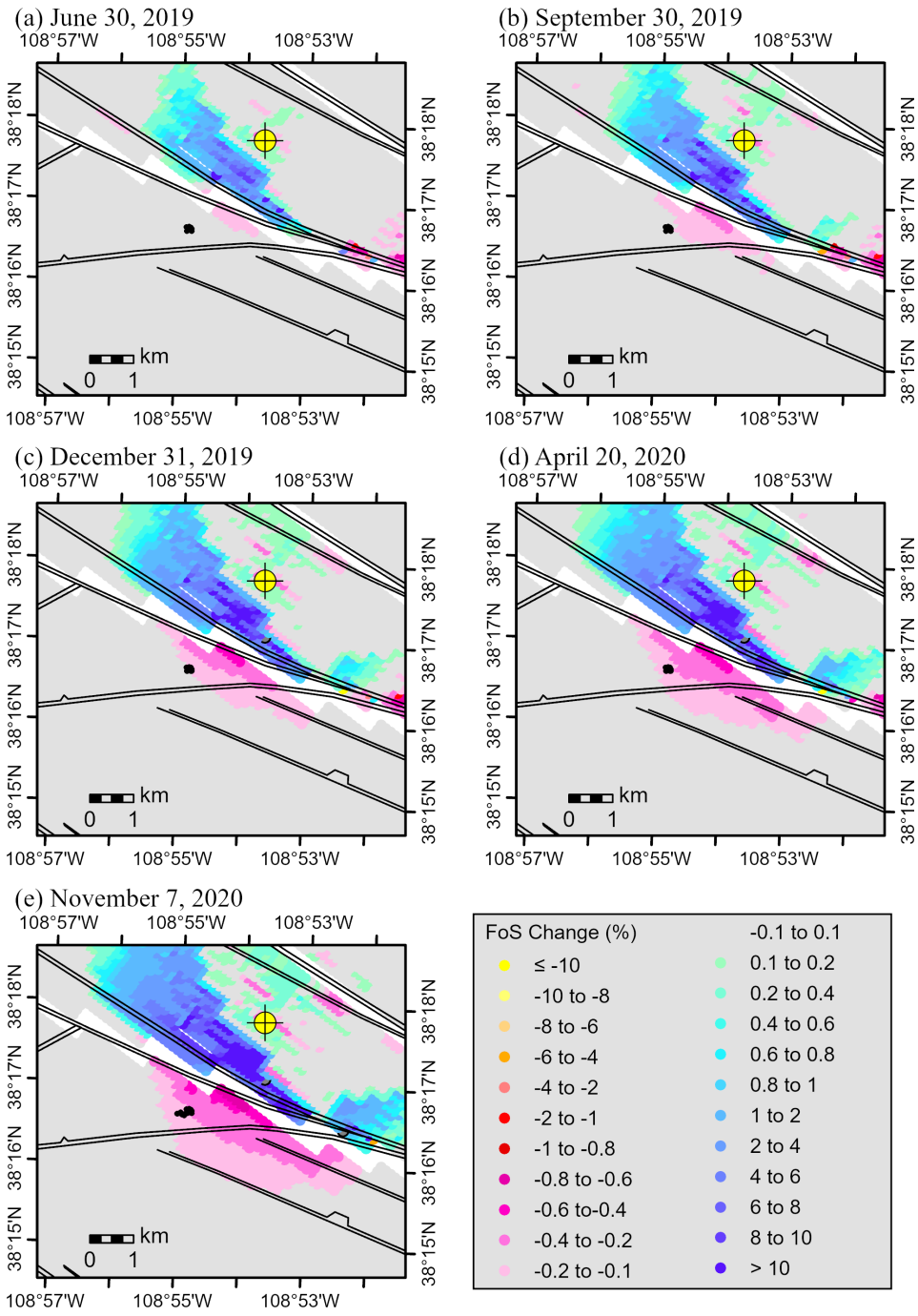

Figure 5-2: Horizontal sections at 4.1 km depth of the percent change in FoS from the day before the extended PVU injection well shut-in (3/3/2019) through dates prior to the beginning of the fall 2020 seismicity swarm: (a) 6/30/2019, (b) 9/30/2019, (c) 12/31/2019, (d) 4/20/2020 (day prior to the injection test), and (d) 11/7/2020 (day prior to the start of the seismicity swarm). The black dots are a-quality earthquake hypocenters in the SW cluster through the date in the plot heading. The black lines are faults at the top of the Precambrian basement interpreted from seismic reflection data (Arestad, 2016), and the thick white line is the impermeable fault in the *FLAC3D* model. The yellow circle with crosshairs is the PVU injection well.

prevents pore pressure diffusion across it, changes in FoS in this area are due solely to stress changes. Hence, following the suspension of PVU injection in March 2019, stresses on the southwest side of the impermeable fault changed over time in a way that caused seismicity to become more likely.

The series of time-lapse maps in Figure 5-3 show how the FoS patterns (at a depth of 4.1 km) continued to evolve after November 2020. These maps show the percent change in FoS from 3/3/2019 to end dates ranging from 6/30/2021 to 12/31/2023. The model indicates that the zone of decreased FoS values on the southwest side of the impermeable fault continued to spread slowly until about June 2022, when it stabilized. There is no noticeable change in FoS from June 2022 through the last date examined, December 2023. The mid-2022 date when the FoS values stopped changing correlates with the resumption of PVU injection and the abrupt decrease in seismicity in the SW cluster (Figure 5-1).

The temporal changes in FoS near the SW cluster are examined more precisely using data from monitoring points in the *FLAC3D* model. These monitoring points are specified locations where the model parameters are saved every 20 days in the simulation. From this data, histories of FoS over time at each point are constructed. For this study, two monitoring points on the southwest side of the impermeable fault were specified (Figure 5-4). The point named *West of Fault* is very close to the impermeable fault, while the point named *SW cluster* is near the eastern end of the SW cluster. There is uncertainty in both the location of the impermeable fault, which was interpreted from sparse seismic reflection data, and in the absolute locations of the earthquakes. Previous analyses suggest that the earthquake hypocenters may need to shift a little farther east relative to the impermeable fault (or the fault needs to shift west relative to the hypocenters) (Block et al., 2020). FoS histories at the two different monitoring points are examined because of this uncertainty in the relative positions of the fault and hypocenters.

The FoS histories from both monitoring points show similar trends (Figure 5-4). These histories are presented as percent change in FoS relative to 3/3/2019, similar to the maps discussed previously. They illustrate that FoS at the monitoring points started decreasing shortly after PVU injection was suspended on March 4, 2019. The FoS decrease was approximately linear until June 2022 (or shortly after), when PVU injection resumed. Since mid-2022, FoS at the *SW cluster* monitoring point has been nearly constant, while FoS at the *West of Fault* monitoring point has increased slightly. The changes in FoS indicated by the *FLAC3D* simulations for the time periods examined are small, only a few tenths of a percent.

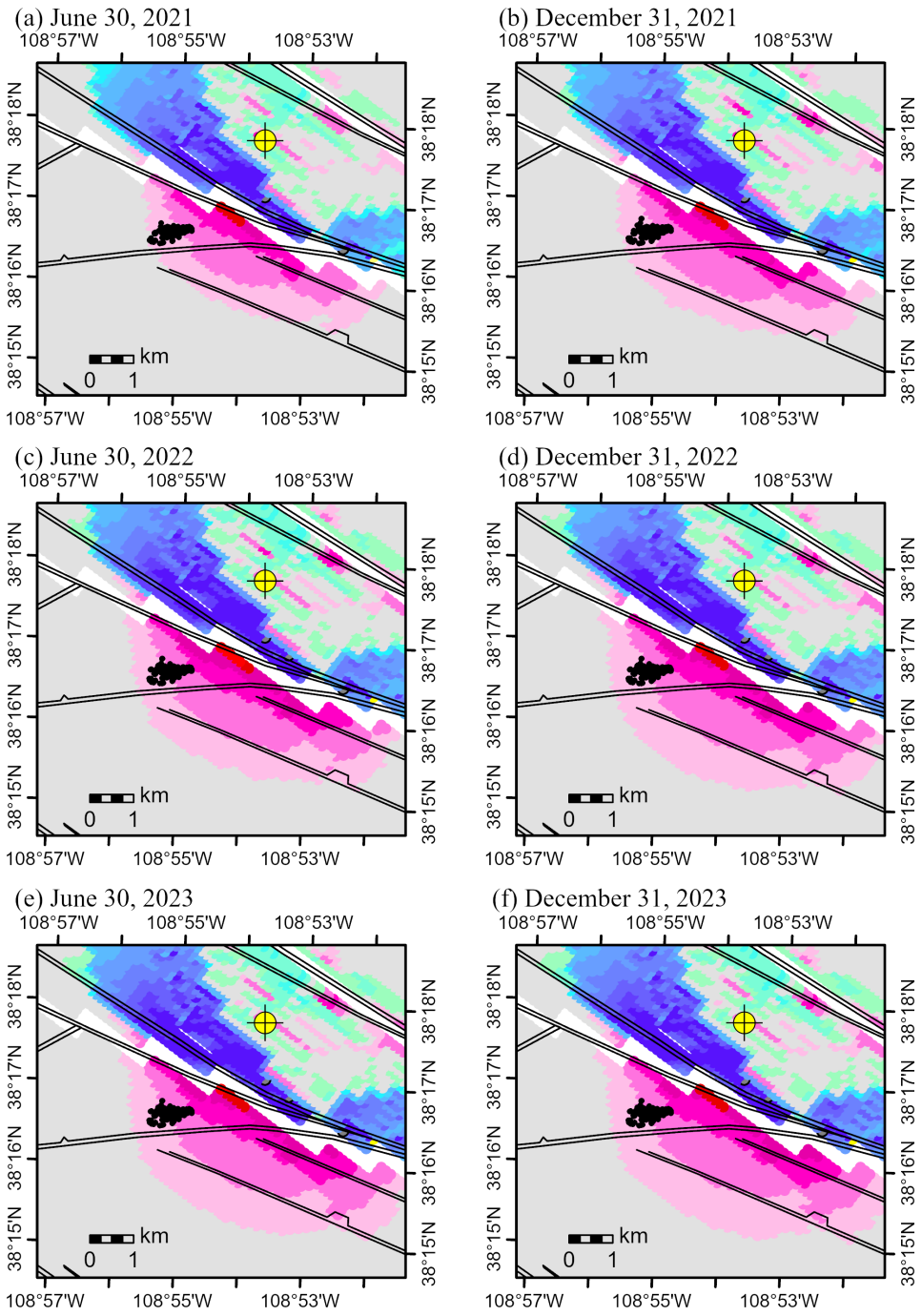

Figure 5-3: Horizontal sections at 4.1 km depth of the percent change in FoS from the day before the extended PVU injection well shut-in (3/3/2019) through dates after the fall 2020 seismicity swarm: (a) 6/30/2021, (b) 12/31/2021, (c) 6/30/2022, (d) 12/31/2022, (e) 6/30/2023, and (f) 12/31/2023. See legend in Figure 5-2 for FoS values. The black dots are a-quality earthquake hypocenters in the SW cluster through the date in the plot heading. The black lines are faults at the top of the Precambrian basement interpreted from seismic reflection data (Arestad, 2016), and the thick white line is the impermeable fault in the *FLAC3D* model. The yellow circle with crosshairs is the PVU injection well.

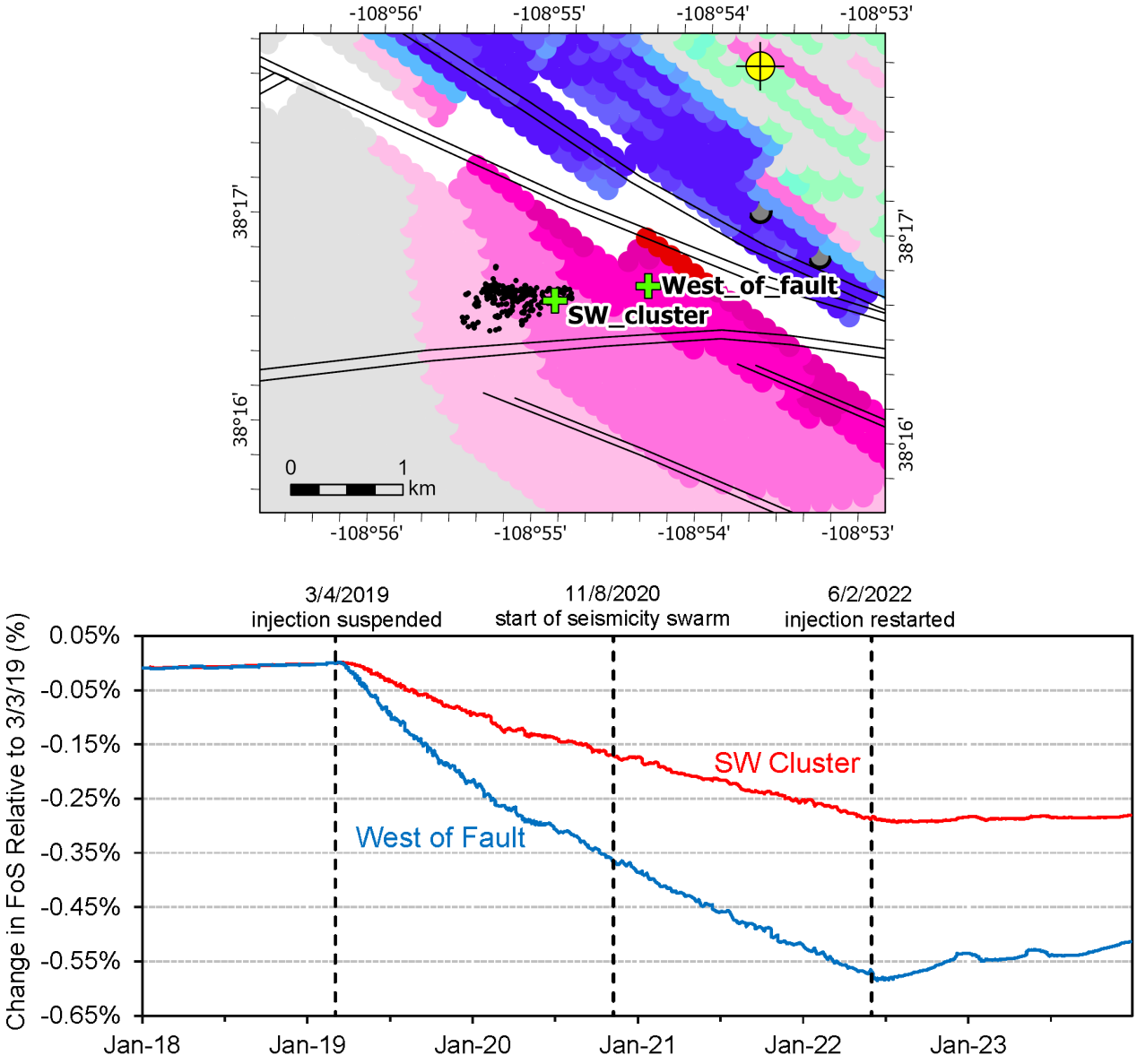

Figure 5-4: FoS histories at two *FLAC3D* monitoring points southwest of the impermeable fault. The locations of the monitoring points are indicated by the green plus symbols on the map. The map shows the percent change in FoS from 3/3/2019 to 12/31/2023 (same as Figure 5-3f). The FoS histories are presented as percent changes in FoS over time relative to the value prior to the extended PVU injection well shut-in (3/3/2019). Small fluctuations in the curves may be due to noise in the numerical model (from discretization and/or incomplete convergence). Dates indicated by the vertical black dashed lines are: 3/4/2019 - PVU injection was suspended; 11/8/2020 - the fall 2020 seismicity swarm began; and 6/2/2022 - PVU injection was resumed.

5.2 April-May 2020 Injection Test

To evaluate the effect of the April-May 2020 injection test on FoS in the area of the SW cluster, the *FLAC3D* simulation was re-run with the injection test excluded. This was done by simply setting the daily injection rates for the test period to zero (instead of the actual values used in the initial simulation).

The results from the new simulation indicate that the April-May 2020 injection test had negligible impact on the factor-of-safety in the area of the SW cluster. A horizontal section at a depth of 4.1 km from this new simulation is compared to the same section through the original simulation in Figure 5-5. These sections show the percent change in FoS from the day before the

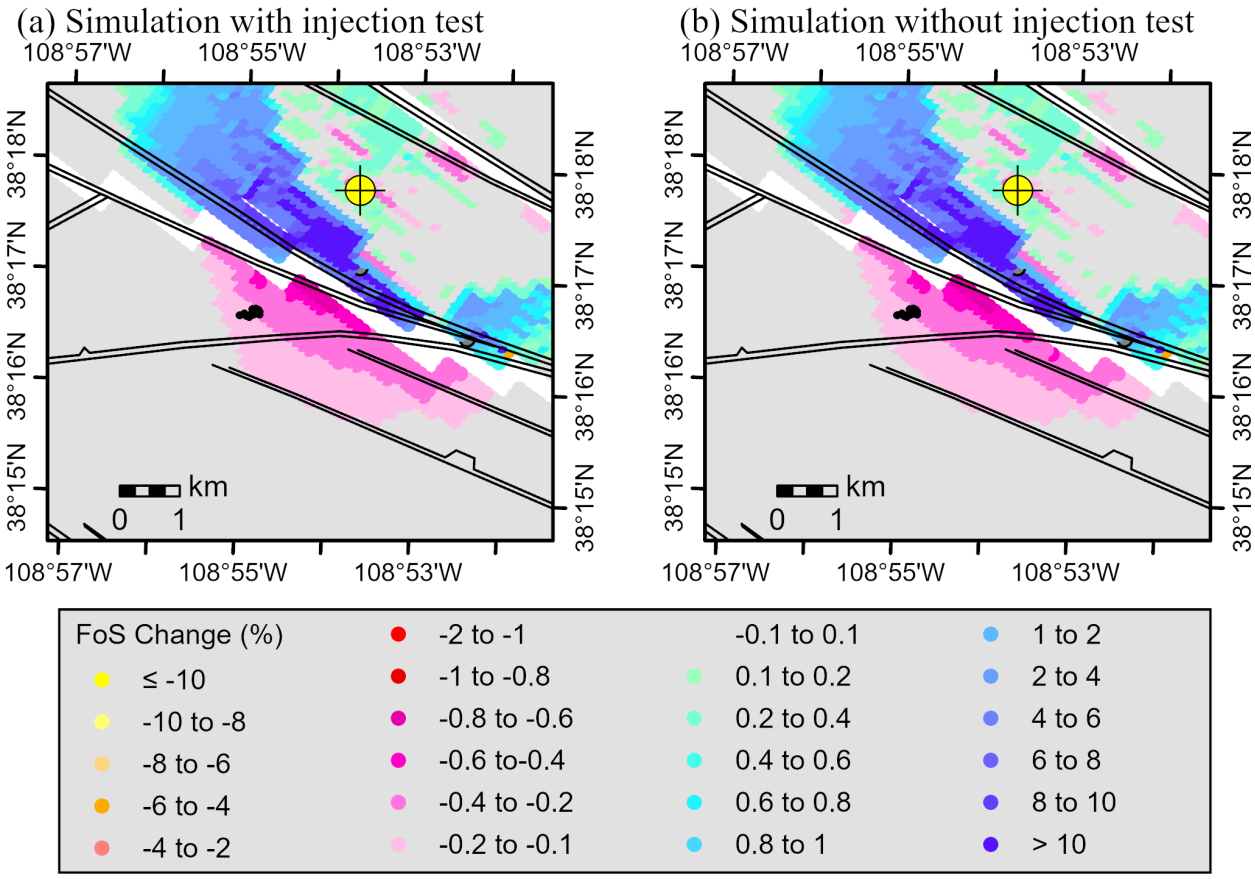

Figure 5-5: Horizontal sections at 4.1 km depth of the percent change in FoS from the day before the extended PVU injection well shut-in (3/3/2019) to the day prior to the start of the fall 2020 seismicity swarm (11/7/2020): (a) original simulation that includes the April-May 2020 injection test, and (b) new simulation that excludes the injection test. The black dots are a-quality earthquake hypocenters in the SW cluster through 11/7/2020. The black lines are faults at the top of the Precambrian basement interpreted from seismic reflection data (Arestad, 2016), and the thick white line is the impermeable fault in the *FLAC3D* model. The yellow circle with crosshairs is the PVU injection well.

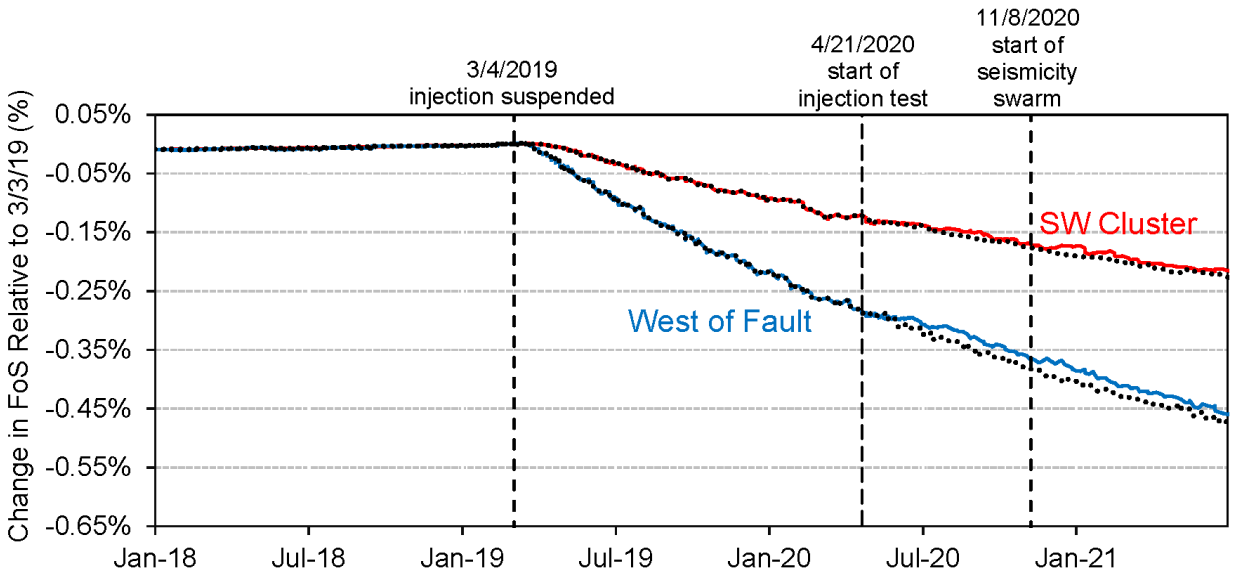

Figure 5-6: FoS histories at the two *FLAC3D* monitoring points southwest of the impermeable fault for simulations with (solid colored lines) and without (dotted black lines) the April-May 2020 injection test. The locations of the monitoring points are shown in Figure 5-4. The FoS histories are presented as percent changes in FoS over time relative to the value prior to the extended PVU injection well shut-in (3/3/2019). Small fluctuations in the curves may be due to noise in the numerical model (from discretization and/or incomplete convergence). Dates indicated by the vertical black dashed lines are: 3/4/2019 - PVU injection was suspended; 4/21/2020 – start of injection test; and 11/8/2020 - the fall 2020 seismicity swarm began.

injection well shut-in (3/3/2019) to the day prior to the start of the fall 2020 seismicity swarm (11/7/2020). The FoS patterns produced with and without the April-May 2020 injection test appear nearly identical (Figure 5-5). The FoS histories at the two monitoring points from the new simulation are compared to those from the original simulation in Figure 5-6. The differences between the FoS histories from the two simulations at monitoring point *SW Cluster* are negligible (Figure 5-6, the solid red line is from the simulation with the injection test and the underlying dotted black line is from the simulation without the test). At monitoring point *West of Fault*, the simulation without the injection test (dotted black line) shows a slightly larger decrease in FoS after mid-2020 than the simulation with the injection test (solid blue line). Hence, the injection test slowed the decrease in FoS at the *West of Fault* location by an extremely small amount (making seismicity slightly less likely). From these results, I conclude that the injection test did not contribute to the occurrence of the fall 2020 seismicity swarm.

5.3 Discussion

Results from geomechanical modeling indicate that stress changes related to the extended PVU injection well shut-in may have contributed to the occurrence of the fall 2020 seismicity swarm.

Factor-of-safety values decreased in the area of the SW cluster following the suspension of injection in early March 2019. These stress changes are likely related to depressurization of the reservoir and associated deformation of the surrounding formations. The changes in FoS indicated by the model are small, only a few tenths of a percent from March 2019 to the beginning of the seismicity swarm in November 2020. However, the changes occurred over a broad area simultaneously, which could have contributed to failure of large segments of the interpreted fault plane in the SW cluster. This pattern offers a potential explanation for the abnormally high portion of larger magnitude earthquakes (low b-value) in the SW cluster.

Seismicity in the SW cluster virtually stopped in mid-2022 (Figure 5-1b). (Only five earthquakes, all with magnitude $\leq M_D$ 0.0, were detected between July 2022 and December 2023.) This timing correlates with the resumption of PVU injection in June 2022. The geomechanical modeling results indicate that the FoS in the region of the SW cluster stabilized following resumption of PVU injection. According to the model, FoS has been increasing slightly just southwest of the impermeable fault since the resumption of injection and staying constant a little farther southwest (Figure 5-4). This pattern predicts a decrease in the potential for induced seismicity after mid-2022, which is consistent with the observed seismicity trend.

6.0 Conclusions

A new seismicity cluster (the SW cluster) began developing about 3 km southwest of the PVU injection well in late March 2019, a few weeks after an induced earthquake with magnitude M_W 4.5. The region where this cluster lies is interpreted as being outside the reservoir pressurized by PVU injection, on the far side of an impermeable fault that forms a barrier to pressure diffusion. Seismicity rates in the SW cluster greatly increased in November-December 2020. During this seismicity swarm, three earthquakes with magnitude $\geq M_W$ 3.5 occurred. Only four other earthquakes of this magnitude had been recorded in the Paradox Valley area since PVSN seismic monitoring began in 1985. The M_W 3.9 earthquake on December 20th 2020 is the fourth-largest local earthquake recorded by PVSN. Based on analyses of relative earthquake hypocenters and focal mechanisms, virtually all of the earthquakes in the SW cluster have occurred on a single fault striking N80°E and dipping 69° to 74° to the south. The rakes from the focal mechanisms indicate that the fault has primarily right-lateral strike-slip displacement. The fault geometry and sense of motion are similar to those of previous PVU-induced earthquakes (Ake et al., 2005; Block et al., 2020; Block et al., 2015; Yeck et al., 2014).

Based on analyses presented here, the initial earthquakes in the SW cluster are interpreted as aftershocks of the M_W 4.5 earthquake. Models of Coulomb stress transfer suggest that they occurred in response to stress changes caused by the fault rupture that produced the March 2019 M_W 4.5 earthquake. Seismicity rates in the SW cluster were low until November 2020, when both rates and maximum magnitudes of the earthquakes abruptly increased. The substantial increase in seismicity rate during the fall 2020 seismicity swarm is not consistent with normal aftershock activity predicted by the Omori aftershock rate relation.

During the extended shut-in of the PVU injection well that began on March 4th 2019 (in response to the M_W 4.5 induced earthquake), stresses continued to evolve in the region of the SW cluster. Geomechanical modeling indicates that these stress changes decreased the factor-of-safety, which is a measure of the potential for seismicity based on the Coulomb failure criterion. I interpret these stress changes as due to depressurization of the PVU reservoir during the extended injection well shut-in and associated deformation of surrounding formations. The magnitudes of the stress changes indicated by the model are small (only a few tenths of a percent from the beginning of the shut-in to the beginning of the seismicity swarm in November 2020) but occurred over a broad area. This decrease in FoS may have contributed to the increased seismicity rates, and possibly the increased earthquake magnitudes, during the fall 2020 seismicity swarm.

The geomechanical modeling indicates that the April-May 2020 injection test had a negligible impact on the factor-of-safety values in the region of the SW cluster. From these results, I conclude that the injection test did not contribute to the occurrence of the fall 2020 seismicity swarm.

Seismicity rates in the SW cluster decreased in early January 2021. Several SW-cluster earthquakes with magnitude ≥ M_W 3.0 that occurred during the fall 2020 seismicity swarm transferred some Coulomb stress away from the interpreted fault plane, which may have contributed to the end of the swarm activity. Seismicity continued to occur at lower rates and magnitudes until June 2022, when seismicity in the SW cluster virtually stopped. This timing correlates with the resumption of PVU injection. Geomechanical modeling indicates that the stress changes associated with reservoir depressurization in the region of the SW cluster stabilized following resumption of PVU injection, decreasing the potential for seismicity. Hence, the resumption of PVU injection in June 2022 appears to have contributed to the decrease in seismicity in the SW cluster.

Since the SW cluster produced four of the seven PVU-induced earthquakes with $M_W \geq 3.5$ recorded to date, understanding the mechanisms that trigger seismicity in that cluster is essential for trying to reduce the seismic hazard associated with PVU operations. *FLAC3D* geomechanical modeling and Coulomb stress analyses of large induced earthquakes yield insights into the mechanisms controlling the seismicity in this cluster. These tools are especially useful in this area because the seismicity in the region of the SW cluster is not controlled by pore pressure increase from PVU injection, because it lies outside the pressurized reservoir. Hence, updated stress analyses, such as those used during this study, should be considered when making decisions about future PVU operations.

7.0 References

Ake, J., Mahrer, K., O'Connell, D., and Block, L., 2005, Deep-injection and closely monitored induced seismicity at Paradox Valley, Colorado: *Bulletin of the Seismological Society of America*, v. 95, no. 2, p. 664-683.

Allis, R. G., Morgan, C. D., Heuscher, S., and McDonald, A., 2009, Regional Middle Paleozoic Hydrodynamic Pressure Regime of the Paradox Basin, Utah and Colorado, *in* Thomas C. Chidsey, J., ed., The Mississippian Leadville Limestone Exploration Play, Utah and Colorado - Exploration Techniques and Studies for Independents: Salt Lake City, Utah Geological Survey, 20 pp.

Arestad, J. F., 2016, *Paradox Valley Unit Seismic Data Interpretation Phase 2 Report*, Excel Geophysical Services and International Reservoir Technologies, Inc., 62 pp.

Block, L., Besana-Ostman, G., and Wood, C., 2020, *Analysis of the March 4, 2019 Earthquake and Its Aftershocks*: Technical Memorandum No. 86-68330-2020-07, Bureau of Reclamation, Denver, Colorado, 149 pp.

Block, L., and Kang, J. B., 2024, *Geomechanical and Flow Modeling of the 2022 Injection Test and Future Injection Scenarios, Paradox Valley Unit, Colorado*: Technical Memorandum No. 86-68330-2023-2, Bureau of Reclamation, Denver, Colorado, 75 pp.

Block, L., Wood, C. K., Schwarzer, J., Kang, J. B., Besana-Ostman, G., and Ball, J., 2024, *2023 Annual Report, Paradox Valley Seismic Network, Paradox Valley Unit, Colorado*: Technical Memorandum No. 86-68330-2024-3, Bureau of Reclamation, Denver, Colorado, 88 pp.

Block, L., 2024a, *Development of a New Velocity Model for the Paradox Valley Area, Paradox Valley Unit, Colorado*: Technical Memorandum No. 86-68330-2024-7, Bureau of Reclamation, Denver, Colorado, 122 pp.

Block, L., 2024b, *Event Relative Location and Updated Earthquake Catalog, Paradox Valley Seismic Network, Paradox Valley Unit, Colorado*: Technical Memorandum No. 86-68330-2024-10, Bureau of Reclamation, Denver, Colorado, 19 pp.

Block, L. V., Wood, C. K., Yeck, W. L., and King, V. M., 2014, The 24 January 2013 ML 4.4 Earthquake near Paradox, Colorado, and Its Relation to Deep Well Injection: *Seismological Research Letters*, v. 85, no. 3, p. 609-624.

Block, L. V., Wood, C. K., Yeck, W. L., and King, V. M., 2015, Induced seismicity constraints on subsurface geological structure, Paradox Valley, Colorado: *Geophysical Jounal International*, v. 200, p. 1172-1195.

Bremkamp, W., and Harr, C. L., 1988, *Area of Least Resistance to Fluid Movement and Pressure Rise, Paradox Valley Unit Salt Brine Injection Project, Bedrock, Colorado*, 39 pp.

Brune, J. N., 1970, Tectonic Stress and the Spectra of Seismic Shear Waves from Earthquakes: *Journal of Geophysical Research*, v. 75, no. 26, p. 4997-5009.

Brune, J. N., 1971, Correction [to "Tectonic stress and the spectra, of seismic shear waves from earthquakes"]: *Journal of Geophysical Research*, v. 76, no. 20, p. 5002-5002.

Detournay, C., 2018, *Geomechanical and Flow Modeling Follow-on: Summary Report*, Itasca Consulting Group, Inc., Minneapolis, MN, 308 pp.

Detournay, C., and Dzik, E., 2017, *Geomechanical and Flow Modeling for Paradox Valley Unit, Study for USBR: Summary Report*, Itasca Consulting Group, Inc., Minneapolis, MN, 337 pp.

Dewan, J. T., 1988, Re: BOR Paradox Valley Injection Test Well #1. Interpretation of Logs Run in Liner Hole., Dewan & Timco, Inc., Houston, 32 pp.

Gibbs, J. F., Healy, J. H., Raleigh, C. B., and Coakley, J., 1973, Seismicity in the Rangely, Colorado, Area: 1962-1970: *Bulletin of the Seismological Society of America*, v. 63, no. 5, p. 1557-1570.

Gutenberg, B., and Richter, C. F., 1954, Seismicity of the Earth and Associated Phenomena, Princeton, New Jersey, Princeton University Press, 310 pp.

Herman, M., 2022, Hdef (Half-space Deformation Toolbox): Department of Geological Sciences, California State University, Bakersfield, CA; URL https://www.matthewwherman.com/software.html; DOI https://doi.org/10.5281/zenodo.3894137; code downloaded Feb. 2022.

Hsieh, P. A., and Bredehoeft, J. D., 1981, A reservoir analysis of the Denver earthquakes; a case of induced seismicity: *Journal of Geophysical Research. B*, v. 86, no. 2, p. 903-920.

Itasca Consulting Group, I., 2018, FLAC3D 7.0 - Fast Lagrangian Analysis of Continua in Three Dimensions, ver. 7.0: Minneapolis, Minnesota.

King, V. M., Wood, C. K., and Block, L. V., 2018, *Integrated Subsurface Geologic Model, Paradox Valley, Colorado*: Technical Memorandum 85-833000-2017-15, Bureau of Reclamation, 92 pp.

Nicholson, C., and Wesson, R. L., 1990, *Earthquake Hazard Associated With Deep Well Injection - A Report to the U.S. Environmental Protection Agency:* Bulletin 1951, U.S. Geological Survey, 86 pp.

Raleigh, C. B., Healy, J. H., and Bredehoeft, J. D., 1976, An Experiment in Earthquake Control at Rangely, Colorado: *Science*, v. 191, no. 4233, p. 1230-1237.

Roylance, D., 2001, Transformation of Stresses and Strains, Modules in Mechanics and Materials online textbook, Department of Materials Science and Engineering, Massachusetts Institute of Technolody, Cambridge, MA; https://web.mit.edu/course/3/3.11/www/modules/trans.pdf, p. 1-15.

Snoke, J. A., 2009, *FOCMEC: FOCal MEChanisn Determinations*, Virginia Tech, Blacksburg, VA, 22 pp.

Wood, C. K., Block, L. V., King, V. M., and Yeck, W. L., 2016, *The ML 4.4 Earthquake of January 24, 2013, Near Paradox, Colorado, and Implications for Near-term Injection Operations:* Technical Memorandum 86-68330-2013-12, Bureau of Reclamation, 151 pp.

Yeck, W. L., Block, L. V., Wood, C. K., and King, V. M., 2014, Maximum magnitude estimations of induced earthquakes at Paradox Valley, Colorado, from cumulative injection volume and geometry of seismicity clusters: *Geophysical Journal International*, v. 200, no. 1, p. 322-336.

Appendix A

Additional Hypocenter Maps and Vertical Sections

Time-lapse maps and vertical sections of hypocenters in the SW cluster and in the area of the March 2019 M_W 4.5 earthquake fault plane are included in this appendix. Only a-quality (relative) hypocenters are included. Each plot includes earthquakes from the date range indicated on the plot. These ranges extend from March 2019 through April 2022.

On the maps, the epicenters of the earthquakes that have occurred since (and including) the M_W 4.5 earthquake are color-coded by hypocenter depth. Earthquakes with magnitude $\geq M_D$ 2.5 are plotted with larger symbols. The small gray dots are earthquakes that pre-date the M_W 4.5 earthquake. The black dashed rectangle is the rough extent of the M_W 4.5 fault plane. The dashed red rectangle is the rough extent of the interpreted fault plane in the SW cluster. The yellow star is the location of the PVU injection well.

On the vertical plots, two projections are included. The projection on the left is perpendicular to the strike of the fault plane in the SW cluster. (It includes events within a 1.75-km-long region parallel to the strike of the fault plane.) The projection on the right is parallel to the strike of the M_W 4.5 fault plane. (It includes events within a 1.2-km-long region parallel to the dip of the plane.) Only events that have occurred since (and including) the M_W 4.5 earthquake are shown. Earthquake symbols are sized and color-coded by earthquake magnitude, as indicated in the legends. The geologic interfaces and location of the impermeable barrier fault are from Block et al. (2020). The dashed red line and circle represent the approximate dip and extent of the fault plane in the SW cluster, respectively.

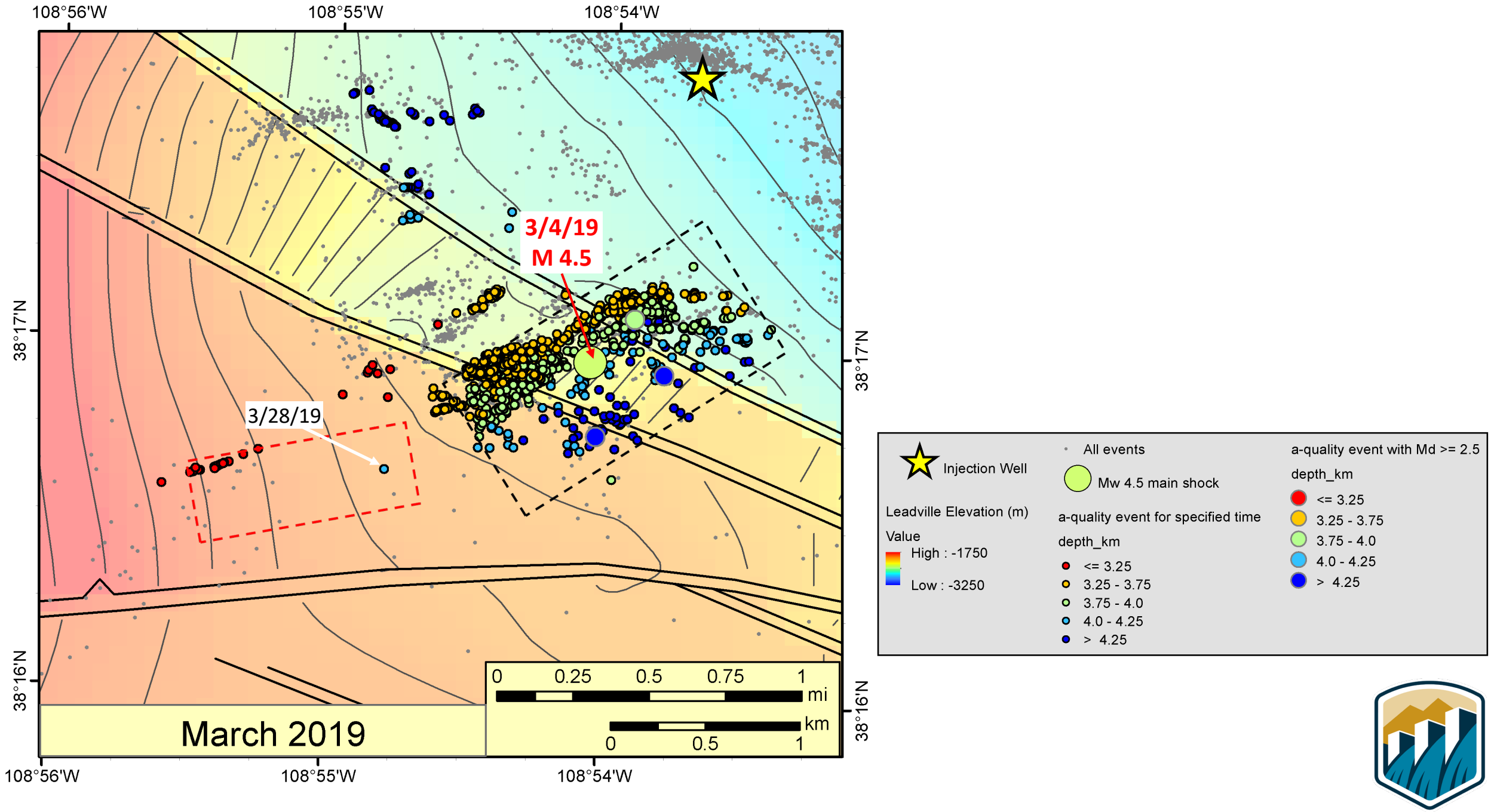
108°56'W
108°55'W
108°54'W
38°17'N
38°16'N
3/4/19
M 4.5
3/28/19
March 2019
0 0.25 0.5 0.75 1 mi
0 0.5 1 km
Injection Well
Mw 4.5 main shock
Leadville Elevation (m)
Value
High : -1750
Low : -3250
All events
a-quality event for specified time
depth_km
<= 3.25
3.25 - 3.75
3.75 - 4.0
4.0 - 4.25
> 4.25
a-quality event with Md >= 2.5
depth_km
<= 3.25
3.25 - 3.75
3.75 - 4.0
4.0 - 4.25
> 4.25

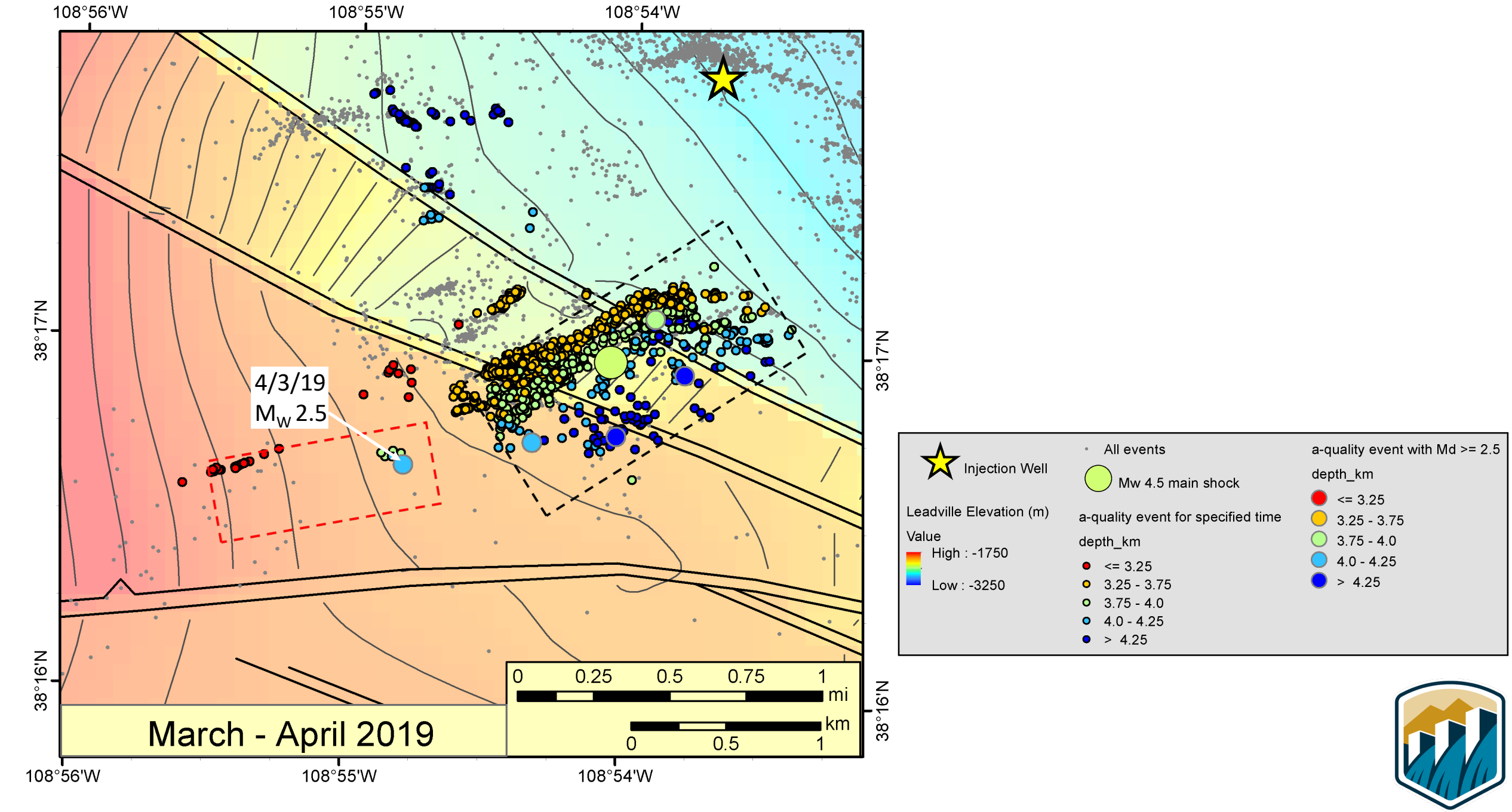
108°56'W
108°55'W
108°54'W
38°17'N
38°16'N
4/3/19
M_W 2.5
March - April 2019
0 0.25 0.5 0.75 1 mi
0 0.5 1 km
Injection Well
Mw 4.5 main shock
Leadville Elevation (m)
Value
High : -1750
Low : -3250
All events
a-quality event for specified time
depth_km
<= 3.25
3.25 - 3.75
3.75 - 4.0
4.0 - 4.25
> 4.25
a-quality event with Md >= 2.5
depth_km
<= 3.25
3.25 - 3.75
3.75 - 4.0
4.0 - 4.25
> 4.25

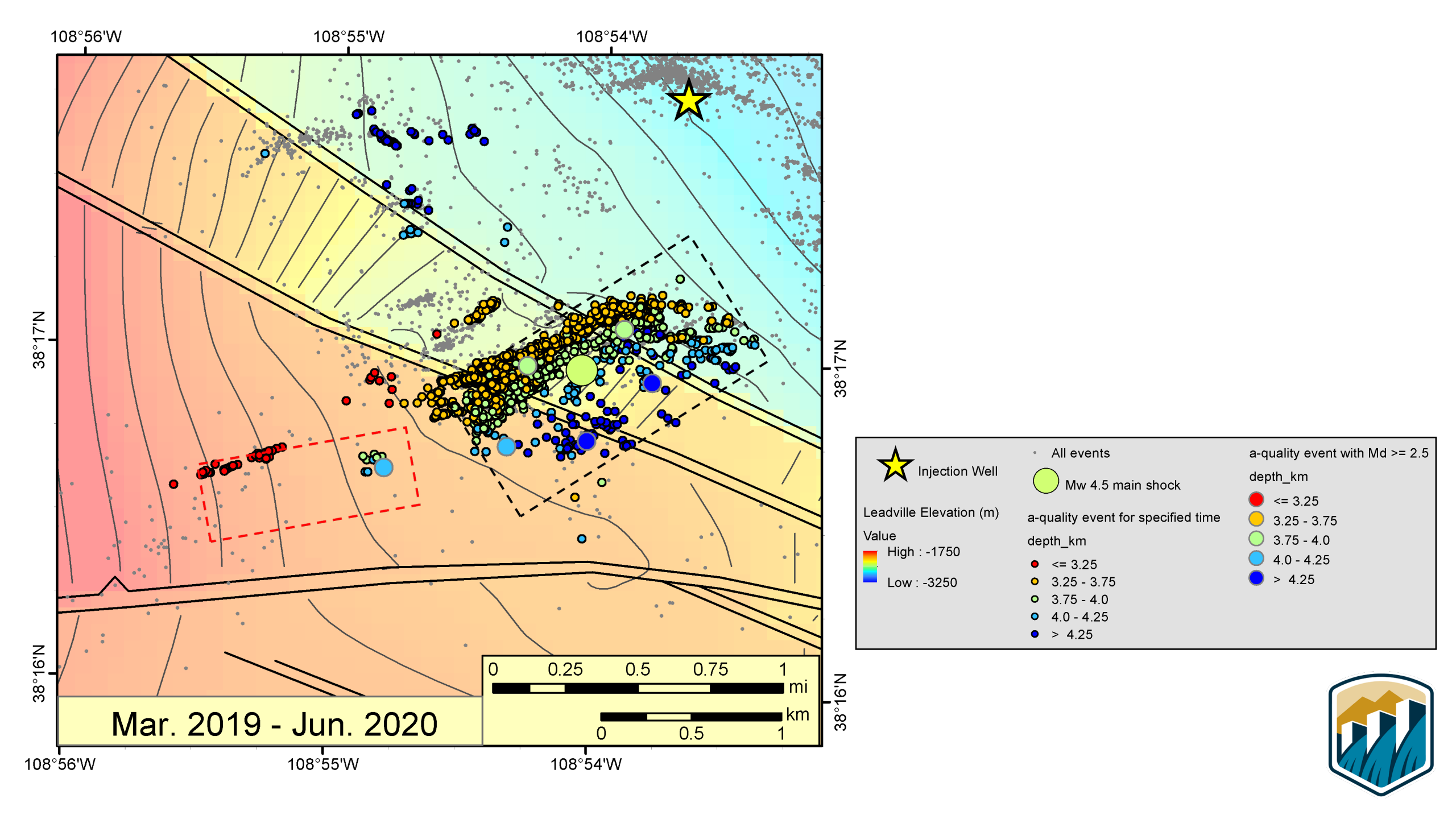
108°56'W
108°55'W
108°54'W
38°17'N
38°16'N
Mar. 2019 - Jun. 2020
0 0.25 0.5 0.75 1 mi
0 0.5 1 km
Injection Well
Leadville Elevation (m)
Value
High : -1750
Low : -3250
All events
Mw 4.5 main shock
a-quality event for specified time
depth_km
<= 3.25
3.25 - 3.75
3.75 - 4.0
4.0 - 4.25
> 4.25
a-quality event with Md >= 2.5
depth_km
<= 3.25
3.25 - 3.75
3.75 - 4.0
4.0 - 4.25
> 4.25

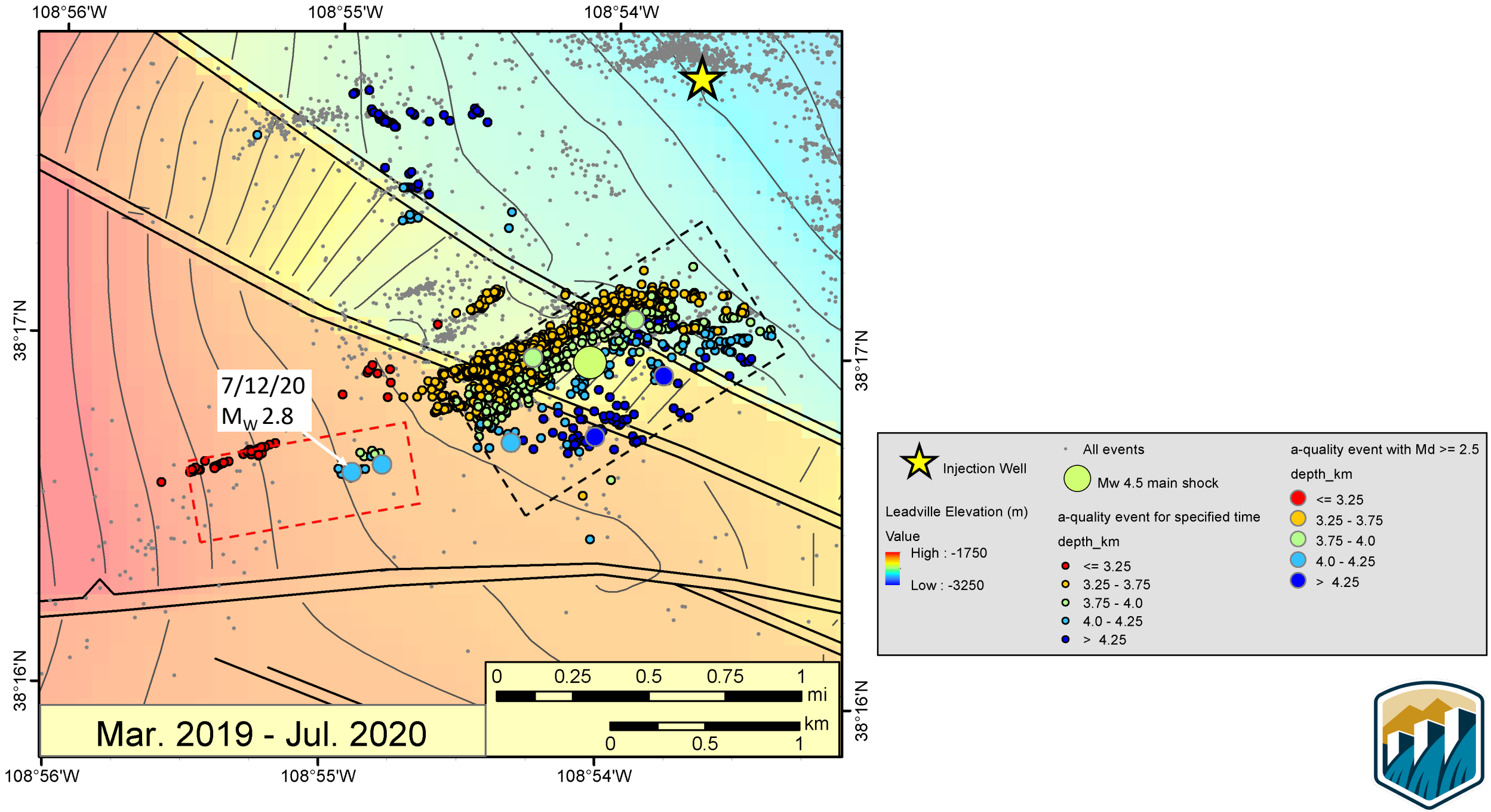
108°56'W
108°55'W
108°54'W
38°17'N
38°16'N
7/12/20
M_W 2.8
Mar. 2019 - Jul. 2020
0 0.25 0.5 0.75 1 mi
0 0.5 1 km
Injection Well
All events
Mw 4.5 main shock
Leadville Elevation (m)
Value
High : -1750
Low : -3250
a-quality event for specified time
depth_km
<= 3.25
3.25 - 3.75
3.75 - 4.0
4.0 - 4.25
> 4.25
a-quality event with Md >= 2.5
depth_km
<= 3.25
3.25 - 3.75
3.75 - 4.0
4.0 - 4.25
> 4.25

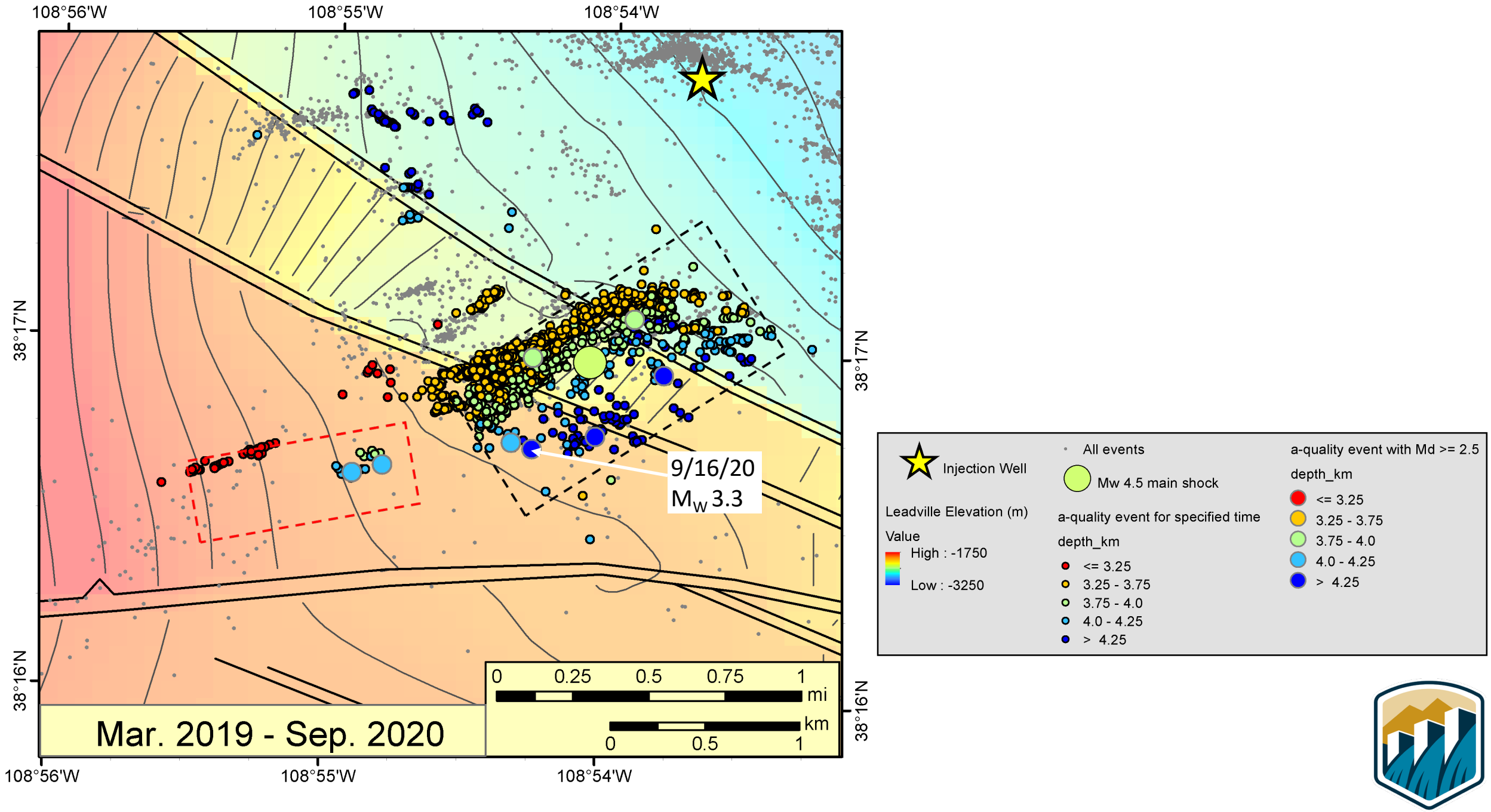
108°56'W
108°55'W
108°54'W
38°17'N
38°16'N
9/16/20
M_W 3.3
Mar. 2019 - Sep. 2020
0 0.25 0.5 0.75 1 mi
0 0.5 1 km
Injection Well
Leadville Elevation (m)
Value
High : -1750
Low : -3250
All events
Mw 4.5 main shock
a-quality event for specified time
depth_km
<= 3.25
3.25 - 3.75
3.75 - 4.0
4.0 - 4.25
> 4.25
a-quality event with Md >= 2.5
depth_km
<= 3.25
3.25 - 3.75
3.75 - 4.0
4.0 - 4.25
> 4.25

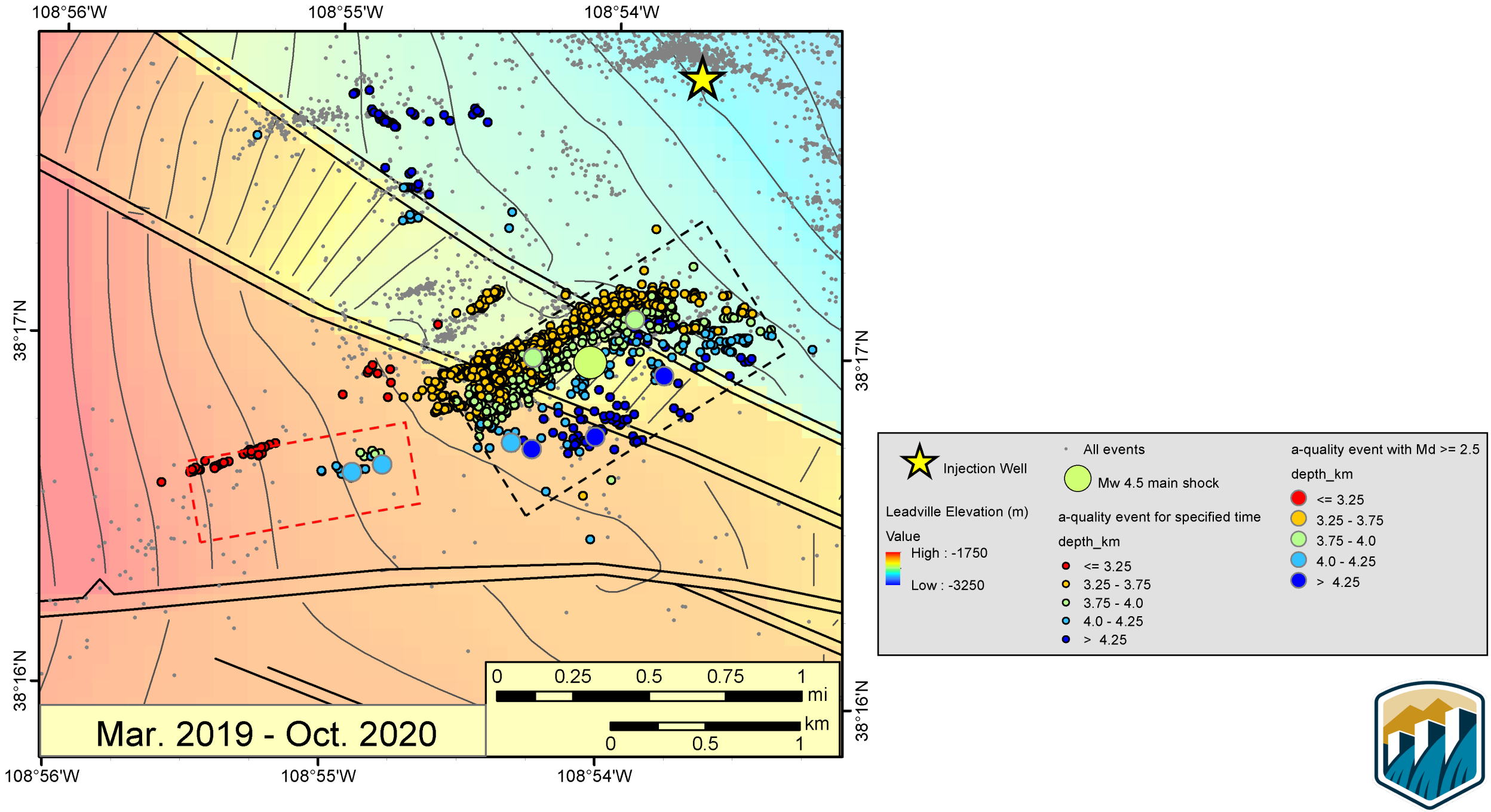
108°56'W
108°55'W
108°54'W
38°17'N
38°16'N
Mar. 2019 - Oct. 2020
0 0.25 0.5 0.75 1 mi
0 0.5 1 km
Injection Well
All events
Mw 4.5 main shock
Leadville Elevation (m)
Value
High : -1750
Low : -3250
a-quality event for specified time
depth_km
<= 3.25
3.25 - 3.75
3.75 - 4.0
4.0 - 4.25
> 4.25
a-quality event with Md >= 2.5
depth_km
<= 3.25
3.25 - 3.75
3.75 - 4.0
4.0 - 4.25
> 4.25

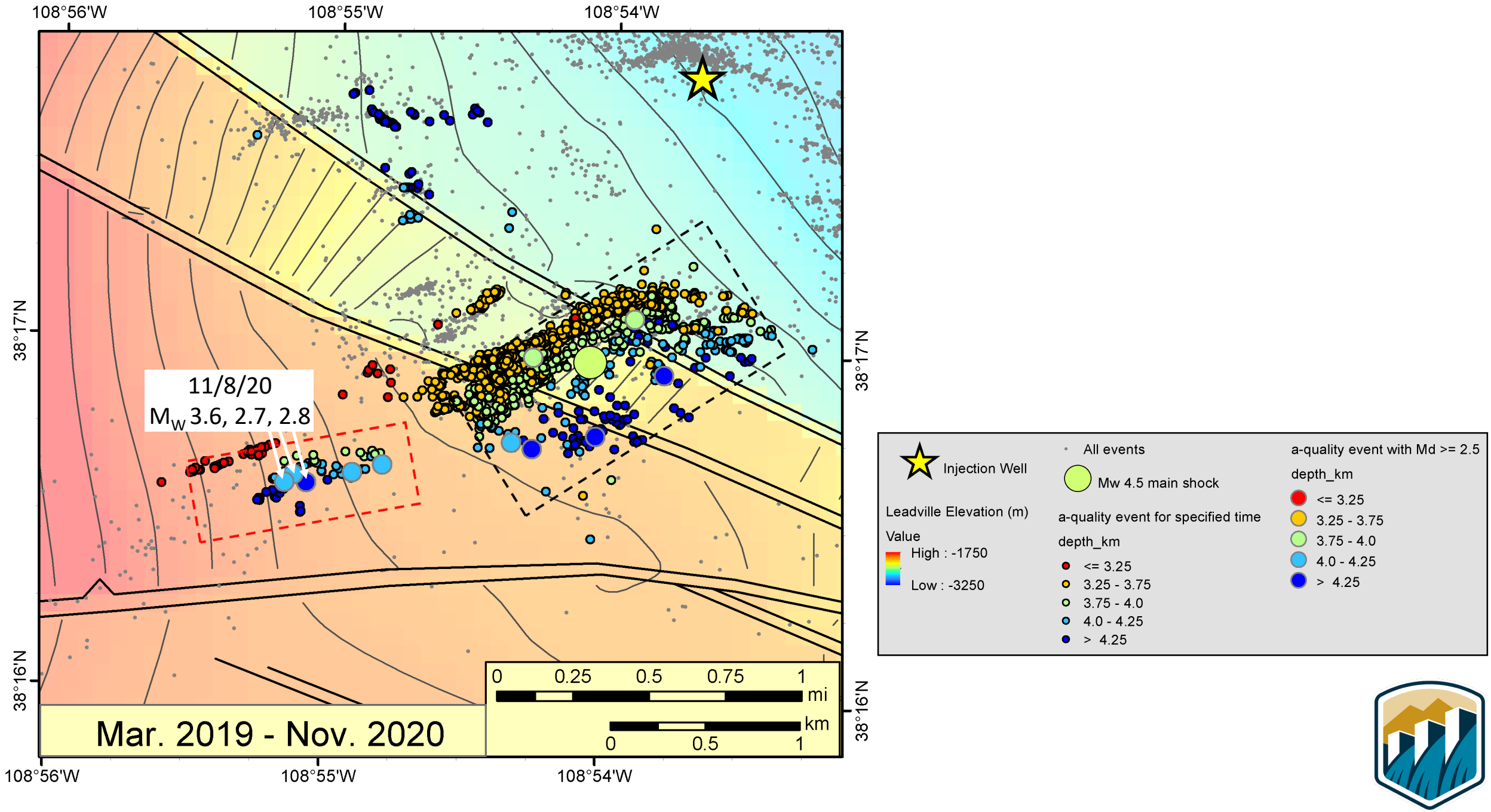
108°56'W
108°55'W
108°54'W
38°17'N
38°16'N
11/8/20
M_W 3.6, 2.7, 2.8
Mar. 2019 - Nov. 2020
0 0.25 0.5 0.75 1 mi
0 0.5 1 km
Injection Well
Leadville Elevation (m)
Value
High : -1750
Low : -3250
All events
Mw 4.5 main shock
a-quality event for specified time
depth_km
<= 3.25
3.25 - 3.75
3.75 - 4.0
4.0 - 4.25
> 4.25
a-quality event with Md >= 2.5
depth_km
<= 3.25
3.25 - 3.75
3.75 - 4.0
4.0 - 4.25
> 4.25

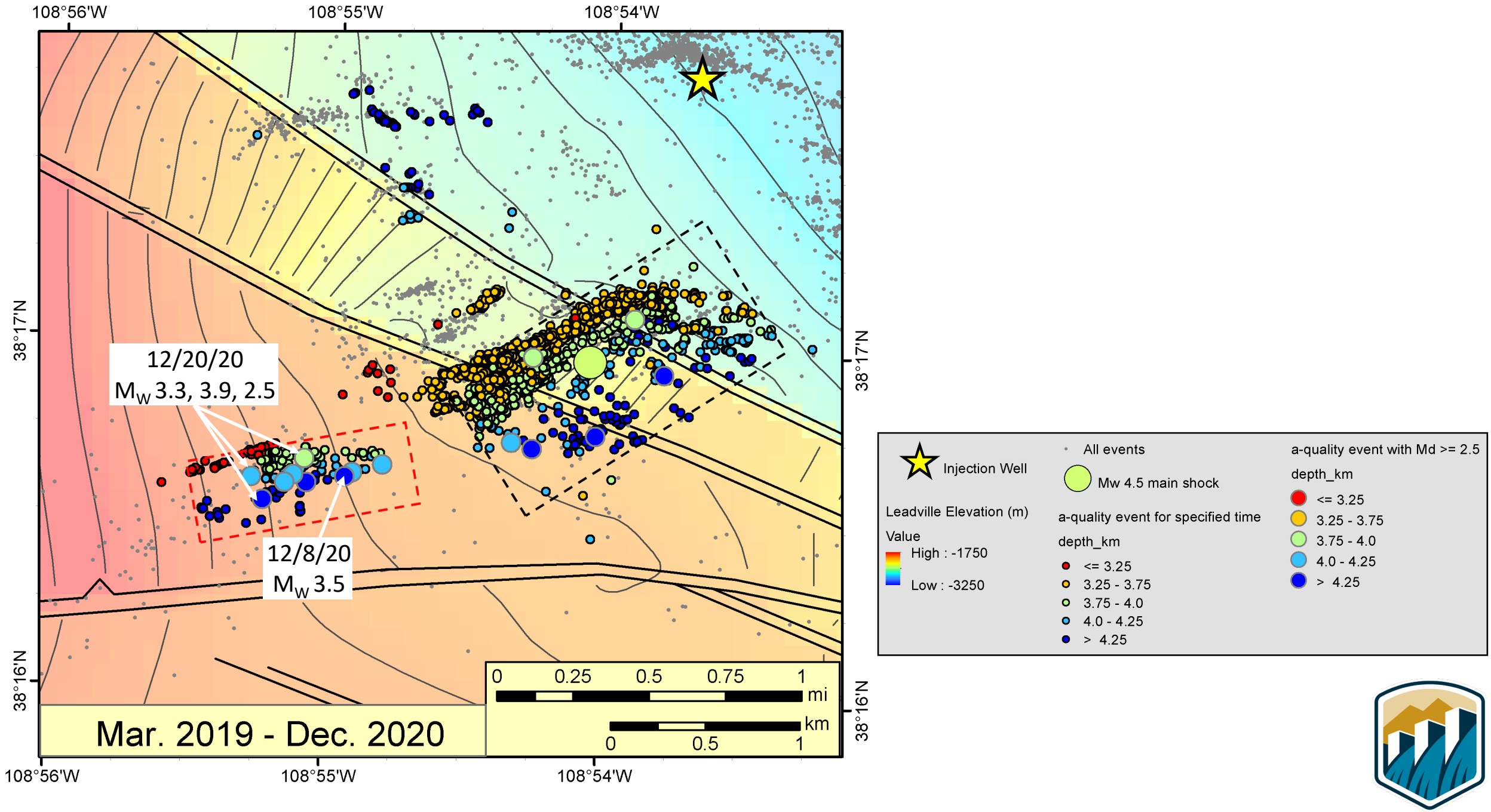
108°56'W
108°55'W
108°54'W
38°17'N
38°16'N
12/20/20
M_W 3.3, 3.9, 2.5
12/8/20
M_W 3.5
Mar. 2019 - Dec. 2020
0 0.25 0.5 0.75 1 mi
0 0.5 1 km
Injection Well
Leadville Elevation (m)
Value
High : -1750
Low : -3250
All events
Mw 4.5 main shock
a-quality event for specified time
depth_km
<= 3.25
3.25 - 3.75
3.75 - 4.0
4.0 - 4.25
> 4.25
a-quality event with Md >= 2.5
depth_km
<= 3.25
3.25 - 3.75
3.75 - 4.0
4.0 - 4.25
> 4.25

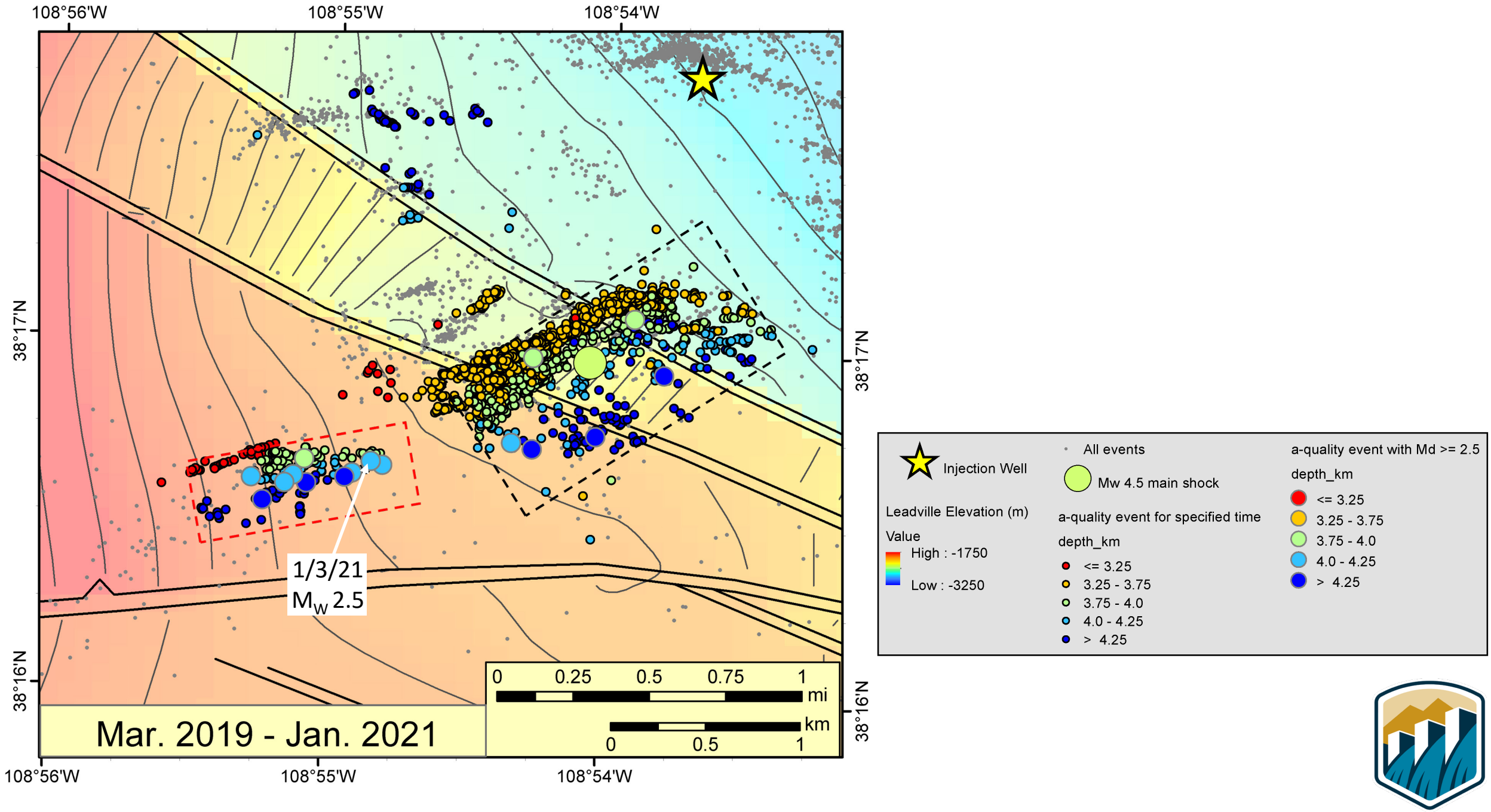
108°56'W
108°55'W
108°54'W
38°17'N
38°16'N
1/3/21
M_W 2.5
Mar. 2019 - Jan. 2021
0 0.25 0.5 0.75 1 mi
0 0.5 1 km
Injection Well
Mw 4.5 main shock
Leadville Elevation (m)
Value
High : -1750
Low : -3250
All events
a-quality event for specified time
depth_km
<= 3.25
3.25 - 3.75
3.75 - 4.0
4.0 - 4.25
> 4.25
a-quality event with Md >= 2.5
depth_km
<= 3.25
3.25 - 3.75
3.75 - 4.0
4.0 - 4.25
> 4.25

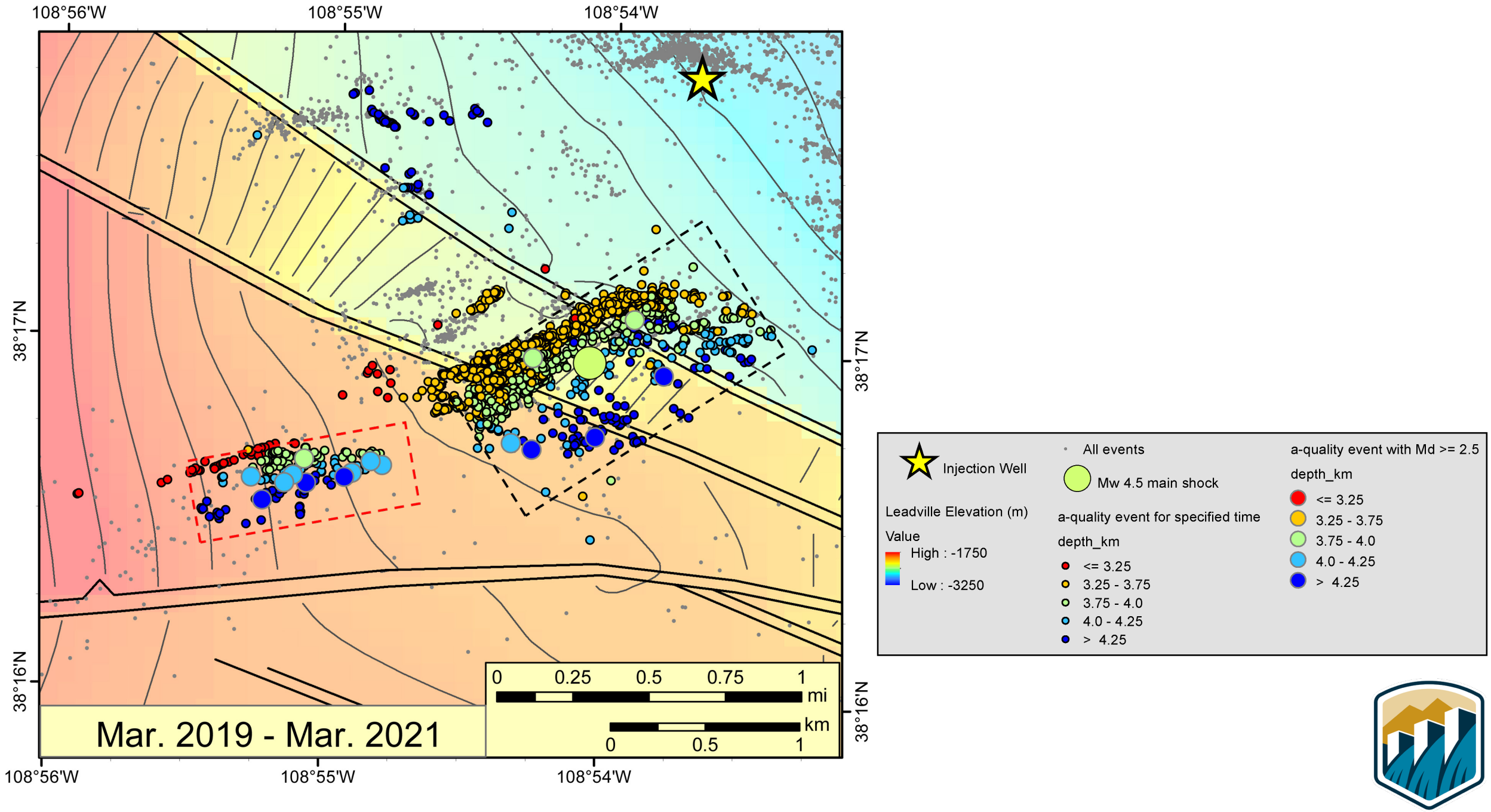
108°56'W
108°55'W
108°54'W
38°17'N
38°16'N
Mar. 2019 - Mar. 2021
0 0.25 0.5 0.75 1 mi
0 0.5 1 km
Injection Well
Mw 4.5 main shock
Leadville Elevation (m)
Value
High : -1750
Low : -3250
All events
a-quality event for specified time
depth_km
<= 3.25
3.25 - 3.75
3.75 - 4.0
4.0 - 4.25
> 4.25
a-quality event with Md >= 2.5
depth_km
<= 3.25
3.25 - 3.75
3.75 - 4.0
4.0 - 4.25
> 4.25

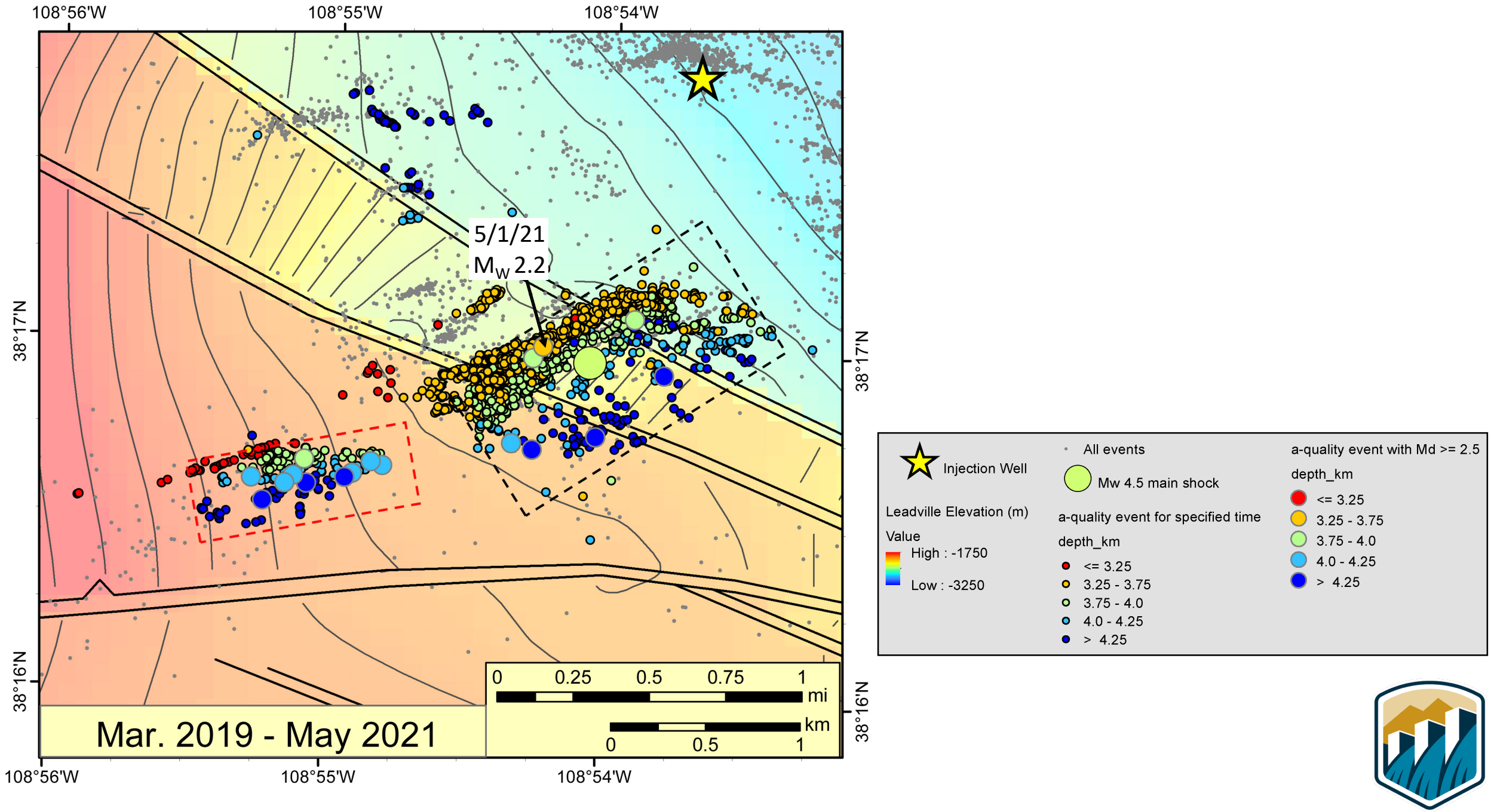
108°56'W
108°55'W
108°54'W
38°17'N
38°16'N
5/1/21
M_W 2.2
Mar. 2019 - May 2021
0 0.25 0.5 0.75 1 mi
0 0.5 1 km
Injection Well
Mw 4.5 main shock
Leadville Elevation (m)
Value
High : -1750
Low : -3250
All events
a-quality event for specified time
depth_km
<= 3.25
3.25 - 3.75
3.75 - 4.0
4.0 - 4.25
> 4.25
a-quality event with Md >= 2.5
depth_km
<= 3.25
3.25 - 3.75
3.75 - 4.0
4.0 - 4.25
> 4.25

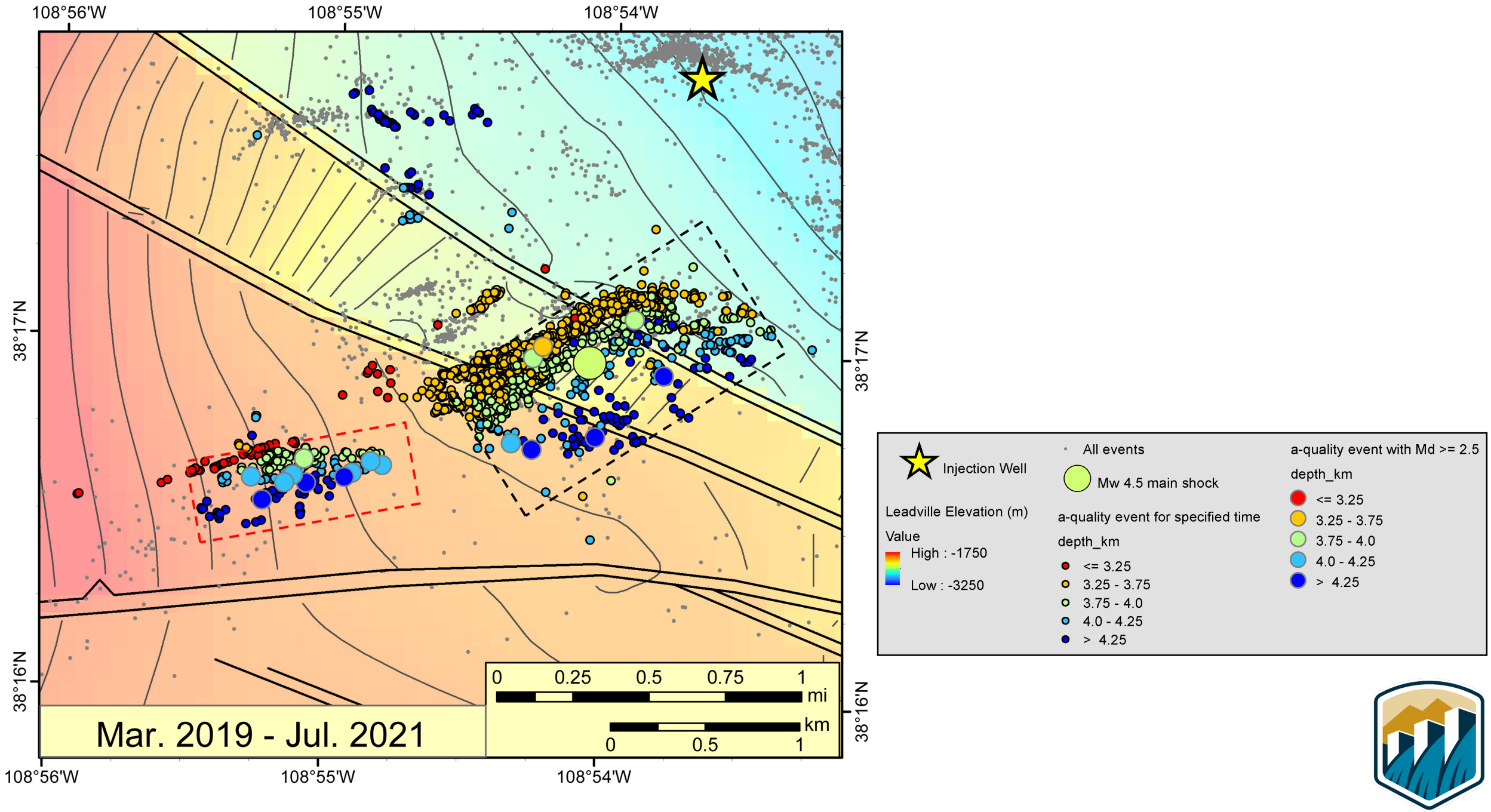
108°56'W
108°55'W
108°54'W
38°17'N
38°16'N
Mar. 2019 - Jul. 2021
0 0.25 0.5 0.75 1 mi
0 0.5 1 km
Injection Well
Mw 4.5 main shock
Leadville Elevation (m)
Value
High : -1750
Low : -3250
All events
a-quality event for specified time
depth_km
<= 3.25
3.25 - 3.75
3.75 - 4.0
4.0 - 4.25
> 4.25
a-quality event with Md >= 2.5
depth_km
<= 3.25
3.25 - 3.75
3.75 - 4.0
4.0 - 4.25
> 4.25

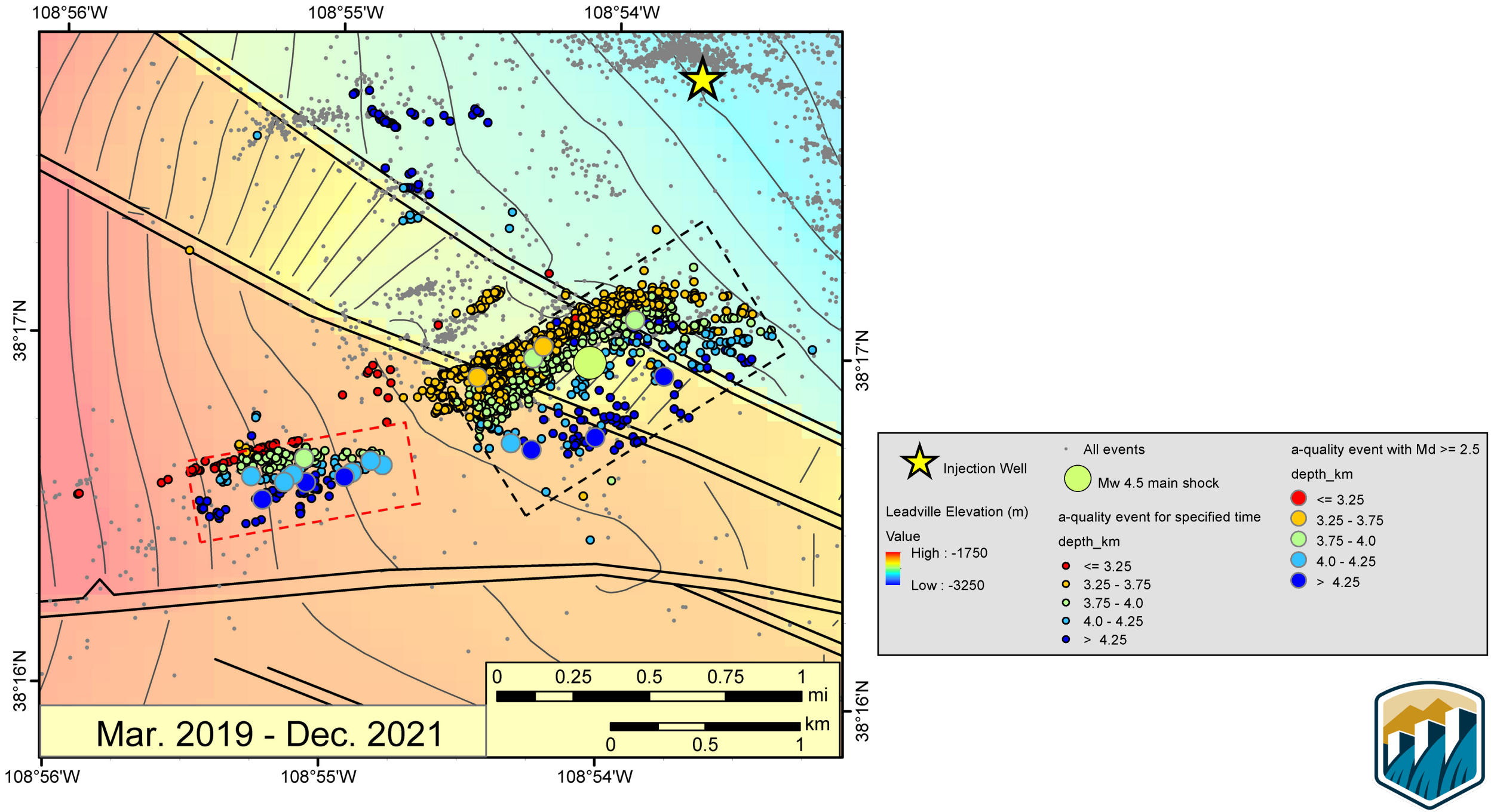
108°56'W
108°55'W
108°54'W
38°17'N
38°16'N
Mar. 2019 - Dec. 2021
0 0.25 0.5 0.75 1 mi
0 0.5 1 km
Injection Well
Mw 4.5 main shock
Leadville Elevation (m)
Value
High : -1750
Low : -3250
All events
a-quality event for specified time
depth_km
<= 3.25
3.25 - 3.75
3.75 - 4.0
4.0 - 4.25
> 4.25
a-quality event with Md >= 2.5
depth_km
<= 3.25
3.25 - 3.75
3.75 - 4.0
4.0 - 4.25
> 4.25

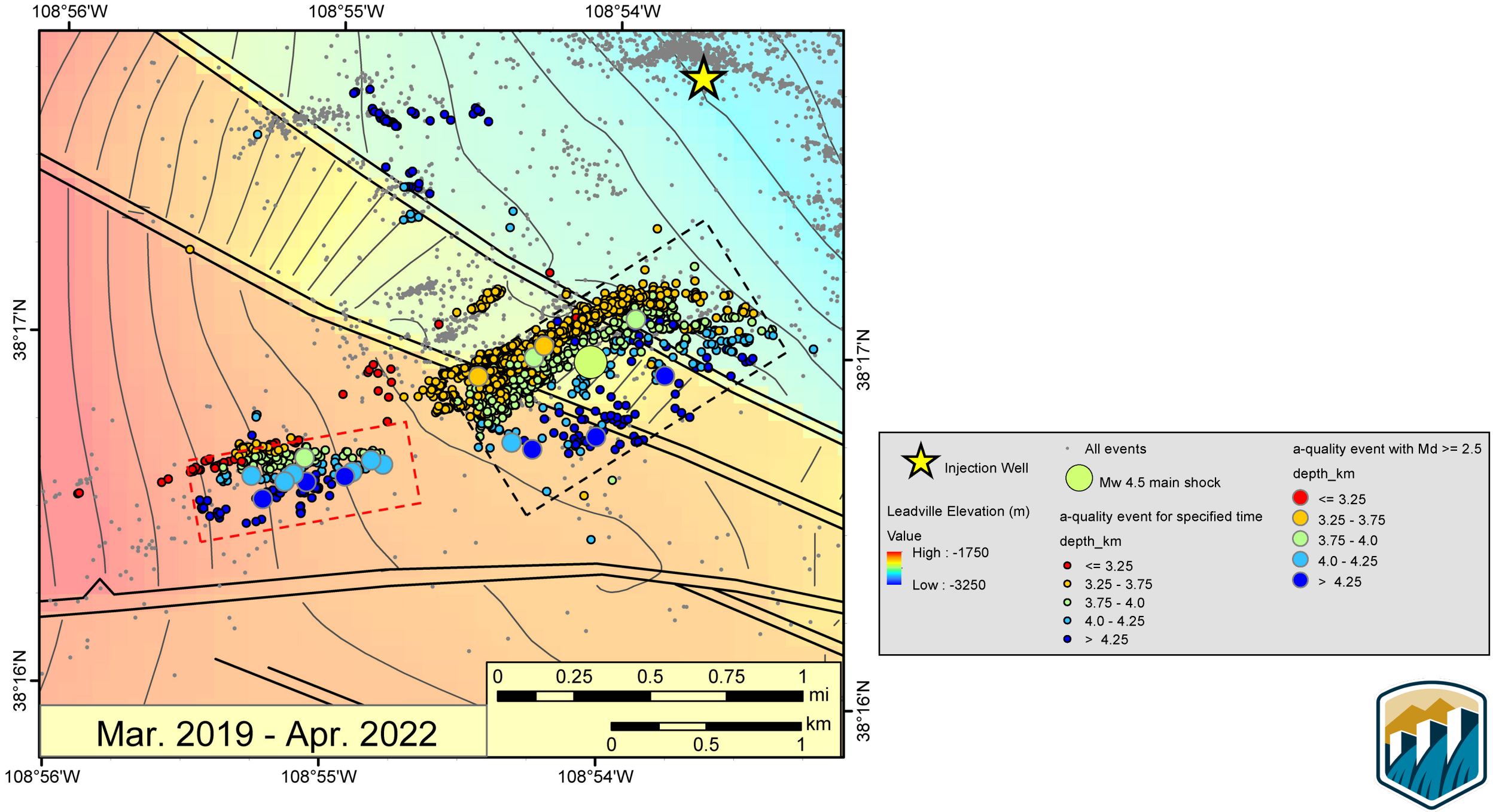
108°56'W
108°55'W
108°54'W
38°17'N
38°16'N
Mar. 2019 - Apr. 2022
0 0.25 0.5 0.75 1 mi
0 0.5 1 km
Injection Well
Leadville Elevation (m)
Value
High : -1750
Low : -3250
All events
Mw 4.5 main shock
a-quality event for specified time
depth_km
<= 3.25
3.25 - 3.75
3.75 - 4.0
4.0 - 4.25
> 4.25
a-quality event with Md >= 2.5
depth_km
<= 3.25
3.25 - 3.75
3.75 - 4.0
4.0 - 4.25
> 4.25

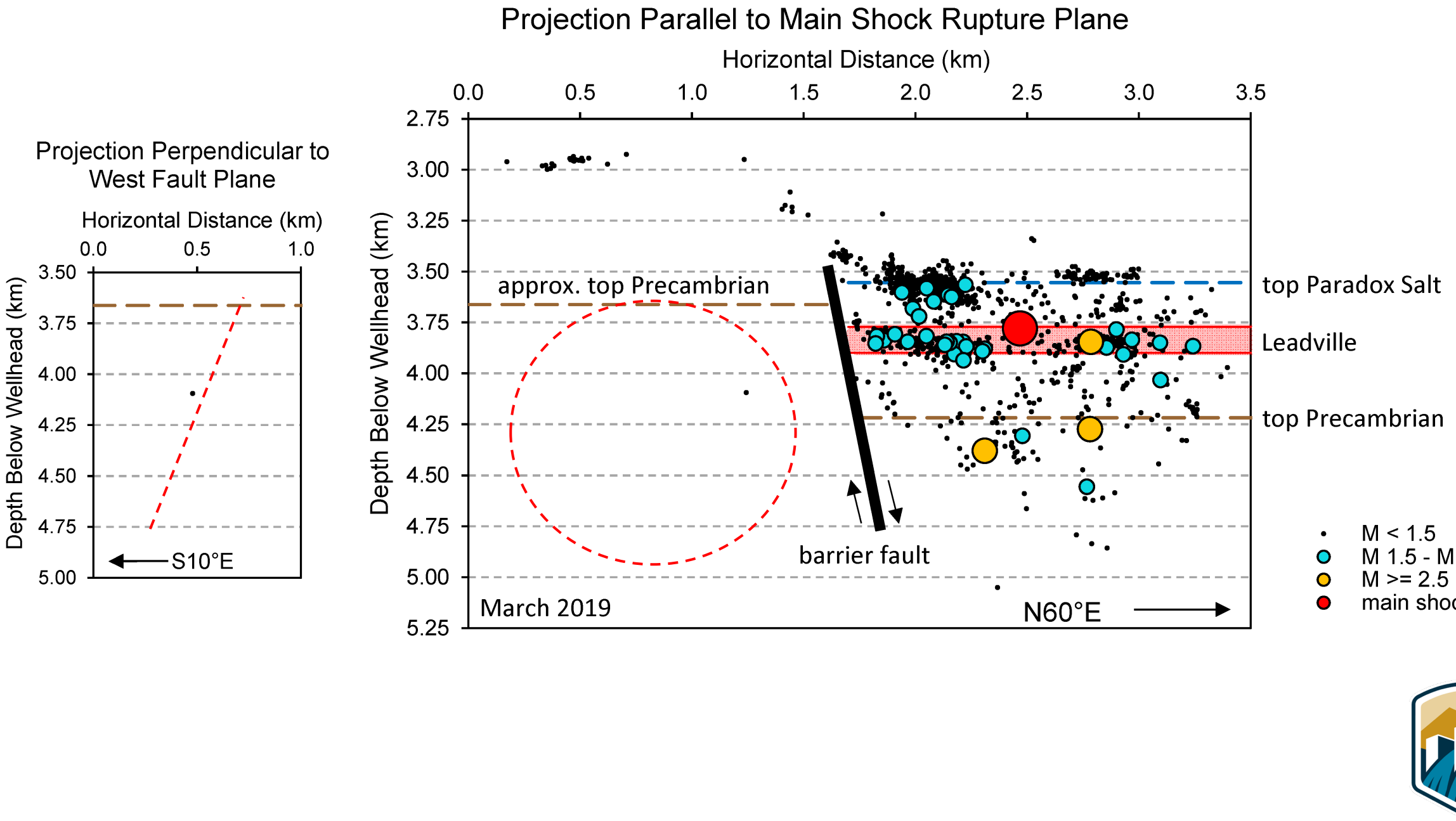
Projection Parallel to Main Shock Rupture Plane
Horizontal Distance (km)
0.0
0.5
1.0
1.5
2.0
2.5
3.0
3.5
Depth Below Wellhead (km)
2.75
3.00
3.25
3.50
3.75
4.00
4.25
4.50
4.75
5.00
5.25
approx. top Precambrian
top Paradox Salt
Leadville
top Precambrian
barrier fault
March 2019
N60°E
M < 1.5
M 1.5 - M 2.5
M >= 2.5
main shock
Projection Perpendicular to West Fault Plane
Horizontal Distance (km)
0.0
0.5
1.0
Depth Below Wellhead (km)
3.50
3.75
4.00
4.25
4.50
4.75
5.00
S10°E

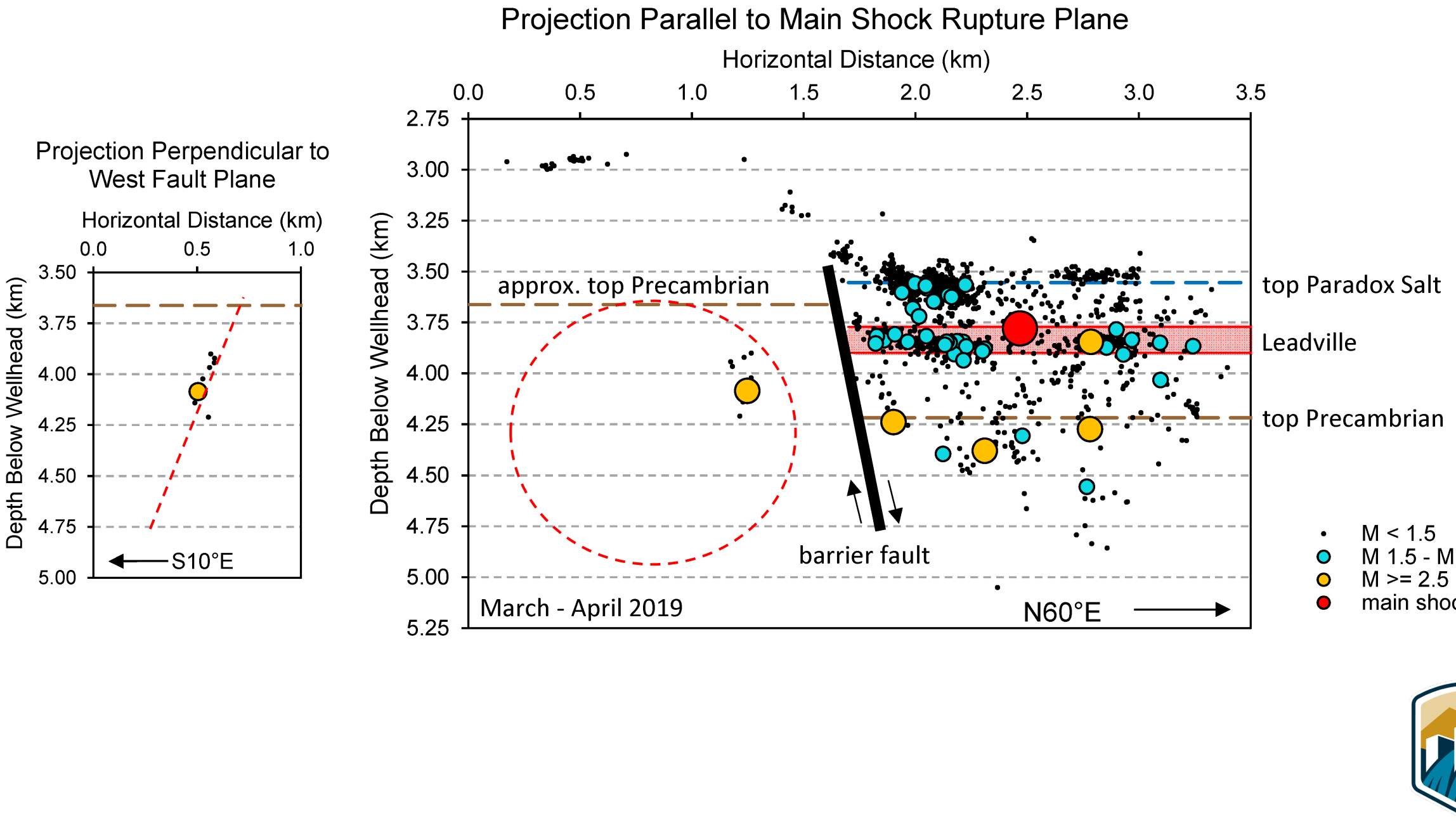
Projection Parallel to Main Shock Rupture Plane
Horizontal Distance (km)
0.0
0.5
1.0
1.5
2.0
2.5
3.0
3.5
Depth Below Wellhead (km)
2.75
3.00
3.25
3.50
3.75
4.00
4.25
4.50
4.75
5.00
5.25
approx. top Precambrian
top Paradox Salt
Leadville
top Precambrian
barrier fault
March - April 2019
N60°E
M < 1.5
M 1.5 - M 2.5
M >= 2.5
main shock
Projection Perpendicular to West Fault Plane
Horizontal Distance (km)
0.0
0.5
1.0
Depth Below Wellhead (km)
3.50
3.75
4.00
4.25
4.50
4.75
5.00
S10°E

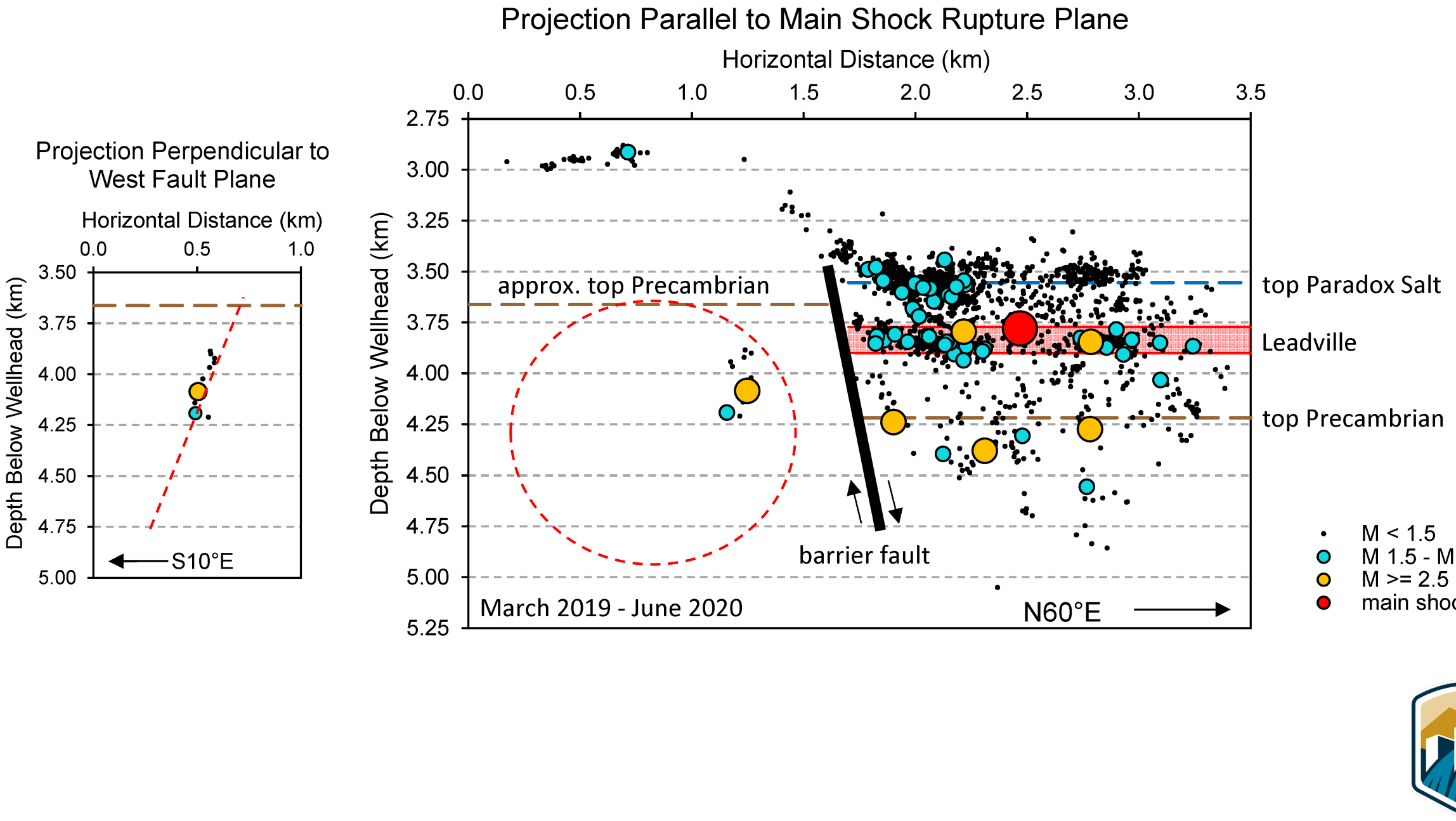
Projection Parallel to Main Shock Rupture Plane
Horizontal Distance (km)
0.0
0.5
1.0
1.5
2.0
2.5
3.0
3.5
Depth Below Wellhead (km)
2.75
3.00
3.25
3.50
3.75
4.00
4.25
4.50
4.75
5.00
5.25
approx. top Precambrian
top Paradox Salt
Leadville
top Precambrian
barrier fault
March 2019 - June 2020
N60°E
M < 1.5
M 1.5 - M 2.5
M >= 2.5
main shock
Projection Perpendicular to West Fault Plane
Horizontal Distance (km)
0.0
0.5
1.0
Depth Below Wellhead (km)
3.50
3.75
4.00
4.25
4.50
4.75
5.00
S10°E

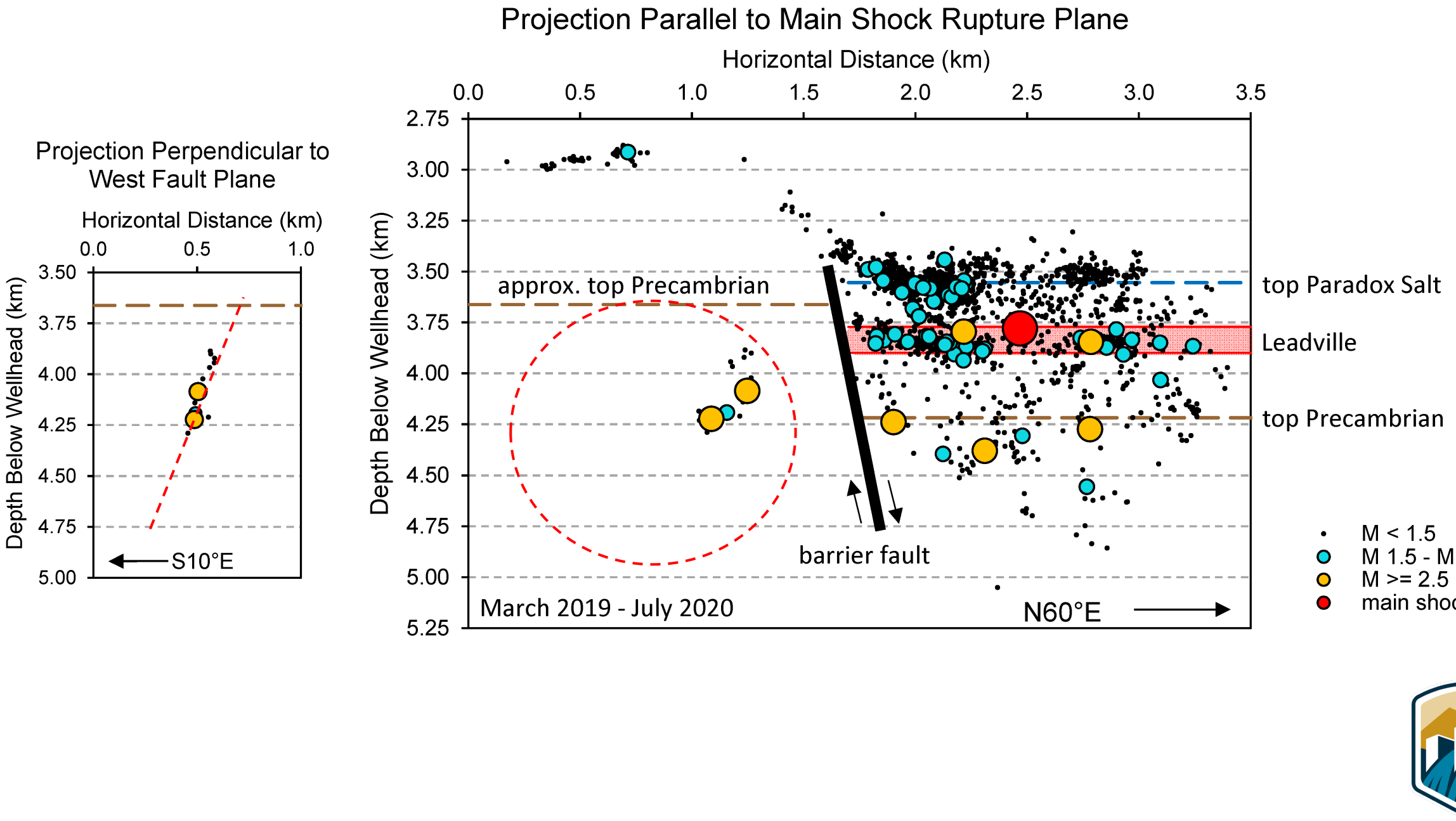
Projection Parallel to Main Shock Rupture Plane
Horizontal Distance (km)
0.0
0.5
1.0
1.5
2.0
2.5
3.0
3.5
Depth Below Wellhead (km)
2.75
3.00
3.25
3.50
3.75
4.00
4.25
4.50
4.75
5.00
5.25
approx. top Precambrian
top Paradox Salt
Leadville
top Precambrian
barrier fault
March 2019 - July 2020
N60°E
M < 1.5
M 1.5 - M 2.5
M >= 2.5
main shock
Projection Perpendicular to West Fault Plane
Horizontal Distance (km)
0.0
0.5
1.0
Depth Below Wellhead (km)
3.50
3.75
4.00
4.25
4.50
4.75
5.00
S10°E

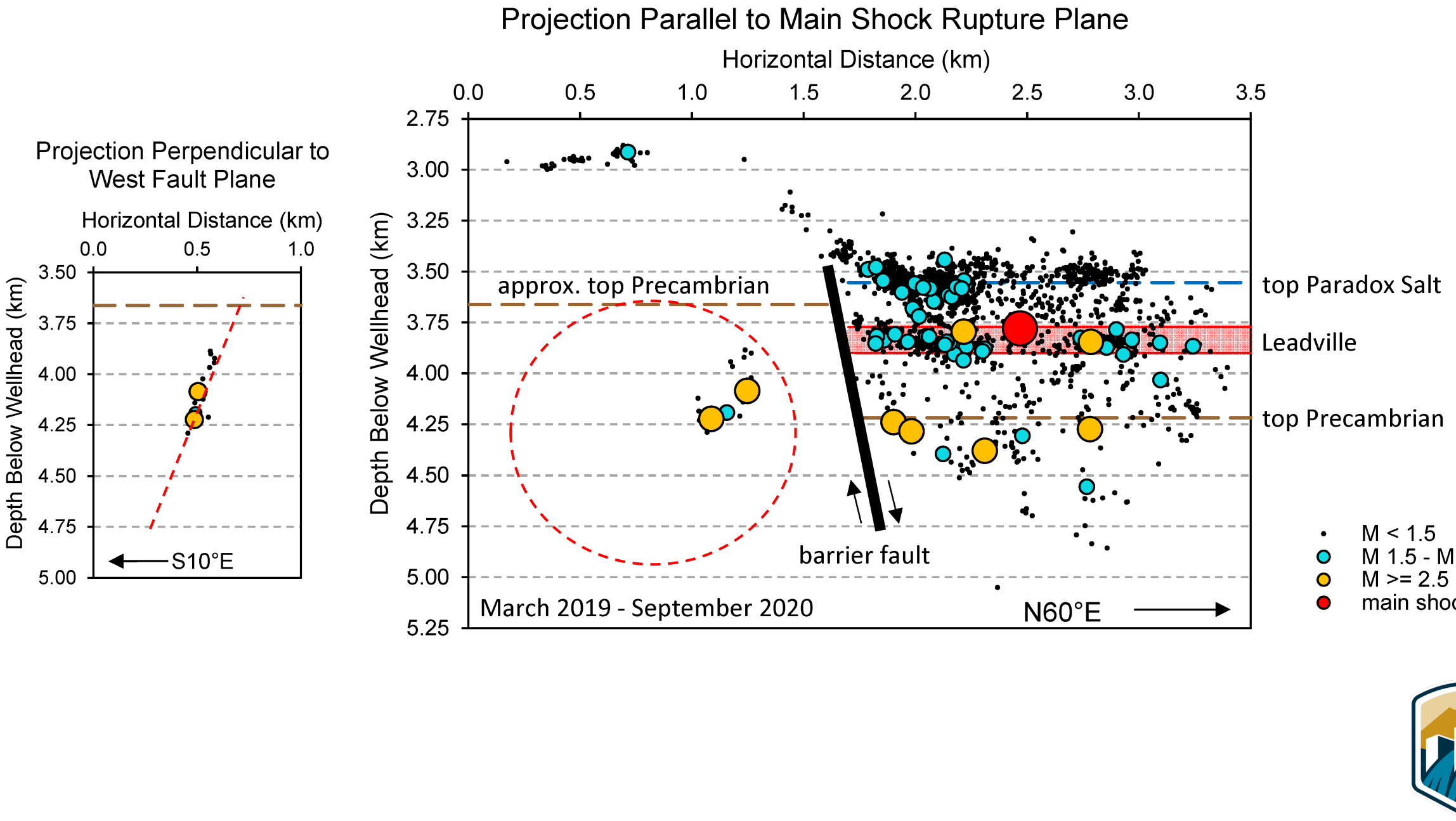
Projection Parallel to Main Shock Rupture Plane
Horizontal Distance (km)
0.0
0.5
1.0
1.5
2.0
2.5
3.0
3.5
Depth Below Wellhead (km)
2.75
3.00
3.25
3.50
3.75
4.00
4.25
4.50
4.75
5.00
5.25
approx. top Precambrian
top Paradox Salt
Leadville
top Precambrian
barrier fault
March 2019 - September 2020
N60°E
M < 1.5
M 1.5 - M 2.5
M >= 2.5
main shock
Projection Perpendicular to West Fault Plane
Horizontal Distance (km)
0.0
0.5
1.0
Depth Below Wellhead (km)
3.50
3.75
4.00
4.25
4.50
4.75
5.00
S10°E

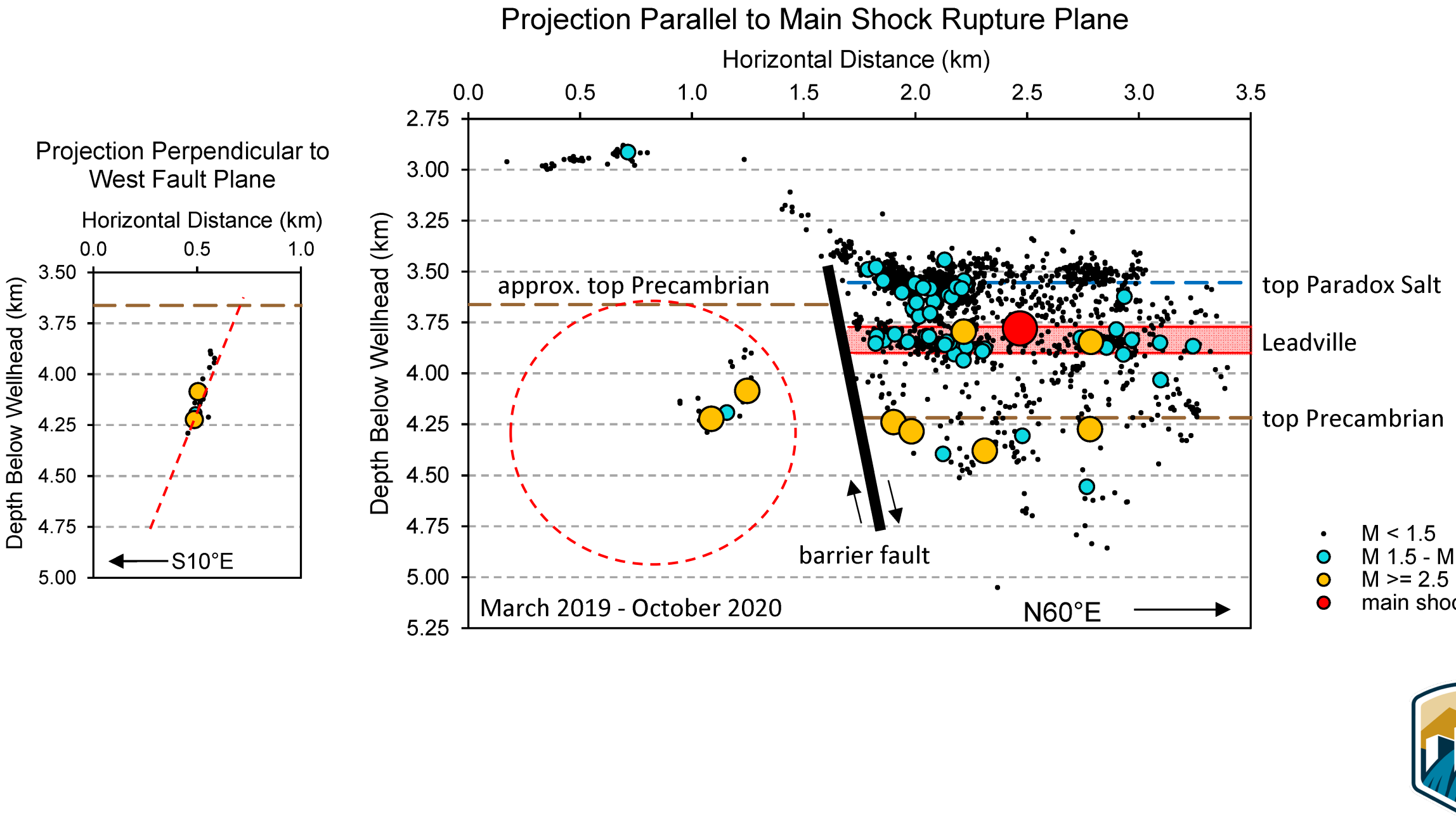
Projection Parallel to Main Shock Rupture Plane
Horizontal Distance (km)
0.0
0.5
1.0
1.5
2.0
2.5
3.0
3.5
Depth Below Wellhead (km)
2.75
3.00
3.25
3.50
3.75
4.00
4.25
4.50
4.75
5.00
5.25
approx. top Precambrian
top Paradox Salt
Leadville
top Precambrian
barrier fault
March 2019 - October 2020
N60°E
M < 1.5
M 1.5 - M 2.5
M >= 2.5
main shock
Projection Perpendicular to West Fault Plane
Horizontal Distance (km)
0.0
0.5
1.0
Depth Below Wellhead (km)
3.50
3.75
4.00
4.25
4.50
4.75
5.00
S10°E

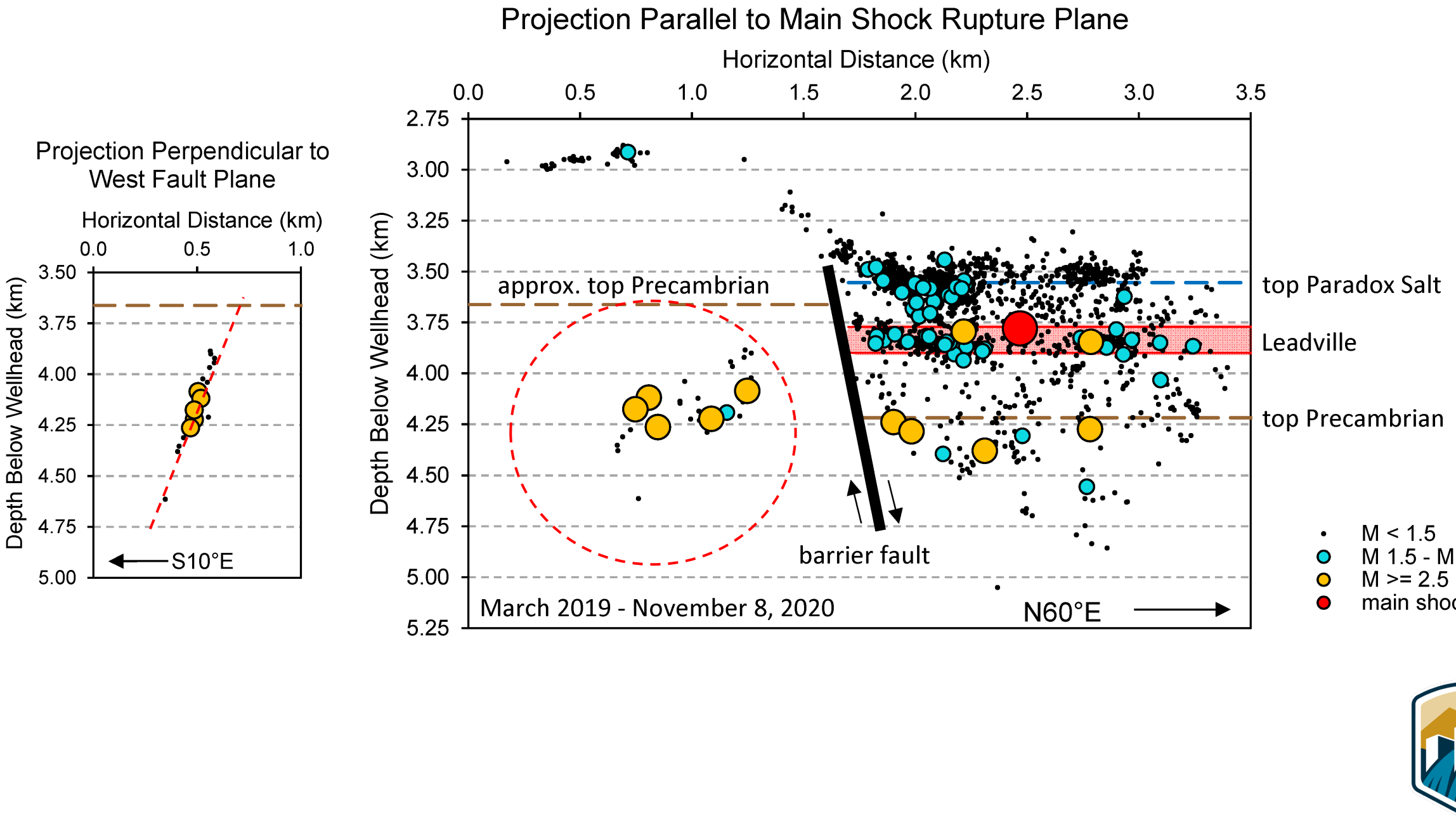
Projection Parallel to Main Shock Rupture Plane
Horizontal Distance (km)
0.0
0.5
1.0
1.5
2.0
2.5
3.0
3.5
Depth Below Wellhead (km)
2.75
3.00
3.25
3.50
3.75
4.00
4.25
4.50
4.75
5.00
5.25
approx. top Precambrian
top Paradox Salt
Leadville
top Precambrian
barrier fault
March 2019 - November 8, 2020
N60°E
M < 1.5
M 1.5 - M 2.5
M >= 2.5
main shock
Projection Perpendicular to West Fault Plane
Horizontal Distance (km)
0.0
0.5
1.0
Depth Below Wellhead (km)
3.50
3.75
4.00
4.25
4.50
4.75
5.00
S10°E

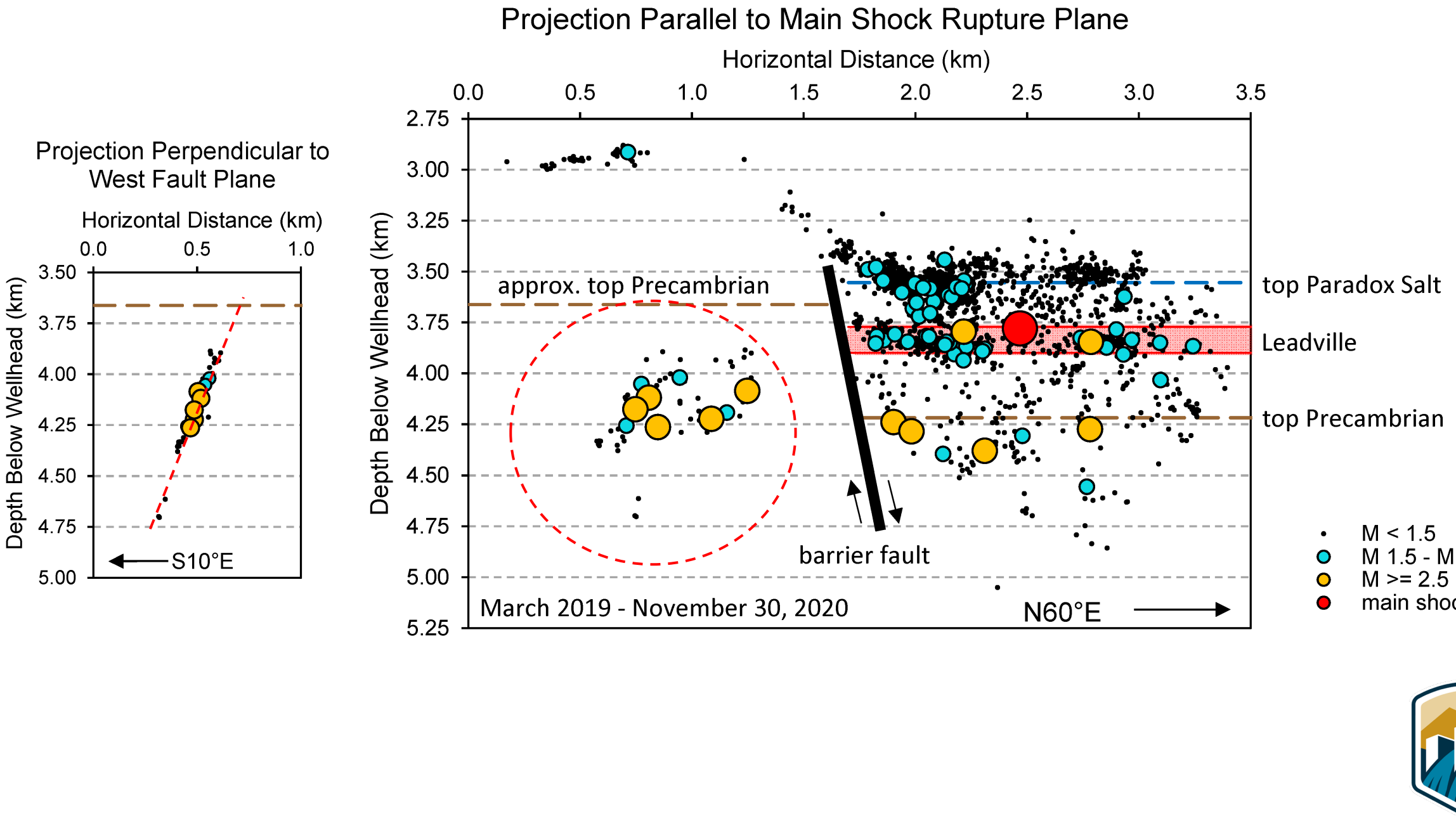
Projection Parallel to Main Shock Rupture Plane
Horizontal Distance (km)
0.0
0.5
1.0
1.5
2.0
2.5
3.0
3.5
Depth Below Wellhead (km)
2.75
3.00
3.25
3.50
3.75
4.00
4.25
4.50
4.75
5.00
5.25
approx. top Precambrian
top Paradox Salt
Leadville
top Precambrian
barrier fault
March 2019 - November 30, 2020
N60°E
M < 1.5
M 1.5 - M 2.5
M >= 2.5
main shock
Projection Perpendicular to West Fault Plane
Horizontal Distance (km)
0.0
0.5
1.0
Depth Below Wellhead (km)
3.50
3.75
4.00
4.25
4.50
4.75
5.00
S10°E

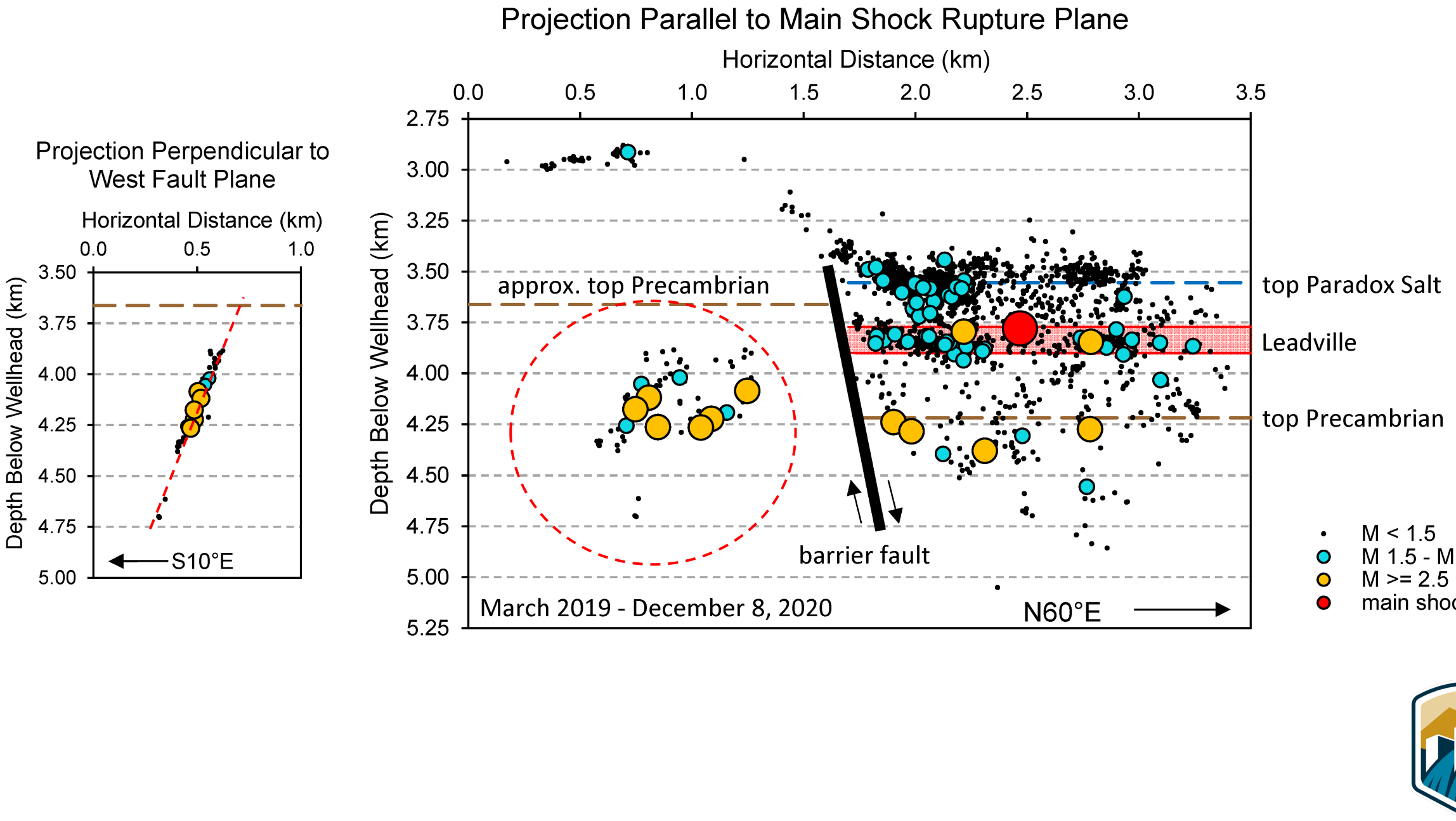
Projection Parallel to Main Shock Rupture Plane
Horizontal Distance (km)
0.0
0.5
1.0
1.5
2.0
2.5
3.0
3.5
Depth Below Wellhead (km)
2.75
3.00
3.25
3.50
3.75
4.00
4.25
4.50
4.75
5.00
5.25
approx. top Precambrian
top Paradox Salt
Leadville
top Precambrian
barrier fault
March 2019 - December 8, 2020
N60°E
M < 1.5
M 1.5 - M 2.5
M >= 2.5
main shock
Projection Perpendicular to West Fault Plane
Horizontal Distance (km)
0.0
0.5
1.0
Depth Below Wellhead (km)
3.50
3.75
4.00
4.25
4.50
4.75
5.00
S10°E

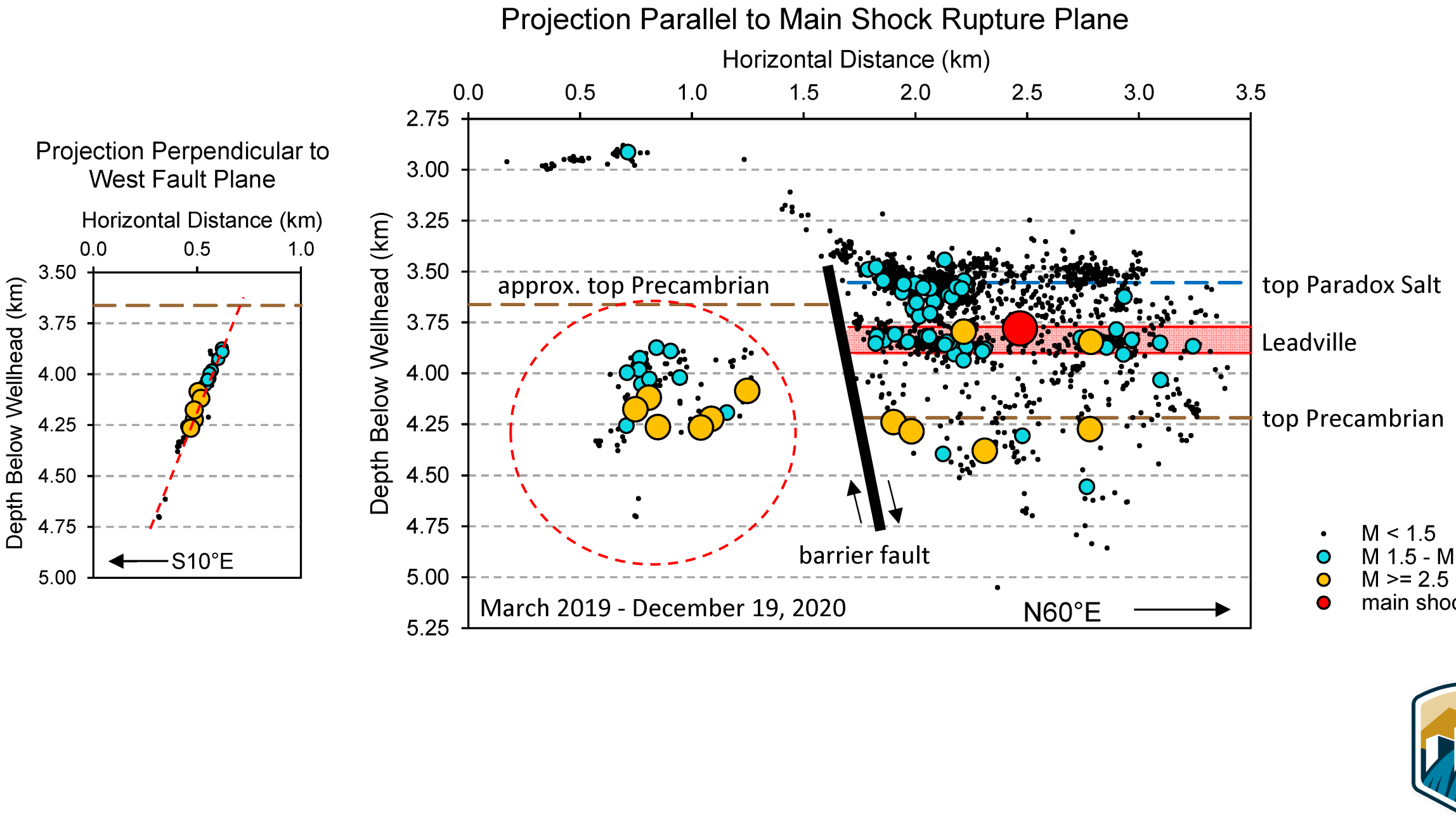
Projection Parallel to Main Shock Rupture Plane
Horizontal Distance (km)
0.0
0.5
1.0
1.5
2.0
2.5
3.0
3.5
Depth Below Wellhead (km)
2.75
3.00
3.25
3.50
3.75
4.00
4.25
4.50
4.75
5.00
5.25
approx. top Precambrian
top Paradox Salt
Leadville
top Precambrian
barrier fault
March 2019 - December 19, 2020
N60°E
M < 1.5
M 1.5 - M 2.5
M >= 2.5
main shock
Projection Perpendicular to West Fault Plane
Horizontal Distance (km)
0.0
0.5
1.0
Depth Below Wellhead (km)
3.50
3.75
4.00
4.25
4.50
4.75
5.00
S10°E

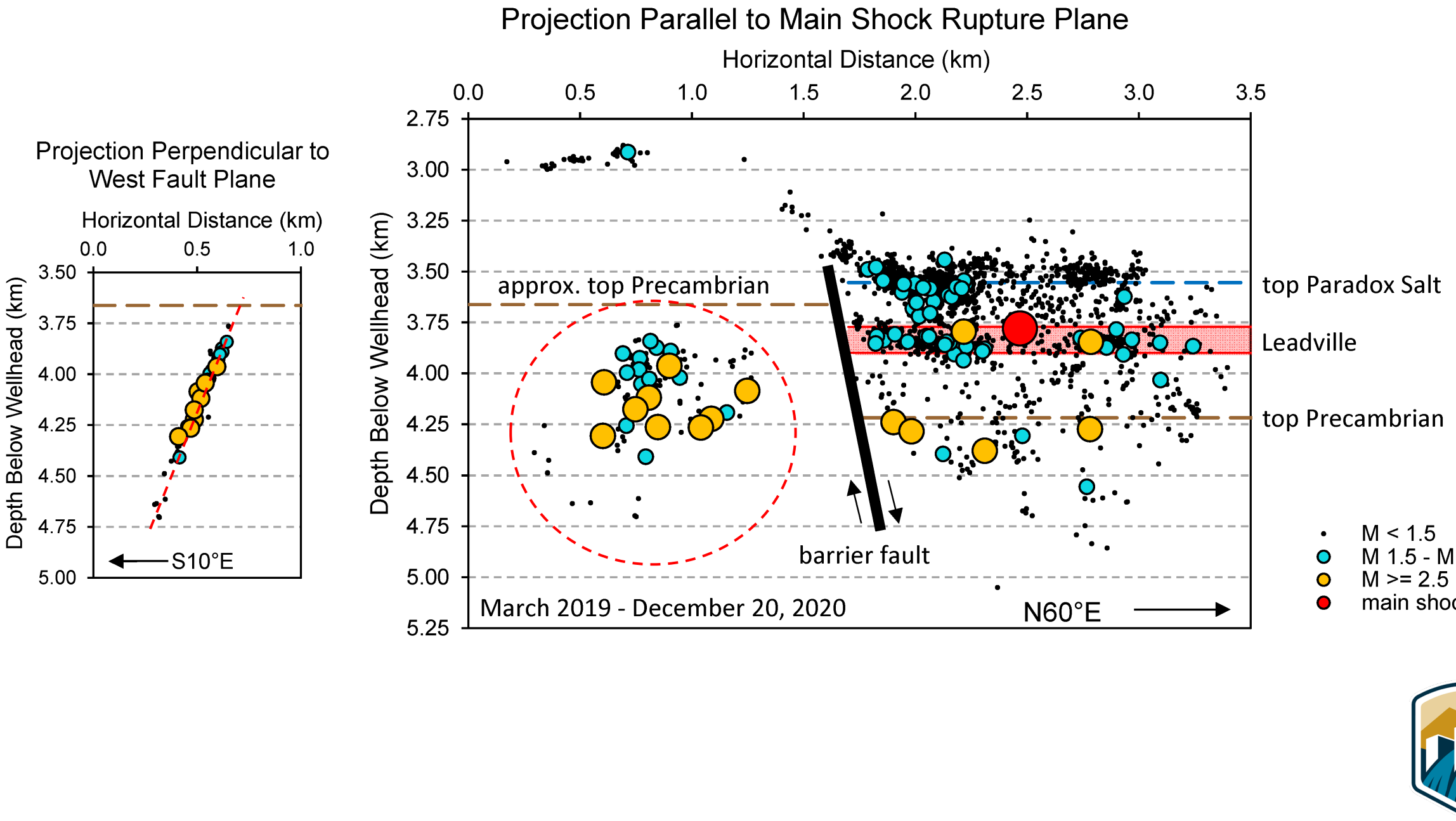
Projection Parallel to Main Shock Rupture Plane
Horizontal Distance (km)
0.0
0.5
1.0
1.5
2.0
2.5
3.0
3.5
Depth Below Wellhead (km)
2.75
3.00
3.25
3.50
3.75
4.00
4.25
4.50
4.75
5.00
5.25
approx. top Precambrian
top Paradox Salt
Leadville
top Precambrian
barrier fault
March 2019 - December 20, 2020
N60°E
M < 1.5
M 1.5 - M 2.5
M >= 2.5
main shock
Projection Perpendicular to West Fault Plane
Horizontal Distance (km)
0.0
0.5
1.0
Depth Below Wellhead (km)
3.50
3.75
4.00
4.25
4.50
4.75
5.00
S10°E

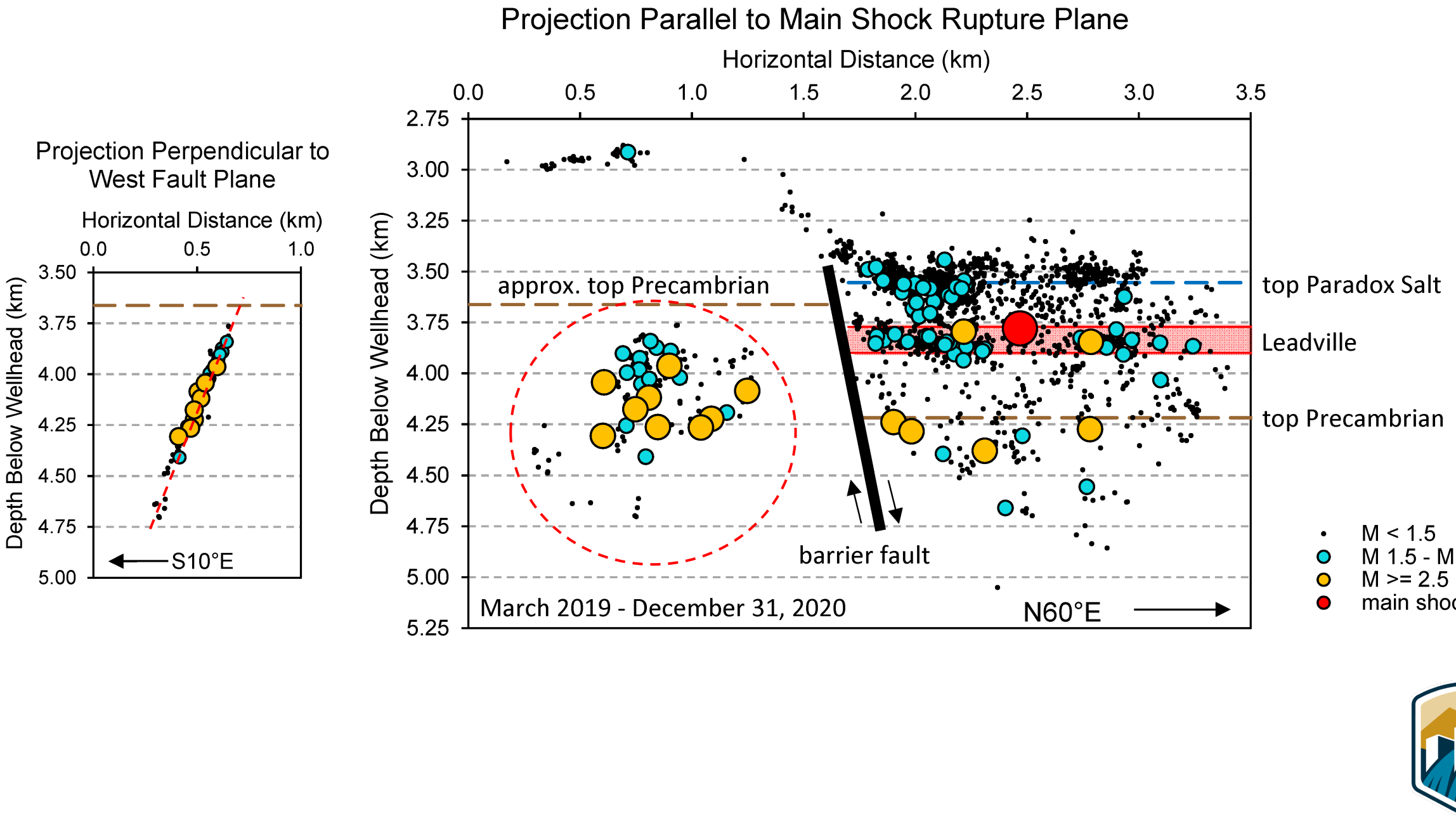
Projection Parallel to Main Shock Rupture Plane
Horizontal Distance (km)
0.0
0.5
1.0
1.5
2.0
2.5
3.0
3.5
Depth Below Wellhead (km)
2.75
3.00
3.25
3.50
3.75
4.00
4.25
4.50
4.75
5.00
5.25
approx. top Precambrian
top Paradox Salt
Leadville
top Precambrian
barrier fault
March 2019 - December 31, 2020
N60°E
M < 1.5
M 1.5 - M 2.5
M >= 2.5
main shock
Projection Perpendicular to West Fault Plane
Horizontal Distance (km)
0.0
0.5
1.0
Depth Below Wellhead (km)
3.50
3.75
4.00
4.25
4.50
4.75
5.00
S10°E

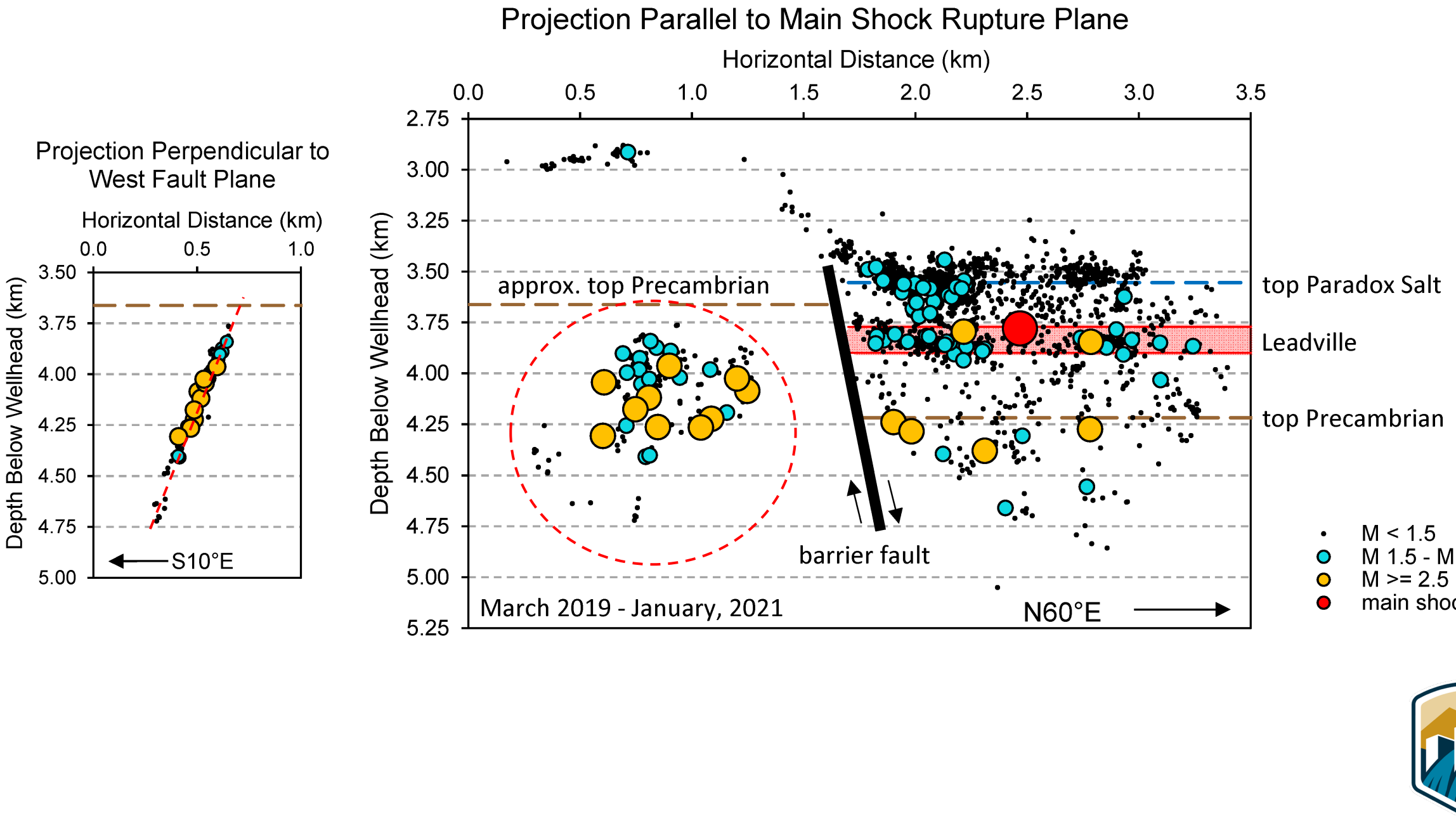
Projection Parallel to Main Shock Rupture Plane
Horizontal Distance (km)
0.0
0.5
1.0
1.5
2.0
2.5
3.0
3.5
Depth Below Wellhead (km)
2.75
3.00
3.25
3.50
3.75
4.00
4.25
4.50
4.75
5.00
5.25
approx. top Precambrian
top Paradox Salt
Leadville
top Precambrian
barrier fault
March 2019 - January, 2021
N60°E
M < 1.5
M 1.5 - M 2.5
M >= 2.5
main shock
Projection Perpendicular to West Fault Plane
Horizontal Distance (km)
0.0
0.5
1.0
Depth Below Wellhead (km)
3.50
3.75
4.00
4.25
4.50
4.75
5.00
S10°E

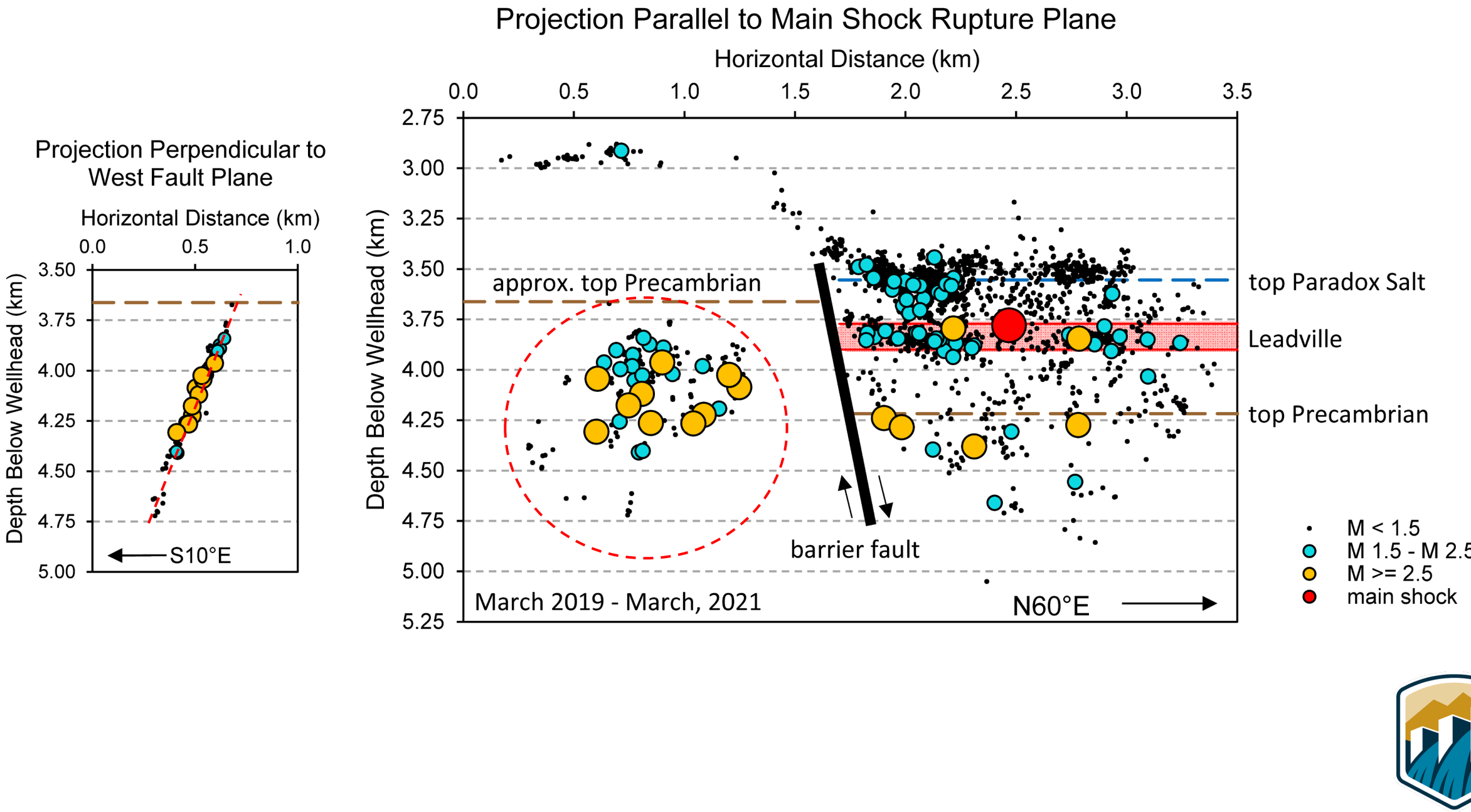
Projection Parallel to Main Shock Rupture Plane
Horizontal Distance (km)
0.0
0.5
1.0
1.5
2.0
2.5
3.0
3.5
Depth Below Wellhead (km)
2.75
3.00
3.25
3.50
3.75
4.00
4.25
4.50
4.75
5.00
5.25
approx. top Precambrian
top Paradox Salt
Leadville
top Precambrian
barrier fault
March 2019 - March, 2021
N60°E
M < 1.5
M 1.5 - M 2.5
M >= 2.5
main shock
Projection Perpendicular to West Fault Plane
Horizontal Distance (km)
0.0
0.5
1.0
Depth Below Wellhead (km)
3.50
3.75
4.00
4.25
4.50
4.75
5.00
S10°E

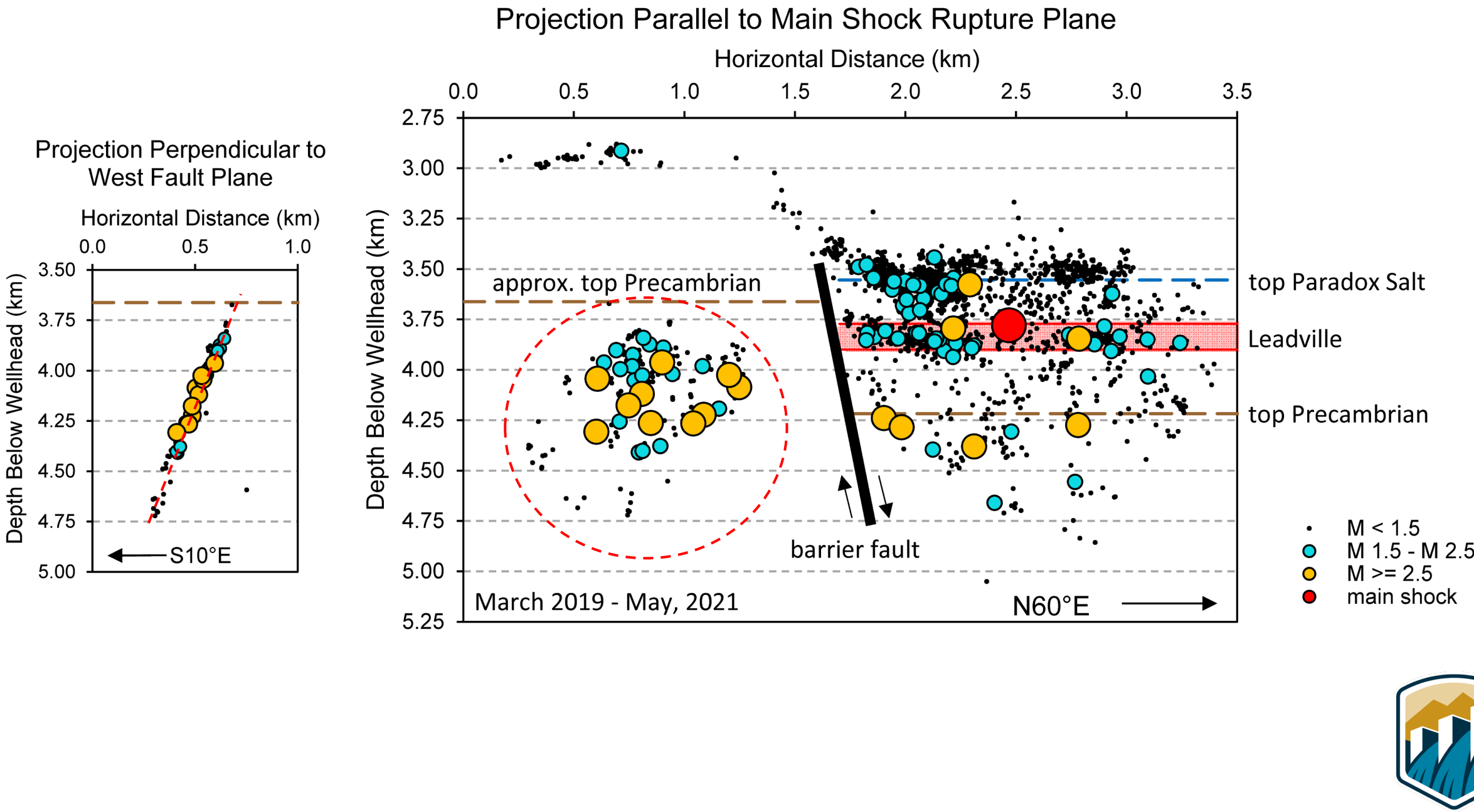
Projection Parallel to Main Shock Rupture Plane
Horizontal Distance (km)
0.0
0.5
1.0
1.5
2.0
2.5
3.0
3.5
Depth Below Wellhead (km)
2.75
3.00
3.25
3.50
3.75
4.00
4.25
4.50
4.75
5.00
5.25
approx. top Precambrian
top Paradox Salt
Leadville
top Precambrian
barrier fault
March 2019 - May, 2021
N60°E
M < 1.5
M 1.5 - M 2.5
M >= 2.5
main shock
Projection Perpendicular to West Fault Plane
Horizontal Distance (km)
0.0
0.5
1.0
Depth Below Wellhead (km)
3.50
3.75
4.00
4.25
4.50
4.75
5.00
S10°E

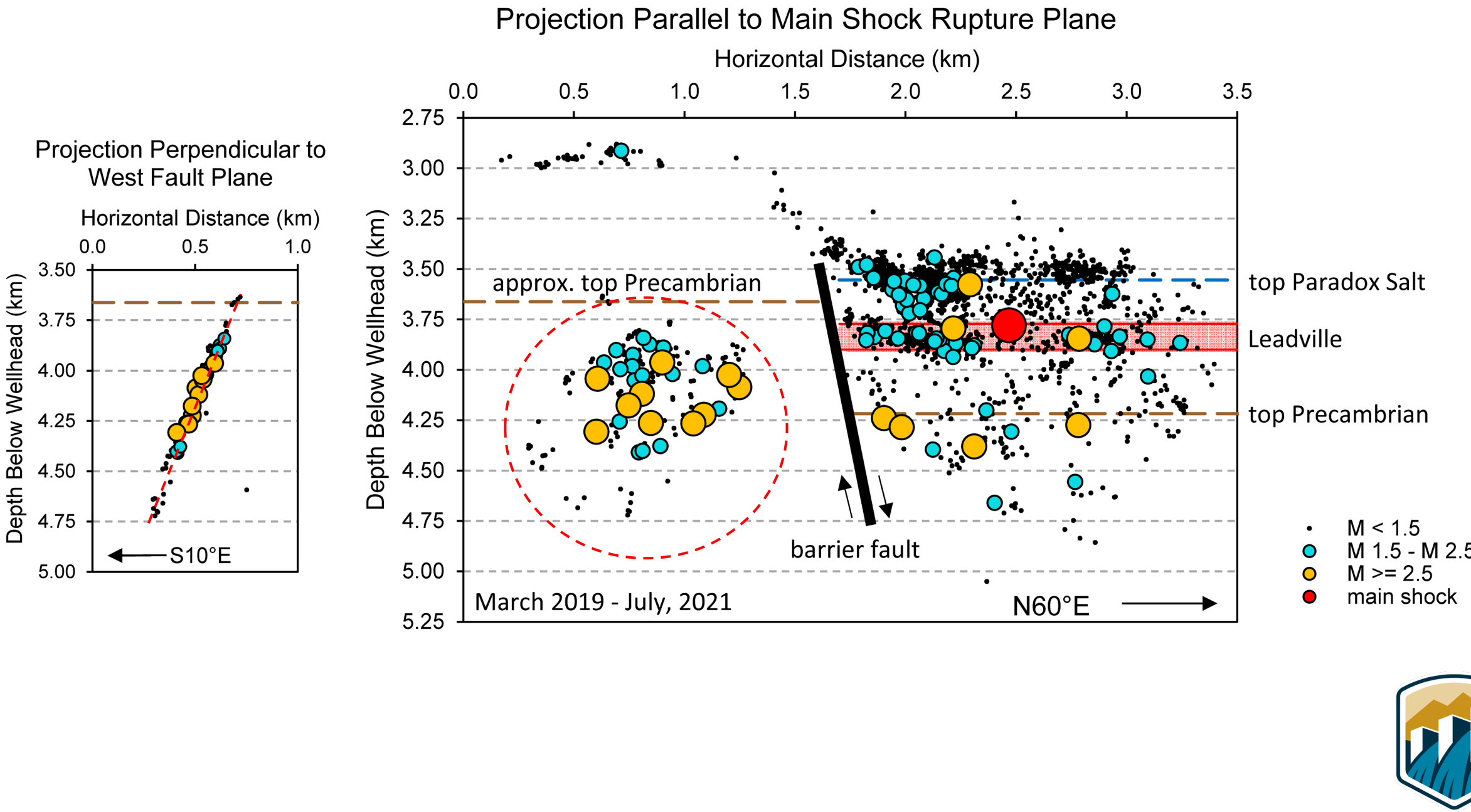
Projection Parallel to Main Shock Rupture Plane
Horizontal Distance (km)
0.0
0.5
1.0
1.5
2.0
2.5
3.0
3.5
Depth Below Wellhead (km)
2.75
3.00
3.25
3.50
3.75
4.00
4.25
4.50
4.75
5.00
5.25
approx. top Precambrian
top Paradox Salt
Leadville
top Precambrian
barrier fault
March 2019 - July, 2021
N60°E
M < 1.5
M 1.5 - M 2.5
M >= 2.5
main shock
Projection Perpendicular to West Fault Plane
Horizontal Distance (km)
0.0
0.5
1.0
Depth Below Wellhead (km)
3.50
3.75
4.00
4.25
4.50
4.75
5.00
S10°E

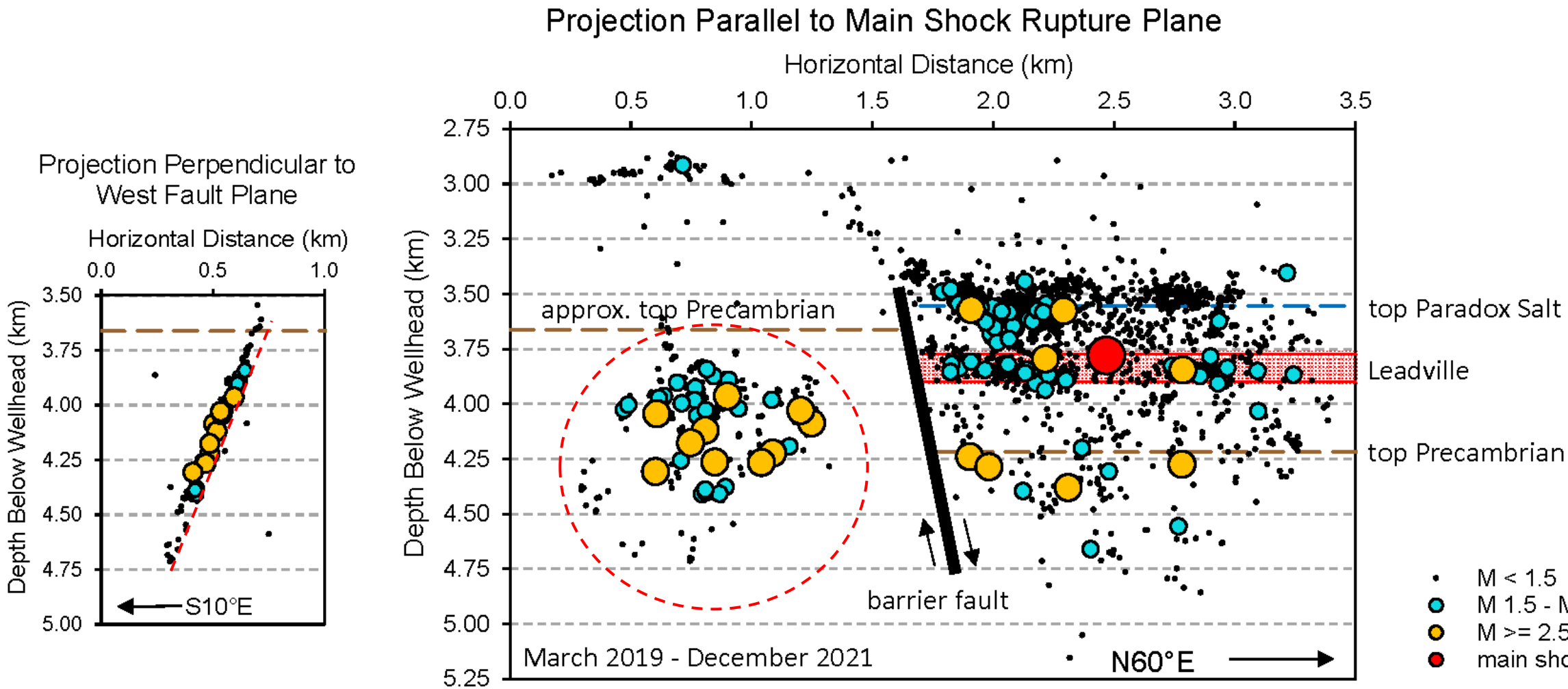
Projection Parallel to Main Shock Rupture Plane
Horizontal Distance (km)
0.0
0.5
1.0
1.5
2.0
2.5
3.0
3.5
Depth Below Wellhead (km)
2.75
3.00
3.25
3.50
3.75
4.00
4.25
4.50
4.75
5.00
5.25
approx. top Precambrian
top Paradox Salt
Leadville
top Precambrian
barrier fault
March 2019 - December 2021
N60°E
M < 1.5
M 1.5 - M 2.5
M >= 2.5
main shock
Projection Perpendicular to
West Fault Plane
Horizontal Distance (km)
0.0
0.5
1.0
Depth Below Wellhead (km)
3.50
3.75
4.00
4.25
4.50
4.75
5.00
S10°E

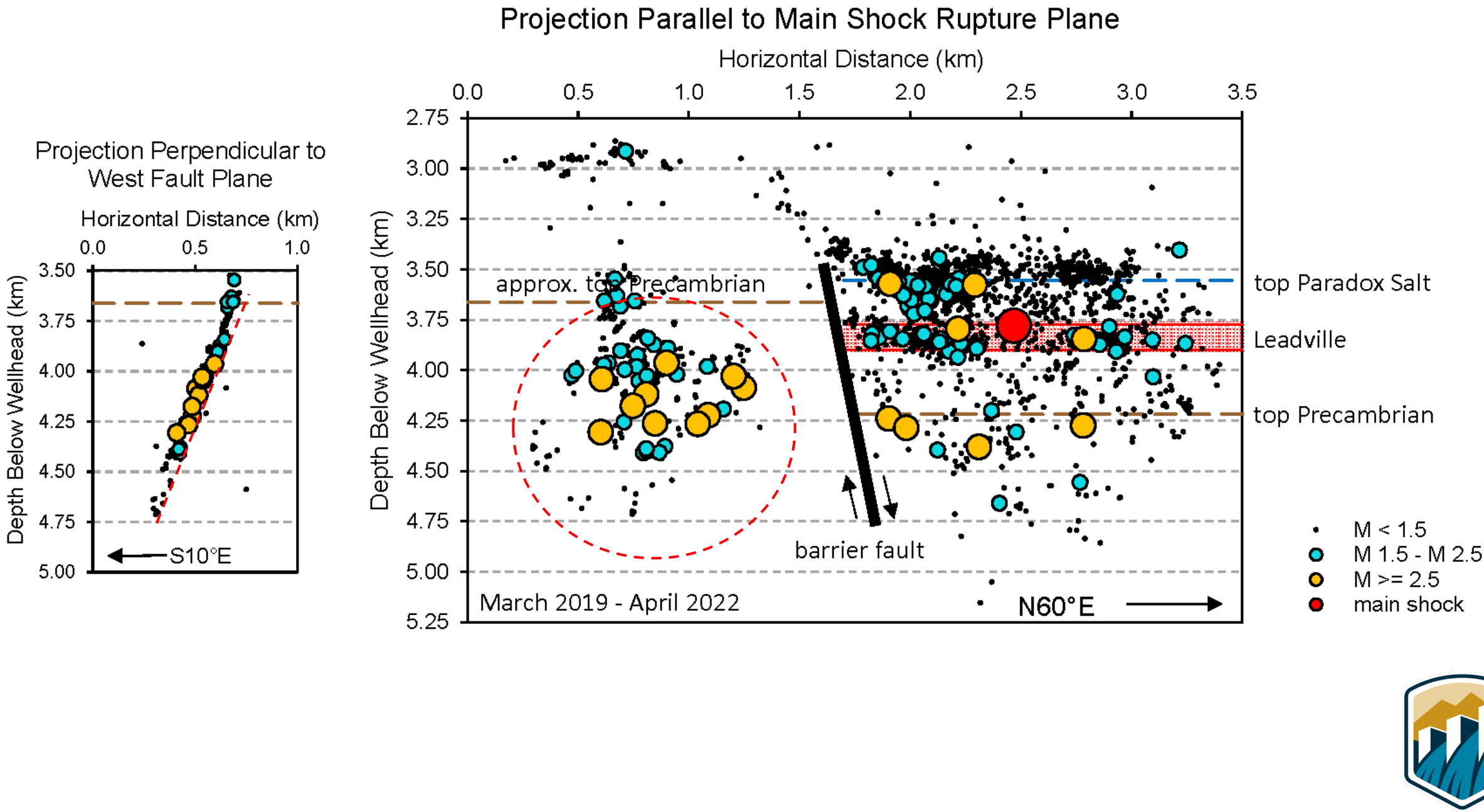
Projection Parallel to Main Shock Rupture Plane
Horizontal Distance (km)
0.0
0.5
1.0
1.5
2.0
2.5
3.0
3.5
Depth Below Wellhead (km)
2.75
3.00
3.25
3.50
3.75
4.00
4.25
4.50
4.75
5.00
5.25
approx. top Precambrian
top Paradox Salt
Leadville
top Precambrian
barrier fault
March 2019 - April 2022
N60°E
M < 1.5
M 1.5 - M 2.5
M >= 2.5
main shock
Projection Perpendicular to
West Fault Plane
Horizontal Distance (km)
0.0
0.5
1.0
Depth Below Wellhead (km)
3.50
3.75
4.00
4.25
4.50
4.75
5.00
S10°E

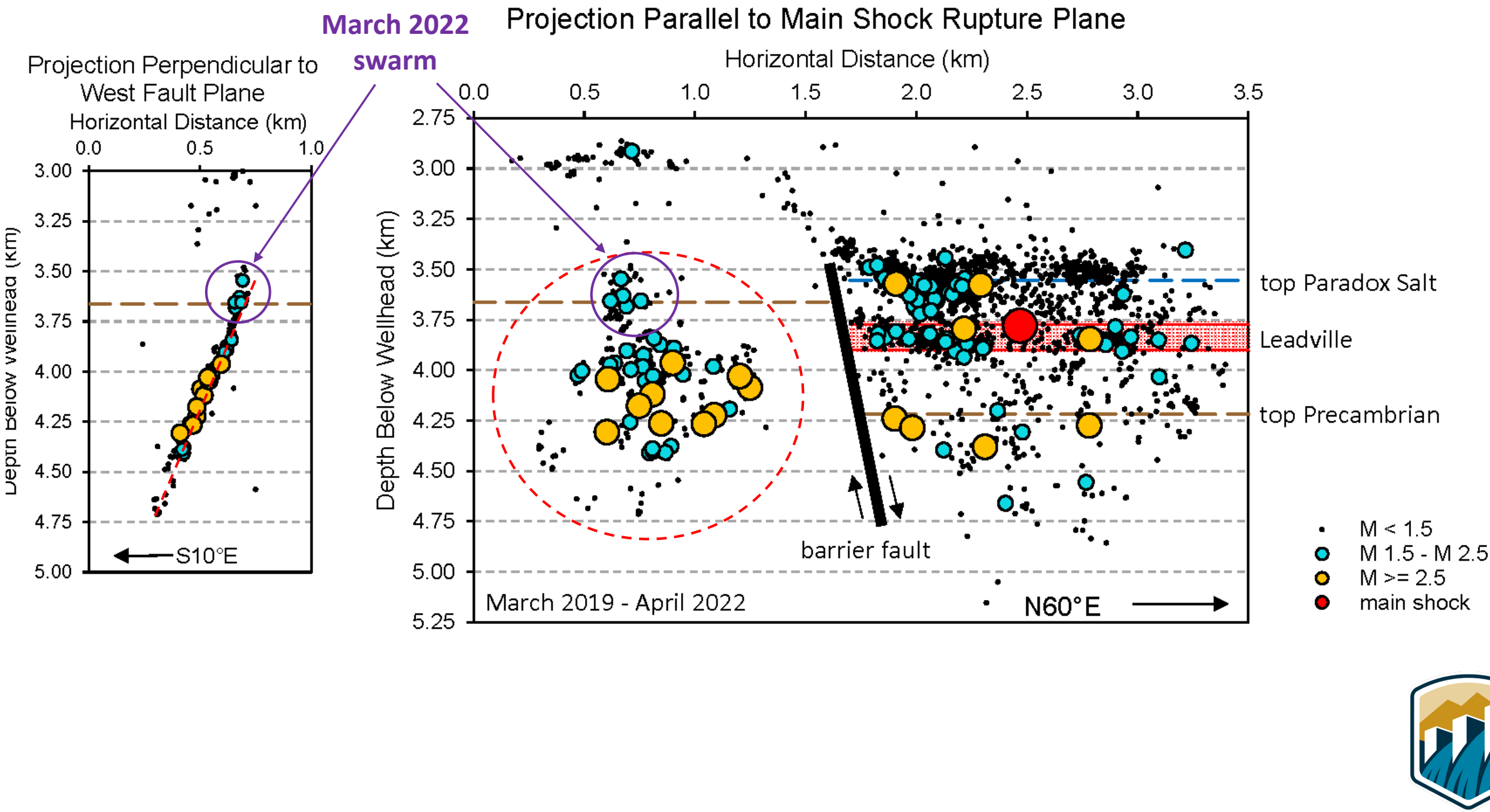
March 2022
swarm
Projection Parallel to Main Shock Rupture Plane
Horizontal Distance (km)
0.0
0.5
1.0
1.5
2.0
2.5
3.0
3.5
Depth Below Wellhead (km)
2.75
3.00
3.25
3.50
3.75
4.00
4.25
4.50
4.75
5.00
5.25
top Paradox Salt
Leadville
top Precambrian
barrier fault
March 2019 - April 2022
N60°E
M < 1.5
M 1.5 - M 2.5
M >= 2.5
main shock
Projection Perpendicular to
West Fault Plane
Horizontal Distance (km)
0.0
0.5
1.0
3.00
3.25
3.50
3.75
4.00
4.25
4.50
4.75
5.00
S10°E

Appendix B

Electronic Attachments

Earthquake Catalog

The catalog of earthquakes in the SW cluster used for the analyses presented in this report are provided as an electronic attachment (file "TM 86-68330-2024-8 SWcluster catalog.csv"). These earthquake hypocenters were computed using a local three-dimensional velocity model that was developed in 2011. Since the analyses presented in this report were completed, a new velocity model has been developed for the Paradox Valley area (Block, 2024a). Absolute and relative hypocenters were subsequently re-computed for the full PVSN earthquake catalog using the updated velocity model. This more complete, updated earthquake catalog is available as an electronic attachment to Block (2024b).

The attached catalog contains one hypocenter for each earthquake. Relative (a-quality) hypocenters are provided for the earthquakes that tie into the relation location inversions. For the earthquakes that do not tie into the relative location inversions, the absolute (b-quality) hypocenters are provided. In the attached catalog, 261 hypocenters (~98% of the events) have a-quality hypocenters, and the remaining 6 earthquakes have b-quality hypocenters.

The earthquake catalog file contains the following columns:

Event_ID: Identification number of event

Year: Earthquake origin time year
Month: Earthquake origin time month
Day: Earthquake origin time day
Hour: Earthquake origin time hour
Minute: Earthquake origin time minute
Second: Earthquake origin time second

Latitude_(deg): Hypocenter latitude in decimal degrees North.
Longitude_(deg): Hypocenter longitude in decimal degrees; negative values are West
Elevation_(m): Hypocenter elevation in meters with respect to mean sea level

Md: Duration Magnitude; the duration magnitudes saturate above approximately Md 3.0.
Mw: Moment Magnitude; computed using only PVSN data.

Quality: Indicates whether the hypocenter was computed with a relative location method (quality = 'a') or an absolute location method (quality='b').

RMS_residual_(s): Root-mean-square (rms) time residual in seconds. For b-quality events, this is the rms of the absolute time residuals. For a-quality events, this is the rms of the time difference residuals.
Nabstimes: Number of arrival times used to compute the absolute location of b-quality events. (Zero for a-quality events.)
Neventpairs: Number of event pairs providing time differences for the relative location of a-quality events. (Zero for b-quality events.)

Ntimediffs: Number of time differences used to compute the relative location of a-quality events. (Zero for b-quality events.)
Nstations: Number of stations providing data for the hypocenter calculations, either in terms of absolute arrival times (for b-quality events) or time differences (for a-quality events).
Maxgap_(deg): Maximum azimuthal gap in ray coverage to the nearest integer degree. For the event relative location (a-quality events), this considers data for all event pairs.
Min_dist/depth: Horizontal distance to the closest seismic station providing data for the hypocenter calculation divided by the hypocenter depth.

PVU Injection Data

Daily average pressure and flow rate data are provided in the attached file "TM 86-68330-2024-8 PVU injection data.csv". These data encompass the period from July 10, 1991 (just before the beginning of the first injection test) through December 2023. The data recorded during the injection test period from 1991 to 1995 have several gaps extending up to several months. There are periods when the injection rates and pressures appear to be inconsistent with one another, for example increasing pressures during periods of zero flow rate. We have not attempted to correct these errors.

The data completeness is significantly better during the period of continuous injection, which began in 1996. However, there was a gap in the pressure data from June 6, 2001 to June 18, 2001, which was filled in using interpolation. Additionally, the pressures from June 19 to June 22, 2001 were inconsistent with the shape of the fall-off curves from other cycles. It seems likely that these values are in error, and they were replaced with interpolated values.

The pressures in the attached file are recorded surface pressures. Downhole pressures can be calculated using the density of the borehole fluid, which varies over time as shown in Table B-1.

Table B-1: Composition and corresponding density of borehole fluid

Start Date	End Date	Composition of Borehole Fluid	Density (g/cm^3)
7/11/1991	8/14/1991	100% fresh water	1.00
8/15/1991	11/4/1991	1/3 brine : 2/3 fresh water	1.06
11/5/1991	11/16/1992	2/3 brine : 1/3 fresh water	1.11
11/17/1992	6/5/1993	100% brine	1.17
6/6/1993	10/2/1993	100% fresh water	1.00
10/3/1993	1/6/2002	70% brine : 30% fresh water	1.12
1/7/2002	present	100% brine	1.17